Yasmin Carina Bürkl, BSc

Substitution of Zirconium in Lead-Lanthanum-Zirconate-Titanate by isovalent Hafnium

Masterarbeit

Zur Erlangung des akademischen Grades

Diplom-Ingenieurin

Masterstudium Technische Chemie

eingereicht an der

Technische Universität Graz

Betreuer

Ao. Univ.-Prof. dipl.-Ing. Dr. techn. Klaus Reichmann

Institut für Chemische Technologien von Materialien

Graz, November 2014

EIDESSTATTLICHE ERKLÄRUNG

AFFIDAVIT

Ich erkläre an Eides statt, dass ich die vorliegende Arbeit selbstständig verfasst, andere als die angegebenen Quellen/Hilfsmittel nicht benutzt, und die den benutzten Quellen wörtlich und inhaltlich entnommenen Stellen als solche kenntlich gemacht habe. Das in TUGRAZonline hochgeladene Textdokument ist mit der vorliegenden Masterarbeit identisch.

I declare that I have authored this thesis independently, that I have not used other than the declared sources/resources, and that I have explicitly indicated all material which has been quoted either literally or by content from the sources used. The text document uploaded to TUGRAZonline is identical to the present master's thesis.

Datum / Date	Unterschrift / Signature

Acknowledgement

I want to thank Prof. Klaus Reichmann for allowing me to work on this interesting topic and for supporting me during my master thesis. I also want to thank Theresa Kainz for always having an open ear and the help she provided.

Additionally I want to acknowledge Christian Doppler Research Association and EPCOS OHG (TDK-EPC) for funding the project, Prof. Franz Mautner for the XRD measurements,SanjaSimic from FELMI-ZFE for the SEM measurements and Albering Christina.

Furthermore I want to thank my family for the encouragement and kind words given to me over the years and especially my parents, Helmut and Claudia, for not only enabling me to pursue my studies, but also for always supporting and helping me. You always cheered me up and motivated me when others couldn't.

I also want to thank my friends here at Graz for the past five+ years of studying, celebrating and having fun together. Special thanks go out to my best friend Betti, who not only is for a big part responsible for the swift progress in my studies, but has also become an additional part of the family to me.

Abstract

In this thesis the influence of substituting zirconium by hafnium on the antiferroelectric material lead lanthanum zirconatetitanate (PLZT) is investigated, as well as the influence of the atomic mass of a dopant on the properties of a material. Two different series with varying zirconium/titanium ratio were prepared and doped with increasing concentrations of hafnium following the formula: $Pb_{0,91}La_{0,06}V_{Pb}^{II}{}_{0,03}(Hf_xZr_{1-x})_yTi_{1-y}$ (x:0 to 0,3; y: 0,9 or 0,85). The samples were prepared using mixed oxide method, calcinated at 850°C and sintered at 1250°C. The incorporation of hafnium into the material was controlled using X-ray powder diffraction and scanning electron microscopy.

The microstructure was investigated using secondary electron and back scattered electron microscopy. The images obtained were used to determine the average grain size and the occurrence of secondary phases.

The dielectric properties measured were thepermittivity and the loss factor.The permittivity versus temperature was measured to determine phase transition temperatures.Theantiferroelectric properties like saturation polarization and switching field were taken from polarization curves.

While the chosen temperatures and the sintering set-up for sample preparation worked well in terms of densification and sintering behavior, secondary phases remained in the material at hafnium concentrations above 10 mol%. The series were compared with each other and it was found that hafnium doping has only a small influence on the switching field and the grain size of PLZT. The variation of the zirconium/titanium ratio has a bigger influence on the performance of the material. The atomic mass of a dopant seems to have a smaller influence on the properties of a material compared with the ionic radius.

Kurzfassung

In dieser Arbeit wird der Einfluss der Substitution von Zirkonium durch Hafnium auf das antiferroeletrische Material Blei-Lanthan-Zirkon-Titanat untersucht. Auch der Einfluss der molekularen Masse eines Dotierstoffes auf ein Material wird untersucht. Es wurden zwei Serien mit unterschiedlichem Zirkon/Titan Verhältnis und variierendem Hafniumgehalt nach folgender Summenformel hergestellt: $_{,91}La_{0,06}V_{Pb}^{II}{}_{0,03}(Hf_xZr_{1-x})_yTi_{1-y}$ (x:0 bis 0,3; y: 0,9 oder 0,85). Zur Herstellung der Proben wurde das Mischoxidverfahren verwendet. Die Proben wurden bei 850°C kalziniert und bei 1250°C gesintert. Die Aufnahme des Hafniums in das Material wurde durch XRD Messungen und Rasterelektronenmikroskopie überprüft.

Die Mikrostruktur wurde mit Hilfe von Sekundärelektronen- und Rückstreuelektronenmikroskopie untersucht. Die erhaltenen Bilder wurden zur Bestimmung der Korngröße und dem Überprüfen auf Sekundärphasen herangezogen.

Die dielektrischen Eigenschaften Permitivität und Verlustfaktor wurden bestimmt. Die Permitivität über einen Temperaturbereich wurden gemessen um Phasenübergänge zu bestimmen. Die Polarisation über ein elektrisches Feld wurde gemessen um antiferroelektrische Eigenschaften wie Schaltfelder und Sättigungspolarisation zu erhalten.

Obwohl die gewählten Temperaturen und der Sinteraufbau für die Probenherstellung zu einer guten Verdichtung und Sinterverhalten führten, blieben bei höheren Hafniumkonzentrationen über 10 mol% Sekundärphasen im Material zurück. Die beiden Serien wurden mit einander verglichen und es wurde festgestellt, dass die Dotierung mit Hafnium nur einen geringen Einfluss auf das Schaltfeld hat. Die Variation des Zirkon/Titan Verhältnisses hatte einen weit größeren Einfluss auf die Leistung des Materials. Der Einfluss der Atommasse eines Dotierelements scheint weit geringer zu sein als der Einfluss des ionischen Radius auf ein Material.

Table ofcontent

1. Introduction

The objective of this thesis is to investigate the influence of substitution of zirconium by hafnium on the antiferroelectric material lead-lanthanum zirconatetitanate (PLZT). Recently antiferroelectrics have been used in multilayer ceramic devices for power conversion as dielectric(CeraLink by TDK-EPC, [1]). To increase the area of possible applications, doping of such dielectric materials is studied intensively. The main goal is to reduce the size and weight and to increase the performance.

By doping (substituting an ion in the lattice) tailoring the size and the properties of the material becomes possible. Dopants can influence a material through tree main factors: ionic radius, atomic mass and valency (electronical configuration). When tailoring the performance of a material this way, it is not possible to discern the exact influence of one of the parameters, as most dopants differ in at least two of the parameters mentioned above from the ion they are replacing. A better understanding of the separate influences of these parameters may lead to a better understanding of the doping process and an easier tailoring of materials.

The aim of this thesis is to investigate the substituting zirconium by hafnium in PLZT and to determine its influence on properties such as permittivity, loss factor, density, grain size, switching field and saturation polarization. The substitution of zirconium by hafnium is of special interest because the two ions differ only in their atomic mass. Therefore changes found in the material can be directly linked to the change in atomic mass. There is only one publication currently available that deals with this system [2] and it focuses on varying titanium concentration without changing the hafnium concentration.

2. Theoretical part

2.1. Electrical properties

2.1.1. Paraelectricity

In paraelectric materials dipoles are induced by the electric field. There are two polarization mechanisms for paraelectric materials. Electric polarization occurs when the electrons are no longer ordered symmetrically around the atomic cores. Ionic polarization takes place if positive and negative ions are shifted in the sublattices of the crystal. If an external field is applied, the dipoles of the materials become aligned and the external electrical field is weakened. After the electrical field is removed, the polarization of the material disappears as well. The typical polarization vs. field curve is depicted in Figure 1a. The dielectric constant of a paraelectric shows linear behaviour.

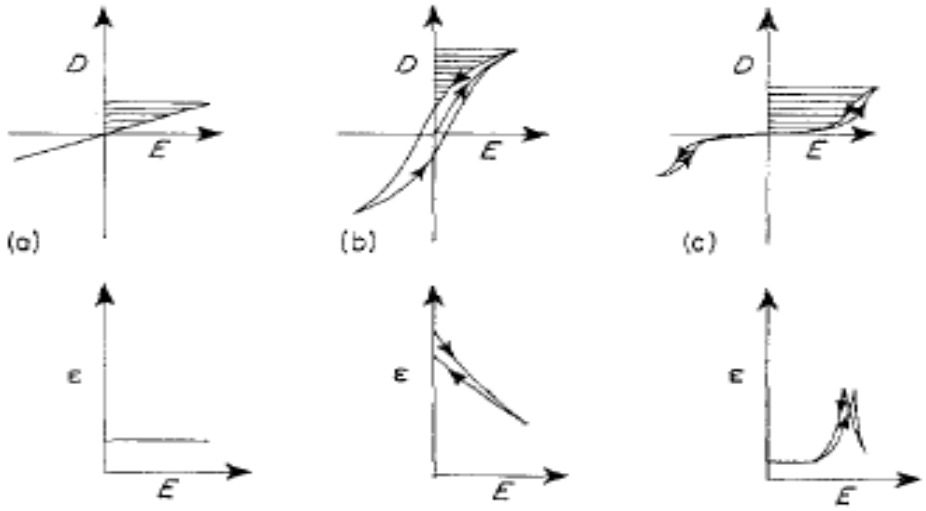

Figure 1: Typical dependence of electrical displacement D (polarization) and permittivity ε on an electric field for (a) paraelectric, (b) ferroelectric, and (c) antiferroelectric materials [3].

2.1.2. Ferroelectricity

Ferroelectric materials possess spontaneously generated dipoles, which can be oriented by an external electrical field. All ferroelectrics have symmetry groups that are non-centro symmetric. Areas in the material where the spontaneous polarization has the same direction and strength are called domains. They are separated by domain walls from regions where the spontaneous polarization has a different orientation. Whenever a field is present within a crystal (e.g. spontaneous polarization) a field opposed to it is generated at the surface of the crystal. To minimise the energy of this external field the domains within the crystal order themselves in an antiparallel direction, therefore decreasing the energy of the field. If heated above the Curie temperature, a structural phase transition takes place, the spontaneous polarization vanishes and the material becomes paraelectric. The dipoles in the material are aligned axially, if an external field is applied. This process is called poling. When removing the field, a remnant polarization remains. However, if a field of the opposite charge is applied, the polarization switches according to the field. By plotting the polarization against the applied field a characteristic hysteresis curve is achieved, as seen in Figure 1b.

The cross-hatched area represents the storage capacity of the material. All ferroelectric materials are pyroelectrics (polarization changes with temperature) and piezoelectrics (mechanical energy/ strain is transformed into electrical energy and vice versa). Due to the piezoelectric properties, strain is generated when an electrical field is applied to the material. This is mainly because of the switching of 90° domains during poling [4]. In regards to both polarization and permittivity, ferroelectrics show a diffuse behaviour.

2.1.3. Antiferroelectricity

In antiferroelectrical materials no net polarization is observed [5]. There is a polarization present within the material; however neighbouring areas have opposed directions of polarization [6]. This leads to a macroscopic polarisation which is zero. The antiparallel ordering of dipoles (directly responsible for the polarization) within antiferroelectric crystals is due to cation displacement (perovskite materials), ordering of H^+-ions (order–disorder transition compounds) or tilting of rod-like polar molecules within neighbouring regions (smectic liquid crystals).The orthorhombic cell which makes up the elementary cell (dotted line in Figure 2) has a centre of symmetry and therefore no de-alignment of charge takes place [7]. Due to the lacking symmetry centre antiferroelectrics are not piezoelectric. Antiferroelectric materials are also built up by domains.

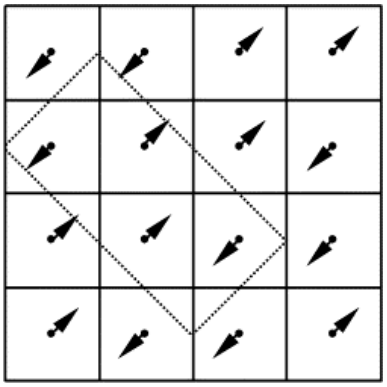

Figure 2 Antiparallel dipoles in an antiferroelectric material [5].

When an electrical field is applied, antiferroelectric materials react in a dielectric/linear manner at first. However, if a critical field strength (switching field) is reached, a phase transition to a ferroelectrical system occurs. This is possible because the antiferroelectric and the ferroelectric phase have very comparable free energies. At higher fields the parallel alignment of the dipoles is energetically favourable, which allows the material to achieve a net polarization diffuse to the applied field. When the applied field is reversed, the polarization returns first to zero retaining the antiparallel orientation and then switches direction according to the field. As depicted in Figure 1c, a double hysteresis loop occurs. Energy storage can be increased, if the switching field and the polarization are maximized. Also the energy loss is smaller in antiferroelectrical materials, as their hystereses are narrower than those of ferroelectrics. With the field-forced transition a large volume change occurs. Electrostrictive behaviour is observed in the materials. The direction of the strain is independent of the direction of the field. In some materials like lead zirconatetitanatetwo ferroelectric phases are separated by a morphotropic phase boundary (MPB). The transition is diffuse and there are configurations were both rombohedraland tetragonal ferroelectric regions coexist. The phase transition can be noticed in the peak of the dielectric constant of the antiferroelectric materials. This peak value can also be detected if the permittivity is measured against the temperature. It makes identifying phase transitions within the material relatively easy. Above the Curie temperature antiferroelectric materials are converted to paraelectric ones. When subjected to a sufficiently high electric field, electrical breakdown occurs within the material due to material failure or a short circuit. In antiferroelectrics electrical breakdown often occurs before the saturation polarization can be reached. The introduction of dopants is generally used to improve the performance of antiferroelectric materials.

2.2. Lead ZirconateTitanate (PZT)

PZT is a perovskite-type compound. The structure class is named after calcium titanate (perovskite) and has the general chemical formulaABO_3.Cations are at the A- and B-site (A-site cations having a bigger radius than B-site cations), while oxygen forms a network of corner sharing octahedra (see Figure 3) In PZT lead occupies the A-site (gray in Fig. 3), while zirconium and titanium occupy the B-site (turquoise in the figure).

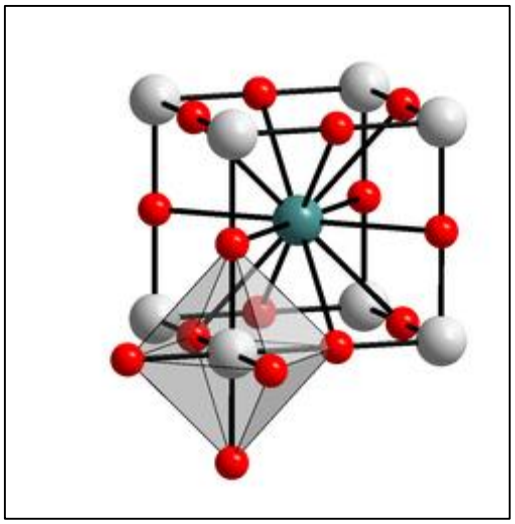

Figure 3 Perovskite structure; red= oxygen, gray= A-site cation, turquoise= B-site cation

The stability of perovskites is determined by the Goldschmidt factor or tolerance factor t.

$$t = \frac{(R_A + R_O)}{\sqrt{2}\,(R_B + R_O)}$$

In the equation R_A is the mean ionic radius of the A-site cations, R_B the mean ionic radius of the B-site cations and R_O the ionic radius of oxygen. The tolerance factor is an indicator how well two atoms are matched [7]. The better two atoms fit together (in terms if radius) the closer *t* is to unity (=1) and the unit cell ideally cubic. A difference in radius can lead to the distortion of the unit cell. Within different publication various values have been deemed acceptably stable for synthesized perovskite materials [8]. Goldschmidt determined a range between 0, 77 and 1 acceptable [9]. Lower values represent an antiferroelectric system and higher values stand for a ferroelectric system.

The research concerning PZT was first done byShirane, Suzuki and Takeda [10]. They discovered that compositions with less than 10 mol percent titanium were antiferroelectric in nature with orthorhombic symmetry, whereas compositions with higher titanium content were ferroelectric. This is due to the titanium displacement in the lattice, which allows better long range interactions of the oxygen atoms. This stabilizes the ferroelectric phase.

Favoring the antiferroelectricity of PZT is the lead displacement that occurs within the lattice. This leads to a tilting of oxygen octahedra, which in turn disturbs the long range interactions of the oxygen atoms and destabilizes the ferroelectrical phase. A phase diagram of PZT is shown in Figure 4 [11].

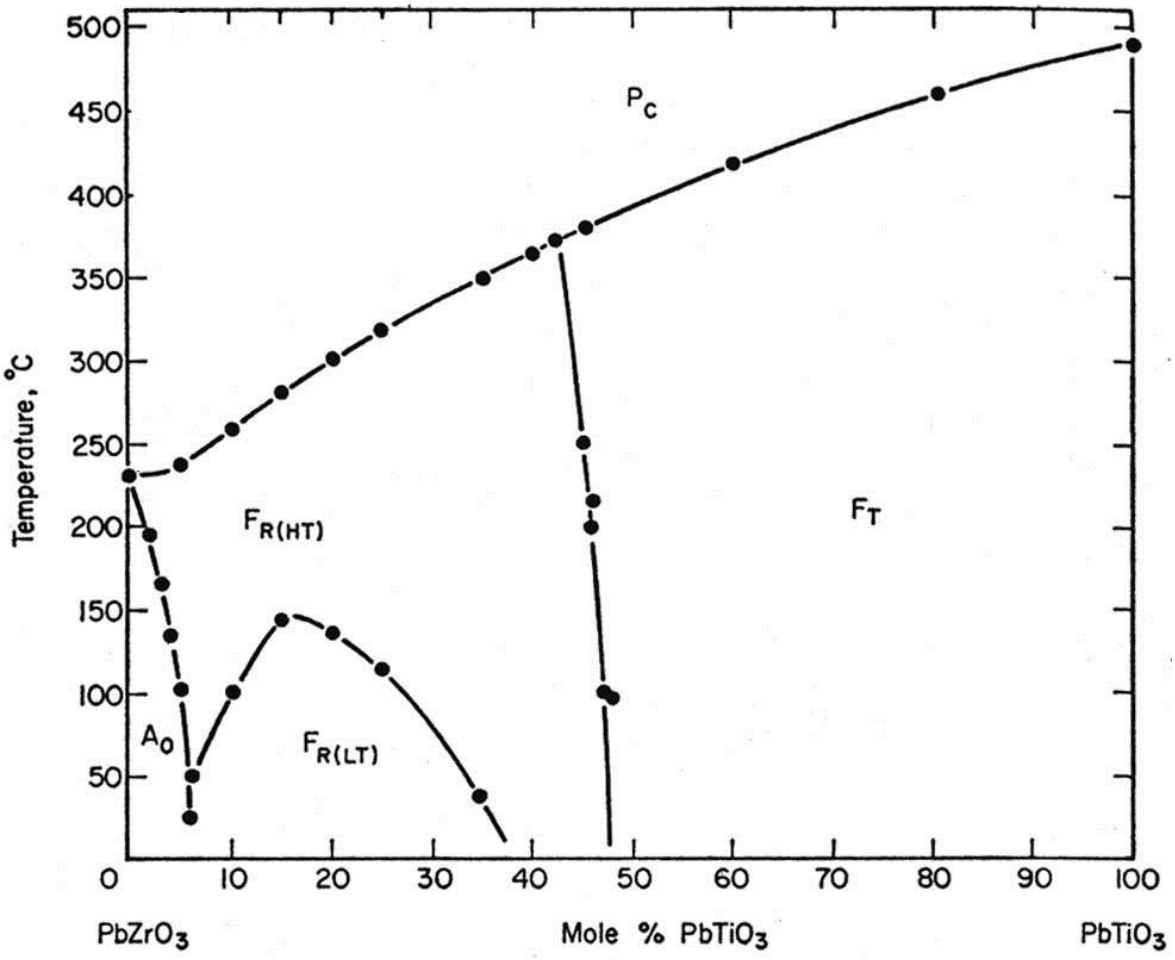

Figure 4: Phase diagram of PZT; with: P_C= cubic, paraelectric; $F_{R\,(HT)}$ =rombohedral, high temperature, ferroelectric; $F_{R\,(LT)}$ =rombohedral, low temperature, ferroelectric; F_T= tetragonal, ferroelectric; A_O= orthorhombic, antiferroelectric] [11]

A morphotropic phase boundary (present in PZT between the rhombohedral and the tetragonal ferroelectric phases) is separating two phases which have equal Gibbs energy. The exact boundary has not been determined for PZT, but lies between 45 and 50% titanium content.

There are two theories concerning the compositions in between. The more popular theory says that close to the MPB both tetragonal and rhombohedral phases are both present at the same time [12].

The other theory postulates that there is a monoclinic phase between the tetragonal and the rhombohedralone [13]. At the MPB, properties such as permittivity increase drastically, which is the reason for close research of compositions in its vicinity.

B. Jaffe, R. S. Rothand S. Marzullo [14] investigated the piezoelectric properties of PZT.Their interest in PLZ was founded in the high Curie point between 220°C and 490°C (see Figure 4), depending on composition, when compared to the most used system of the time: barium titanate (Curie point at 120°C). At the Curie point a loss of polarization occurs and the material becomes paraelectric. A polarization of the material is necessary for the piezoelectrical effect to occur. Therefore PZT was usable in a wider temperature range than barium titanate, while still showing good electrical properties (permittivity, loss factor, and polarization). PZT is used today as piezoelectric material in sensors, actuators, transducers and in sonar systems [15].

2.3. Lead lanthanum zirconatetitanate (PLZT)

To further increase the stable temperature range and the electrical properties various dopants were investigated in combination with the PZT system. Probably the most well researched one is doping with lanthanum oxide. The so formed lead lanthanum zirconatetitanate (PLZT) has the perovskite structure as described above, with lanthanum substituting lead on A-site. Due to the difference in valency between lead and lanthanum compensation by cation-vacancies occurs in the material. The phase diagram is shown below (Figure 5)· [16]. The addition of lanthanum serves to stabilize the antiferroelectrical phase. This is especially interesting for compositions with higher titanium content, as the materials are easier to sinter and have a lower switching field if lanthanum is added. The transition temperature also lowers greatly with increasing titanium content. The dipoles of PLZT occur because the lead atoms divert form the theoretical position in a spherical manner. This displacement leads to tilting of the oxygen octahedraand therefore an unbalanced distribution of the charge, resulting in dipoles present in both PZT and PLZT [14].

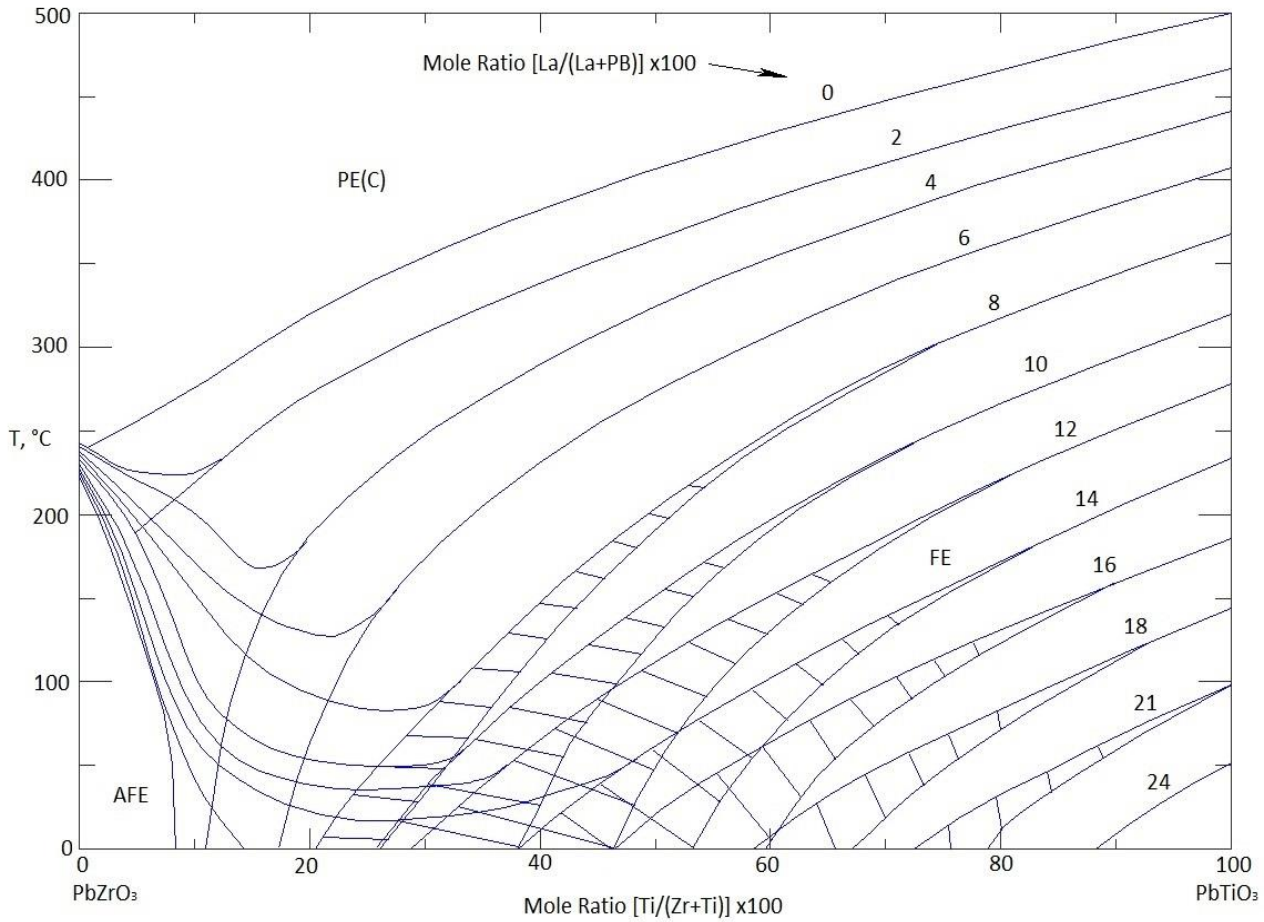

Figure 5 Phase diagram of PLZT; PE_C= paraelectrical, cubic phase; AFE= Antiferroelectric phase; FE= ferroelectric phase [16]

The addition of lanthanum also leads to a decrease of sintering temperature. This made the production of transparent ceramic materials easier, which can be used in electro-optical applications [16]. Before the discovery of PLZT, mostly single crystals could be used for this purpose [16]. The usage of PLZT is favourable due to a less sophisticated synthesis and a broader range of size.

2.4. Influence of dopants on PZT/PLZT

The term dopant is used when 5 or less atomic percent of a substituent are introduced to a system [17]. When more is added one speaks of a modified system.

In general, there are these factors influencing the properties of a doped system: the ionic radius, atomic mass and number of valence electrons of the dopant in comparison with the atom that is substituted. Independent of the valency and the site the dopant is introduced, there are a few trends observable. If the tolerance factor of a perovskite system is decreased, the antiferroelectrical phase is stabilized. If there is an increase in the tolerance factor, the ferroelectric phase is stabilized. Also, if the doping ion increases the mean radius on either A- or B-site, the unit cell volume increases as well. The reversed effect is also observed. On the other hand the atomic mass influences the vibrational or phonon spectrum of a crystal, which in turn is relevant for the transition between ferroelectric (or antiferroelectric) phases and the paraelectric phase. The influence of the valence factor will be discussed in the paragraphs below. It should be noted that in almost all cases there are at least two of the factors named above involved in any doping concept. It is hardly possible to exactly discern the individual influence of one factor because usually a substituent with a larger atomic mass exhibits a larger ionic radius, too.

2.4.1. Aliovalent dopants

Aliovalent dopants differ in the valency from the ion they are replacing. This can lead to either donor doping, where cation vacancies are created and the dopant has a higher valency than the substituted ion; or to acceptor doping where oxygen vacancies are created to compensate the charge difference and the dopant has a lower valency. Prime example of this is the doping of PZT with lanthanum oxide forming PLZT. It is generally agreed that due to the observed change of lattice parameters and cell volume, lanthanum is an A-site dopant. The dopant ion La^{3+} has a higher oxidation number than Pb^{2+}. Due to this fact there are cation vacancies introduced to the system in order to remain neutral. These cationvacancies shift the Schottky equilibrium of the compound, which causes a reduction of oxygen vacancies. This reduction of oxygen vacancies in the lattice increases the dielectric constant [18].

Another factor influenced by decreased oxygen vacancy concentration is the mobility of the domain walls as a lower oxygen vacancy concentration facilitates domain wall movement by reducing domain wall pinning [19]. If Nb^{5+} is substituted for Ti^{4+} or Nd^{3+} for Pb^{2+} a so called soft PZT is formed, with easily movable domain walls.

This leads to higher piezoelectric coefficients, due to the easier switching of the domains. Soft PZT ceramics are often used as hydrophones and other sensors [15]. If, on the other hand, Fe^{3+} is substituted for Ti^{4+} a hard PZT is produced. These types of ceramic will not depole under mechanical load. Hard PZT ceramics are used in high power transducers [15].

2.4.2. Isovalent dopants

Isovalent dopants differ in their atomic radius and molecular mass, but not in the valency from the element they are substituting. An example of this kind of doping is the substitution of lead with strontium in PLZT [19]. The authors claim that this leads to a stabilization of the antiferroelectrical phase and the creation of a second, tetragonal antiferroelectric phase close to the ferroelectric phase.

With increasing strontium content the unit cell becomes more distorted, leading to a tetragonal symmetry. At first this leads to an increase in the dielectric constant, because the composition moves closer to the MPB. If a certain percentage of strontium doping is exceeded, the increased tetragonal nature of the cell causes the composition to move away from the MPB and the dielectric constant becomes lower again [20]. Also the switching field is lowered, the hysteresis curve becomes narrower and the saturation polarization decreases. It was shown that strontium doping increases the particle size, has no effect on the densification behavior and causes square-shaped grains to appear [18].

3. Experimental Part

3.1. Powderprocessing

The following chemicals were used for the synthesis in this work.

- Lead oxide (Pb_3O_4); Penox GmbH, Köln/Deutz, Germany
- Lanthanumoxide (La_2O_3); Treibacher Industrie AG, Treibach, Austria
- Hafnium oxide (HfO_2); (99,0%) Heraeus, Karlsruhe, Germany
- Zirconiumoxide (ZrO_2); MEL Chemicals, Manchester, United Kingdom
- Titaniumoxide (TiO_2); (99, 8 %)Tronox Pigments, Holland BV

Before usage the chemicals were dried at 220°C and stored in adesiccator while cooling. An Acculab scale from Satorius Group ACL was used for the weighting. For milling a Pulverisette 7 planetary ball mill from Fritsch Premium Line was utilized.

Powders were prepared using the mixed oxide method, in which the oxide powders of the educts are first mixed and subsequently calcinated and sintered. For all samples 50 g of the undoped and 15 g of the doped powders were synthesised. As the samples with higher hafnium concentration were prepared at another time than those with lower concentrations, two samples with 10 mol% hafnium were prepared and compared to determine the influence of the different preparation time. The results of both samples differ by maximal 5%. Therefor only one of the 10% hafnium samples is shown here due to the good compliance. The exact preparation is described in the following section.

3.1.1. Net weightcalculation

There were two series prepared. The first one (PLZT_90/10_xHf) was weighted in following the formula [1] where V_{Pb}^{II} stands for the Pb-vacancies created by lanthanum. Samples with x=0 to x=0, 3 were prepared.

$$Pb_{0,91}La_{0,06}V_{Pb}^{II}{}_{0,03}(Hf_xZr_{1-x})_{0,9}Ti_{0,1} \quad [1]$$

The equations used to calculate the net weight for the educts will be explained using the sample with 1 mol% of hafnium doping (x=0,01):

For x=0,01 formula [1] changes to: $Pb_{0,91}La_{0,06}V_{Pb}^{II}{}_{0,03}Hf_{0,009}Zr_{0,891}Ti_{0,1}$

The molecular mass of the product is 332,56 g/mol. A total mass of 15g is desired.Following the equation $n=\frac{m}{M}$; 0,0451 mol of the product will be needed.

Subsequently 0,0451*0,91 mol of Pb_3O_4, 0,0451*0,06 mol of La_2O_3, 0,0451*0,009 mol of HfO_2, 0,0451*0,891 mol of ZrO_2 and 0,0451*0,1 mol TiO_2 are needed. Using the equation above, the net weight can be determined. One weight-percent of leadoxide was added as excess. The net weightfor all samples of the PLTZ_90/10_xHf series can be seen in Table 2. In Table 1 the data for the product powders is listed.

Table 1 Data of the product powders PLZT_90/10_xHf

Name	Hfcontent [% dopant]	M [g/mol]	n[mol]	m [g]
PLZT_90/10_0Hf	0	331,77	0,0452	50
PLZT_90/10_1Hf	1	332,56	0,0451	15
PLZT_90/10_2Hf	2	333,34	0,0450	15
PLZT_90/10_4Hf	4	334,91	0,0448	15
PLZT_90/10_6Hf	6	336,49	0,0446	15
PLZT_90/10_8Hf	8	338,06	0,0444	15
PLZT_90/10_10Hf	10	339,63	0,0442	15
PLZT_90/10_20Hf	20	347,48	0,0432	15
PLZT_90/10_25Hf	25	351,41	0,0427	15
PLZT_90/10_30Hf	30	355,33	0,0422	15

Table 2 Net weight of the PLZT_90/10_xHf series

	Pb_3O_4	La_2O_3	HfO_2	ZrO_2	TiO_2
M [g/mol]	669,60	325,82	210,49	123,22	79,88
PLTZ_90/10_0Hf					
Composition [mol%]	0,91	0,06	0,00	0,90	0,10
n [mol]	0,0457	0,0045	0,0000	0,1356	0,0151
m [g]	30,916	1,473	0,000	16,713	1,204
PLZT_90/10_1Hf					
Composition [mol%]	0,91	0,06	0,01	0,89	0,10
n [mol]	0,0137	0,0014	0,0004	0,0402	0,0045
m [g]	9,253	0,441	0,085	4,952	0,360
PLZT_90/10_2Hf					
Composition [mol%]	0,91	0,06	0,02	0,88	0,10
n [mol]	0,0136	0,0014	0,0008	0,0397	0,0045
m [g]	9,231	0,440	0,170	4,890	0,359

PLZT_90/10_4Hf	Pb_3O_4	La_2O_3	HfO_2	ZrO_2	TiO_2
Composition [mol%]	0,91	0,06	0,04	0,86	0,10
n [mol]	0,0136	0,0013	0,0016	0,0387	0,0045
m [g]	9,188	0,438	0,339	4,768	0,358
PLZT_90/10_6Hf					
Composition [mol%]	0,91	0,06	0,05	0,85	0,10
n [mol]	0,0135	0,0013	0,0024	0,0377	0,0045
m [g]	9,145	0,436	0,507	4,647	0,356
PLZT_90/10_8Hf					
Composition [mol%]	0,91	0,06	0,07	0,83	0,10
n [mol]	0,0135	0,0013	0,0032	0,0367	0,0044
m [g]	9,102	0,434	0,672	4,527	0,354
PLZT_90/10_10Hf					
Composition [mol%]	0,91	0,06	0,09	0,81	0,10
n [mol]	0,0134	0,0013	0,0040	0,0358	0,0044
m [g]	9,060	0,432	0,837	4,408	0,353
PLZT_90/10_20Hf					
Composition [mol%]	0,91	0,06	0,18	0,72	0,10
n [mol]	0,0131	0,0013	0,0078	0,0311	0,0043
m [g]	8,856	0,422	1,636	3,830	0,345
PLZT_90/10_25Hf					
Composition [mol%]	0,91	0,06	0,23	0,68	0,10
n [mol]	0,0129	0,0013	0,0096	0,0288	0,0043
m [g]	8,757	0,417	2,022	3,550	0,341
	Pb_3O_4	La_2O_3	HfO_2	ZrO_2	TiO_2
PLZT_90/10_30Hf					
Composition [mol%]	0,91	0,06	0,27	0,63	0,10
n [mol]	0,0128	0,0013	0,0114	0,0266	0,0042
m [g]	8,660	0,413	2,399	3,277	0,337

For the second series (PLZT_85/15_xHf) the following formula [2] was used:

$$Pb_{0,91}La_{0,06}V_{Pb}^{II}{}_{0,03}(Hf_xZr_{1-x})_{0,85}Ti_{0,15} \qquad [2]$$

Samples with x=0,0 to x=0,3 were produced. The calculation of the net weight is following the same process used for the PLZT_90/10_xHf series. The calculated net weight can be seen in Table 4. The data for the products can be viewed in Table 3.

Table 3 Data of the product powders PLZT_85/15_xHf

Name	Hfcontent [% dopant]	M [g/mol]	n[mol]	m [g]
PLZT_85/15_0Hf	0	329,60	0,1517	50
PLZT_85/15_1Hf	1	330,35	0,0454	15
PLZT_85/15_2Hf	2	331,09	0,0453	15
PLZT_85/15_4Hf	4	332,57	0,0451	15
PLZT_85/15_6Hf	6	334,06	0,0449	15
PLZT_85/15_8Hf	8	335,54	0,0447	15
PLZT_85/15_10Hf	10	337,02	0,0445	15
PLZT_85/15_20Hf	20	344,44	0,0435	15
PLZT_85/15_25Hf	25	348,15	0,0431	15
PLZT_85/15_30Hf	30	351,86	0,0426	15

Table 4 Net weight of the PLZT_85/15_xHf series

	Pb_3O_4	La_2O_3	HfO_2	ZrO_2	TiO_2
M [g/mol]	669,60	325,82	210,49	123,22	79,88
PLTZ_85/15_0Hf					
Composition [mol%]	0,91	0,06	0,00	0,85	0,15
n [mol]	0,0460	0,0046	0,0000	0,1289	0,0228
m [g]	31,120	1,483	0,000	15,888	1,818
PLZT_85/15_1Hf					
Composition [mol%]	0,91	0,06	0,01	0,84	0,15
n [mol]	0,0138	0,0014	0,0004	0,0382	0,0068
m [g]	9,315	0,444	0,081	4,708	0,544
PLZT_85/15_2Hf					
Composition [mol%]	0,91	0,06	0,02	0,83	0,15
n [mol]	0,0137	0,0014	0,0008	0,0377	0,0068
m [g]	9,294	0,443	0,162	4,650	0,543
PLZT_85/15_4Hf					
Composition [mol%]	0,91	0,06	0,03	0,82	0,15
n [mol]	0,0137	0,0014	0,0015	0,0368	0,0068
m [g]	9,253	0,441	0,323	4,535	0,540
PLZT_85/15_6Hf					
Composition [mol%]	0,91	0,06	0,05	0,80	0,15
n [mol]	0,0136	0,0013	0,0023	0,0359	0,0067
m [g]	9,211	0,439	0,482	4,421	0,538
PLZT_85/15_8Hf					
Composition [mol%]	0,91	0,06	0,07	0,78	0,15
n [mol]	0,0136	0,0013	0,0030	0,0350	0,0067
m [g]	9,171	0,437	0,640	4,308	0,536

PLZT_85/15_10Hf	Pb_3O_4	La_2O_3	HfO_2	ZrO_2	TiO
Composition [mol%]	0,91	0,06	0,09	0,77	0,15
n [mol]	0,0135	0,0013	0,0038	0,0340	0,0067
m [g]	9,130	0,435	0,796	4,195	0,533
PLZT_85/15_20Hf					
Composition [mol%]	0,91	0,06	0,17	0,68	0,15
n [mol]	0,0132	0,0013	0,0074	0,0296	0,0065
m [g]	8,934	0,426	1,558	3,649	0,522
PLZT_85/15_25Hf					
Composition [mol%]	0,91	0,06	0,21	0,64	0,15
n [mol]	0,0131	0,0013	0,0092	0,0275	0,0065
m [g]	8,839	0,421	1,927	3,384	0,516
PLZT_85/15_30Hf					
Composition [mol%]	0,91	0,06	0,26	0,60	0,15
n [mol]	0,0129	0,0013	0,0109	0,0254	0,0064
m [g]	8,745	0,417	2,288	3,126	0,511

3.1.2. Powderprocessing

The educt powders were ball milled using tungsten-carbide vials und balls with a diameter of 0,5 cm. The samples were milled for 30 minutes at 300 rotations per minute (rpm) without external cooling. Ethanol was used as liquid medium.

The samples were dried at 120 °C for overnight and sieved (test sieve/ 500 µm).

Subsequently the samples were calcinated in a chamber furnace(Nabertherm N7H) using the program shown in Figure 6. It should be noted that the cooling rate differed from the theoretical value due to passive cooling. This is true for all furnace programs used in this work.

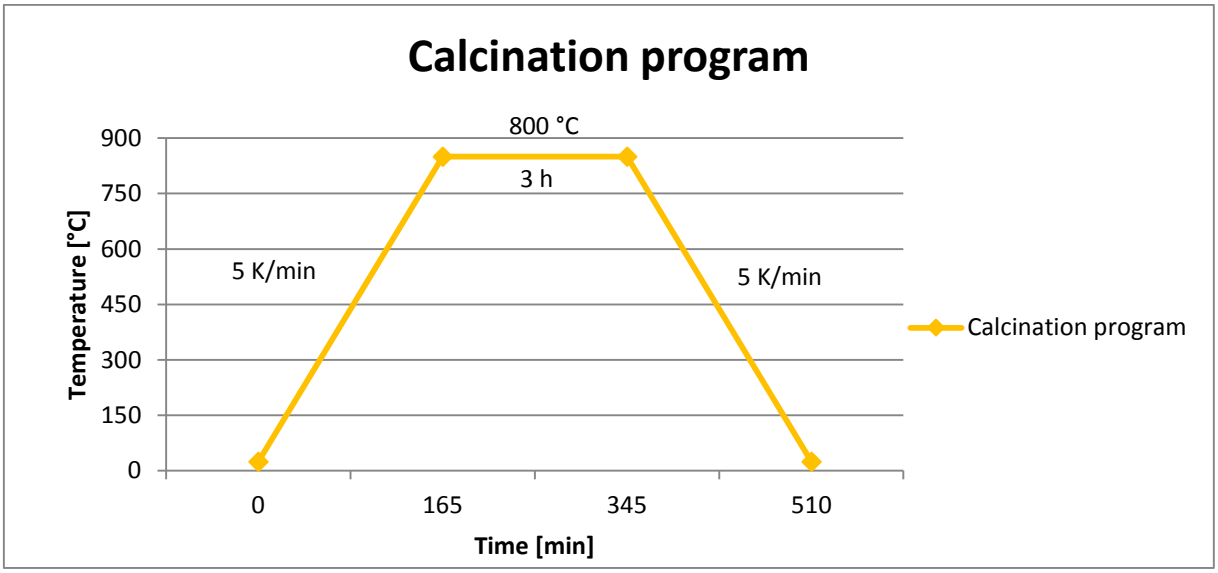

Figure 6 Calcination program

The powders were sieved (test sieve, 500 µm), weighted and samples for XRD measurements were taken. Results will be shown later in this work. Afterwards the samples are milled again (30 min, 300 rpm; in ethanol), dried at 120 °C overnight and sieved (test sieve, 500 µm).

Then 5 wt% binder (Polyethylenglycol (PEG) 20.000; 30 wt% in water) were added. The samples were granulated and dried for 30 minutes at 80°C. Fine sieving was done by subsequent use of test sieves with 500 µm; 380 µm and 180 µm. The whole powder was sieved through the sieve with the largest mesh size and partly through the 380 µm sieve. Subsequently the granulate on the 380 µm and the 180 µm sieve was mixed again and used for pressing.

3.2. Preparation of green bodies and sintering

The powders were pressed to cylindrical green bodies with a height of 1 mm and a diameter of 13 mm. A uniaxial press was used and the samples were pressed at 150 MPa for 5 minutes. Altogether 6 green bodies per composition were prepared. The weight of the green bodies was determined to calculate the weight loss during debindering, which was done separately before sintering using the program described in Figure 7.

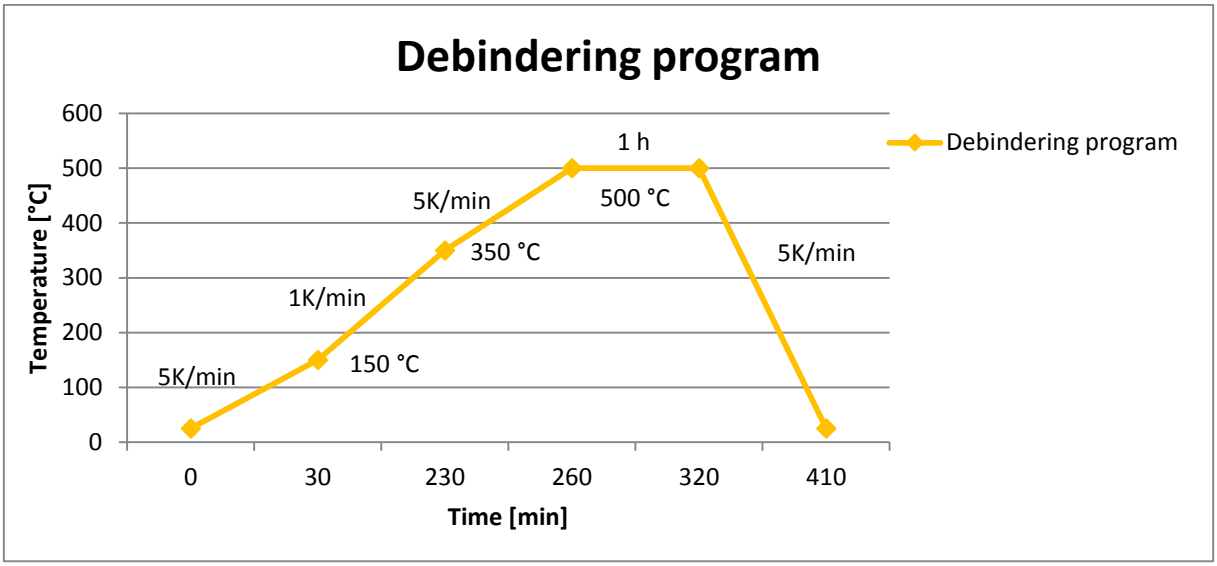

Figure 7 Debindering program

After removing the binder the samples were weighted to determine the weight loss during sintering and prepared for sintering.

The following set-up was used: On an aluminium oxide plate some ZrO_2 powder was spread followed by stacking 6 green bodies. Those were separated by ZrO_2 powder to guarantee better separation of the samples after sintering. Around the stack a ring of not calcinated lead-zirconate powder was arranged to prevent lead loss of the samples. Over each stack two aluminium oxide crucibles were positioned. The samples were sintered according to the program described in Figure 8.

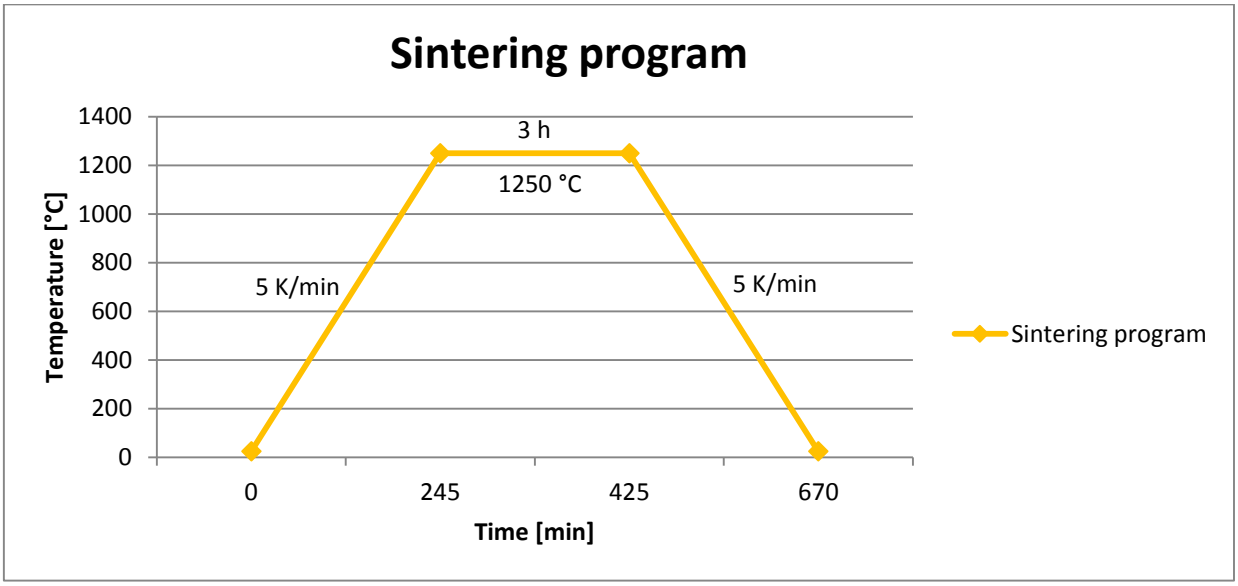

Figure 8 Sintering program

After sintering the samples were separated and cleaned to remove excess ZrO_2.

3.3. Analytical Methods

3.3.1. Gravimetricmeasurements

The sample weight was used to determine the loss of material during the preparation progress. Regarding this information it was decided whether the loss due to lead volatilization was still acceptable, or if process conditions had to be adjusted. This was done for both calcination and sintering process.

3.3.2. Densitymeasurements

The quality of the sintering process was estimated by measuring the density of the samples. Three different approaches were used.

Geometric density:

The diameter and height of each sample were measured three times and an average for each was calculated. Afterwards using the mass of the sintered specimen the density was calculated according to the following formula [3]:

$$\rho = \frac{m[g]}{V[cm^3]} \qquad [3]$$

Density using Archimedes principle:

The density was determined using an Archimedes scale (Mettler Toledo; XS204 Delta Range). First the samples were weighted. Subsequently they were immersed in distilled water and weighted again. The difference in mass, due to the buoyancy of the sample, and the density of the liquid were used to calculate the density.

$$\rho = \frac{m_d * \rho_L}{m_d - m_w} \qquad [4]$$

m_d= mass of dry sample m_w= mass of the sample in liquid

ρ_L= density of the liquid (water) ρ= density

Theoretical density/ X-ray density:

For comparison the theoretical density was calculated using the unit cell volume gathered by XRD measurements and following calculation [5]:

$$\rho = \frac{Z*M}{V*N_A} \qquad [5]$$

Z= formula units per unit cell M=molecular weight of the sample

V= Volume of the unit cell N_A= Avogadro constant

3.3.3. X-Ray diffractionmeasurements

The measurements were done on a Bruker AXS D5005 y-y. The obtained data was analyzed in the X'PertHighScore Plus software, using Rietveld method. θ/2θ measurements were done after calcinating and sintering to determine the efficiency of both processes. The incorporation of hafnium into the crystal structure was also checked by identifying secondary phases containing hafnium. If no such phases could be found it was assumed that the hafnium was incorporated.

Regarding the data obtained by the Rietveld method lattice parameters, cell volume and theoretical density were determined and compared.

The Goldschmidt's tolerance factor was also calculated:

$$t = \frac{r_A + r_O}{\sqrt{2} * (r_B + r_O)}$$

r_A= radius of the A-site atom(s) r_O= radius of oxygen atom

r_B= radius of the B-site atom(s)

3.3.4. Small signalmeasurements

For the electrical measurements silver paste was applied to the sample surface and dried at 80° C for 30 minutes. Then the capacityand the loss factor were measured on a Hewlett Pickard- 4192A Lf Impedance Analyser at 1kHz and at 100kHz of the unpoled samples.

The permittivity of the samples was calculated from the capacity, the diameter and thickness.

3.3.5. High signalmeasurements

3.3.5.1. Polarization

The polarization curve of a material shows its behavior in an electrical field. An aixACCT TF Analyzer 2000 was used to measure the polarization versus the electrical field.

3.3.5.2. Permittivity versus Temperature

Permittivity versus temperature measurements were done atan Alpha, Beta Analyzer. Each sample was measured at 1 MHz, 100kHz, 10kHz, 1 kHz and 0,1 kHz over a temperature range from -50°C to 300°C. The loss factor of the samples was also determined over the same range. The gained data can be viewed in annex 1 for both series.

3.3.6. Electronmicroscopy

SEM-measurements were done on a Zeiss Ultra 55 to determine the influence of hafnium-doping on grain growth and the existence of secondary phases.

The methods used were SE (secondary electrons) and BSE (back scattered electrons) spectroscopy for studies of the topography (pores, grain connections).

EDX (energy dispersive x-ray) analysis was used to obtain a rough overview of the composition of the material. Specific values could not be obtained due to interference of the dopant with the matrix.

Channeling Contrast Mode was applied to observe the orientation and the domain structure of the samples.

The average grain size of the samples was determined using the line cut method and the intercept method described in DIN 50601 [21]. The imaging conditions of the individual micrographs can be seen at the bottom of each picture

4. Results and discussion

4.1. Results

The data shown below is if not otherwise noted a calculated average. All 6 samples of the same composition were measured separately and then the average was formed. This is also true for values that were calculated from data shown here (e.g.: permittivity), as six values were calculated and then averaged.

4.1.1. Gravimetricmeasurements

The weight loss during calcination is presented in Table 5 for PLZT_90/10_xHf and in Table 6 for PLZT_85/15_xHf. For an ideal reaction during calcinations only oxygen should be liberated (theoretical values inTable 5 and Table 6.)

Table 5 Weight loss calcinating PLZT_90/10_xHf

Sample	Theoreticalweightloss [g]	Experimental weightloss [g]	Difference Theo/exp. [g]	Difference theo/exp. [%]
PLZT_90/10_0Hf	1,0375	0,9565	0,0810	7,81
PLZT_90/10_1Hf	0,3105	0,2822	0,0283	9,11
PLZT_90/10_2Hf	0,3098	0,3151	-0,0053	-1,71
PLZT_90/10_4Hf	0,3083	0,2988	0,0095	3,08
PLZT_90/10_6Hf	0,3069	0,3279	-0,0210	-6,84
PLZT_90/10_8Hf	0,3055	0,2879	0,0176	5,76
PLZT_90/10_10Hf	0,3048	0,3169	-0,0121	-3,97
PLZT_90/10_20Hf	0,2968	0,3119	-0,0151	-5,09
PLZT_90/10_25Hf	0,2937	0,3060	-0,0123	-4,19
PLZT_90/10_30Hf	0,2904	0,3016	-0,0112	-3,86

Table 6 Weight loss calcinating PLZT_85/15_xHf

Sample	Theoretical weight loss [g]	Experimental weight loss [g]	Difference theo/exp [g]	Difference theo/exp [%]
PLZT_85/15_0Hf	1,0443	0,9891	0,0552	5,29
PLZT_85/15_1Hf	0,3126	0,3256	-0,013	-4,16
PLZT_85/15_2Hf	0,3119	0,3709	-0,059	-18,92
PLZT_85/15_4hf	0,3105	0,3386	-0,0281	-9,05
PLZT_85/15_6Hf	0,3091	0,3400	-0,0309	-10,00
PLZT_85/15_8Hf	0,3078	0,3436	-0,0358	-11,63
PLZT_85/15_10Hf	0,3064	0,3264	-0,02	-6,53
PLZT_85/15_20Hf	0,2998	0,3296	-0,0298	-9,94
PLZT_85/15_25Hf	0,2966	0,3250	-0,0284	-9,58
PLZT_85/15_30Hf	0,2935	0,3290	-0,0355	-12,10

The weight loss for all doped samples of the PLZT_85/15_xHf series is lower than the calculated value. There was no complete formation of the product compound during calcination. Most likely the chosen temperature was not high enough to enable a complete reaction. The process was not altered because XRD analysis of the sintered samples showed that the reaction was competed during sintering.

The weight loss during sintering is shown in Table 7 for PLZT_90/10_xHf and in Table 8 for PLZT_85/15_xHf. All samples were measured, but only the average for each composition is shown. Theoretically no weight loss should occur during sintering.

Table 7 Weight loss sintering PLZT_90/10_xHf

Sample	m (before) [g]	m (after) [g]	Δ m [g]	Δ m [%]
PLZT_90/10_0Hf	0,746	0,727	0,019	2,60
PLZT_90/10_1Hf	0,756	0,741	0,015	2,00
PLZT_90/10_2Hf	0,762	0,738	0,024	3,14
PLZT_90/10_4Hf	0,759	0,746	0,012	1,61
PLZT_90/10_6Hf	0,758	0,743	0,015	1,93
PLZT_90/10_8Hf	0,757	0,726	0,031	4,10
PLZT_90/10_10Hf	0,768	0,748	0,020	2,61
PLZT_90/10_20Hf	0,753	0,736	0,017	2,26
PLZT_90/10_25Hf	0,759	0,747	0,013	1,67
PLZT_90/10_30Hf	0,749	0,744	0,005	0,66

Table 8 Weight loss sintering PLZT_85/15_xHf

Sample	m (before) [g]	m (after) [g]	Δ m [g]	Δ m [%]
PLZT_85/15_0Hf	0,760	0,743	0,016	2,16
PLZT_85/15_1Hf	0,756	0,726	0,030	3,99
PLZT_85/15_2Hf	0,758	0,756	0,002	0,29
PLZT_85/15_4hf	0,758	0,757	0,001	0,13
PLZT_85/15_6Hf	0,758	0,735	0,024	3,13
PLZT_85/15_8Hf	0,759	0,733	0,026	3,43
PLZT_85/15_10Hf	0,760	0,747	0,013	1,69
PLZT_85/15_20Hf	0,759	0,754	0,005	0,65
PLZT_85/15_25Hf	0,761	0,757	0,003	0,44
PLZT_85/15_30Hf	0,760	0,746	0,014	1,88

4.1.2. Densitymeasurements

Shown here are only the calculated averages for each composition (Table 9; Table 10). The relative density below is the ratio of theoretical density to density calculated applying the Archimedes principle.

Table 9 Density of PLZT_90/10_xHf

Sample	Theoretical Density [g/cm³]	Geometric density [g/cm³]	Archimedes density [g/ cm³]	geom./Arch.-Density ratio [%]	Relative density [%]
PLZT_90/10_0Hf	7,84	7,35	7,48	98,2	95,39
PLZT_90/10_1Hf	7,88	7,58	7,55	100,4	95,77
PLZT_90/10_2Hf	7,88	7,55	7,60	99,4	96,38
PLZT_90/10_4Hf	7,92	7,72	7,64	101,3	96,42
PLZT_90/10_6Hf	7,97	7,73	7,77	99,5	97,40
PLZT_90/10_8Hf	8,01	7,62	7,70	99,1	96,07
PLZT_90/10_10Hf	8,03	7,81	7,84	99,6	97,68
PLZT_90/10_20Hf	8,23	7,96	7,93	100,3	96,37
PLZT_90/10_25Hf	8,33	8,22	8,11	101,3	97,41
PLZT_90/10_30Hf	8,42	8,34	8,22	101,5	97,56

Table 10 Density of PLZT_85/15_xHf

Sample	Theoretical Density [g/cm³]	Geometric density [g/cm³]	Archimedes density [g/cm³]	geom./Arch.-Density ratio [%]	Relative density [%]
PLZT_85/15_0Hf	7,83	7,59	7,62	99,7	97,25
PLZT_85/15_1Hf	7,90	7,60	7,58	100,2	95,95
PLZT_85/15_2Hf	7,87	7,77	7,81	99,6	99,22
PLZT_85/15_4Hf	7,95	7,81	7,76	100,7	97,58
PLZT_85/15_6Hf	8,00	7,71	7,72	99,9	96,53
PLZT_85/15_8Hf	8,04	7,74	7,76	99,8	96,53
PLZT_85/15_10Hf	8,03	7,89	7,64	103,3	95,20
PLZT_85/15_20Hf	8,21	7,99	7,83	102,2	95,32
PLZT_85/15_25Hf	8,30	8,02	8,07	99,3	97,22
PLZT_85/15_30Hf	8,40	8,04	8,14	98,8	96,86

4.1.3. X-Ray diffractionmeasurements

The XRD spectra of the PLZT_90/10_xHf series are shown in Figure 9 and Figure 10. The main PLZT peak at approximately 30 °2θ is clearly visible. Next to it (indicated by *) are secondary phase peaks. They were assigned to ZrO_2 and $PbHfO_3$.

In Figure 11 and Figure 12 the same data for the PLZT_85/15_xHf series is shown. The main peak is clearly visible, but there are the same secondary phases present (indicated by *) as in the PLZT_90/10_xHf series.

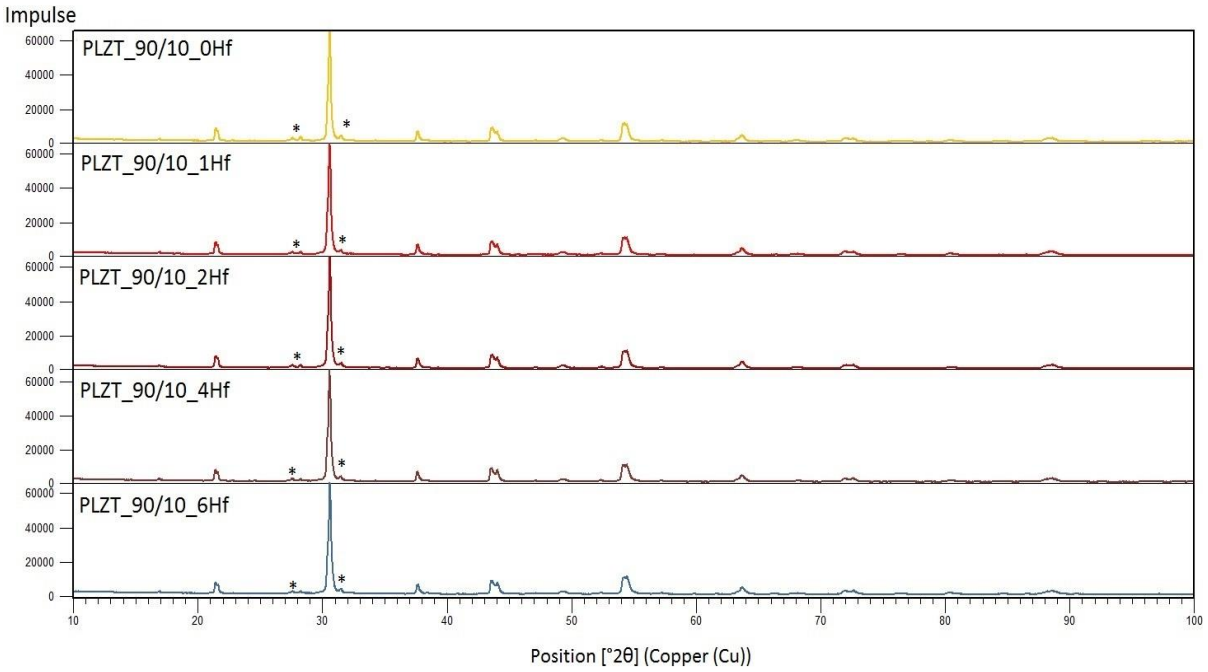

Figure 9 XRD Spectra of calcinated PLZT_90/10_xHf (x: 0->6Hf) *= secondary phases ($PbHfO_3$ and ZrO_2)

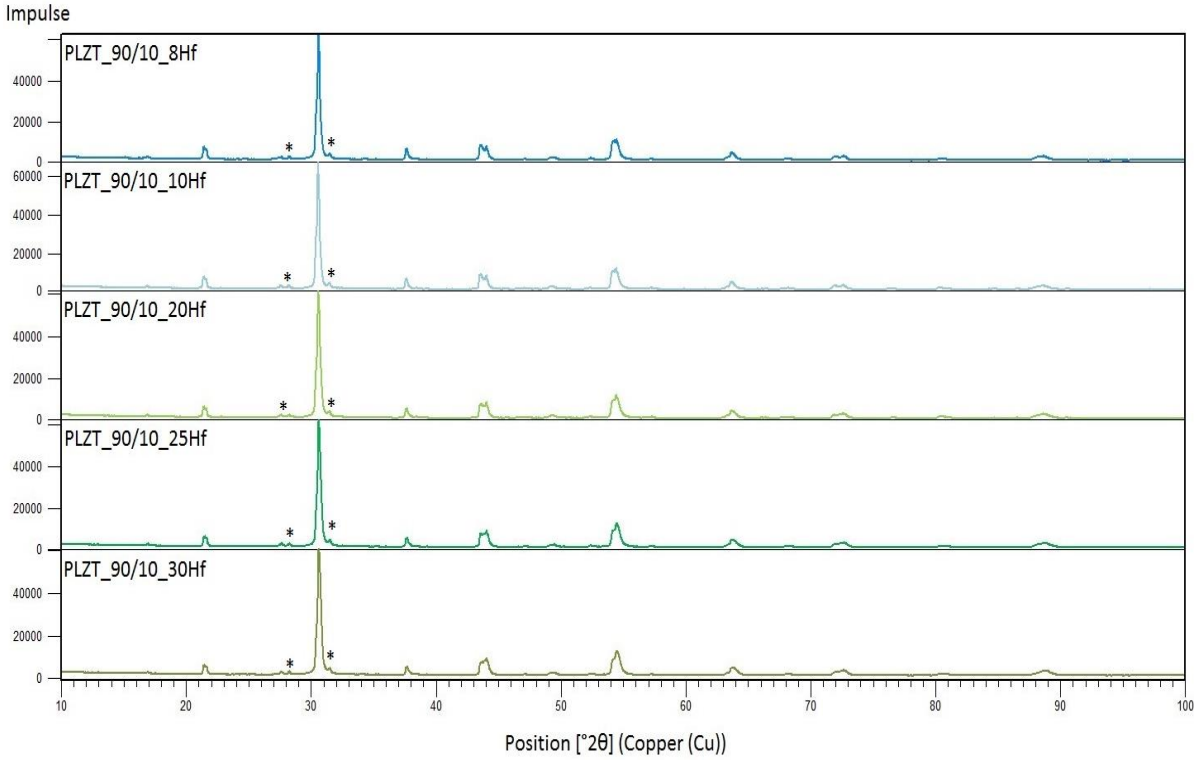

Figure 10 XRD Spectra of calcinated PLZT_90/10_xHf (x: 8->30Hf) *= secondary phases ($PbHfO_3$ and ZrO_2)

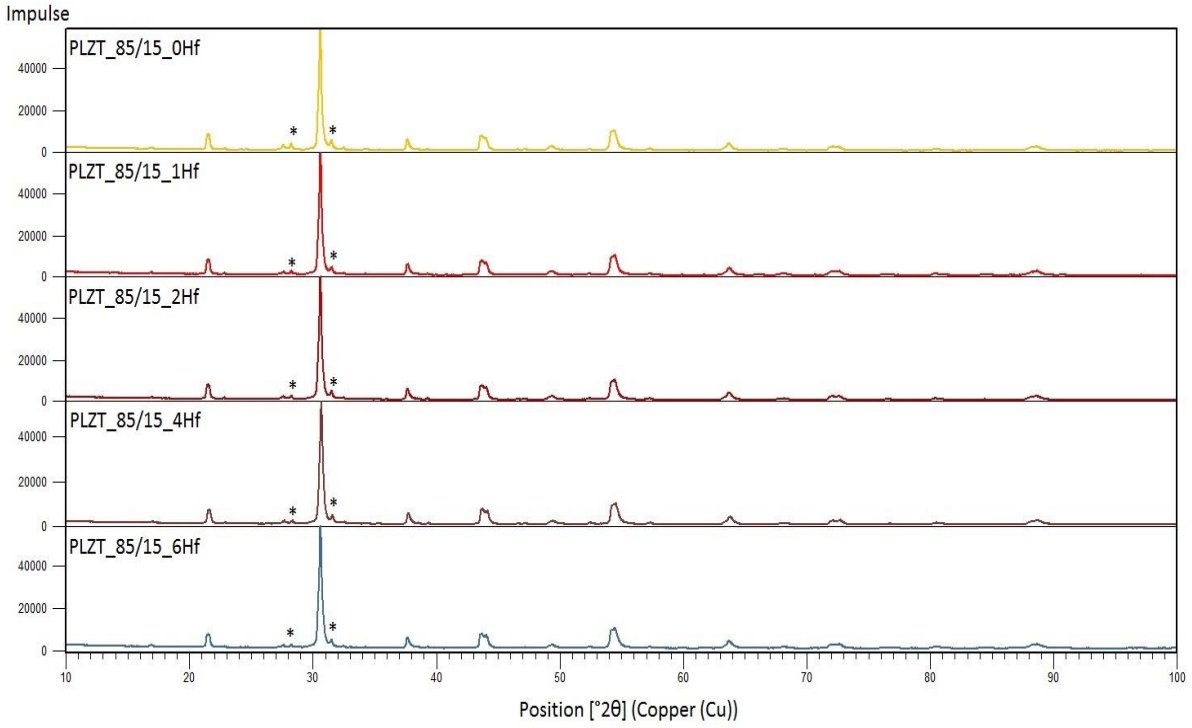

Figure 11 XRD Spectra of calcinated PLZT_85/15_xHf (x: 0->6Hf) *=peak secondary phases ($PbHfO_3$ and ZrO_2)

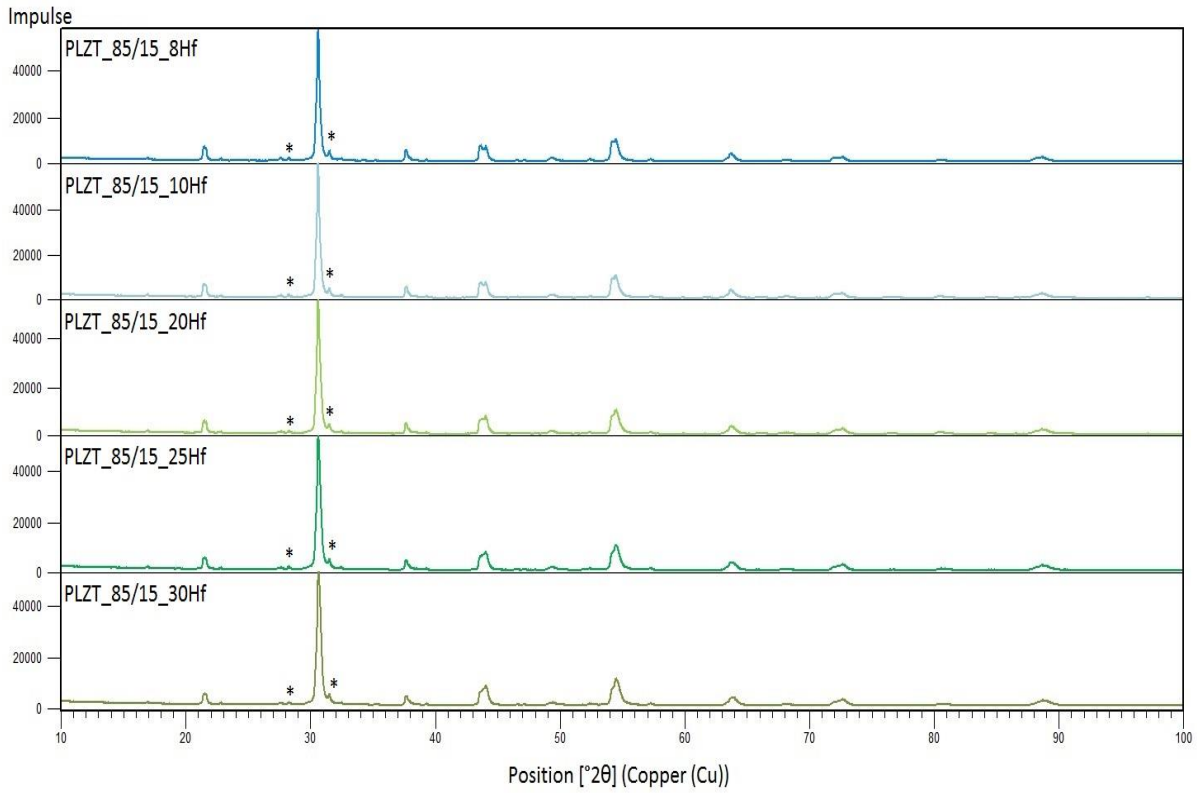

Figure 12 XRD Spectra of calcinated PLZT_85/15_xHf (x: 8->30Hf) *=peak secondary phases ($PbHfO_3$ and ZrO_2)

Figure 13 and Figure 14show the XRD spectra for the sintered samples of PLZT_90/10_xHf. The main PLZT peak at 30 °2θ is clearly shown and no secondary phases could be detected. The same can be said for the PLZT_85/15_xHf samples shown in Figure 15 and Figure 16.

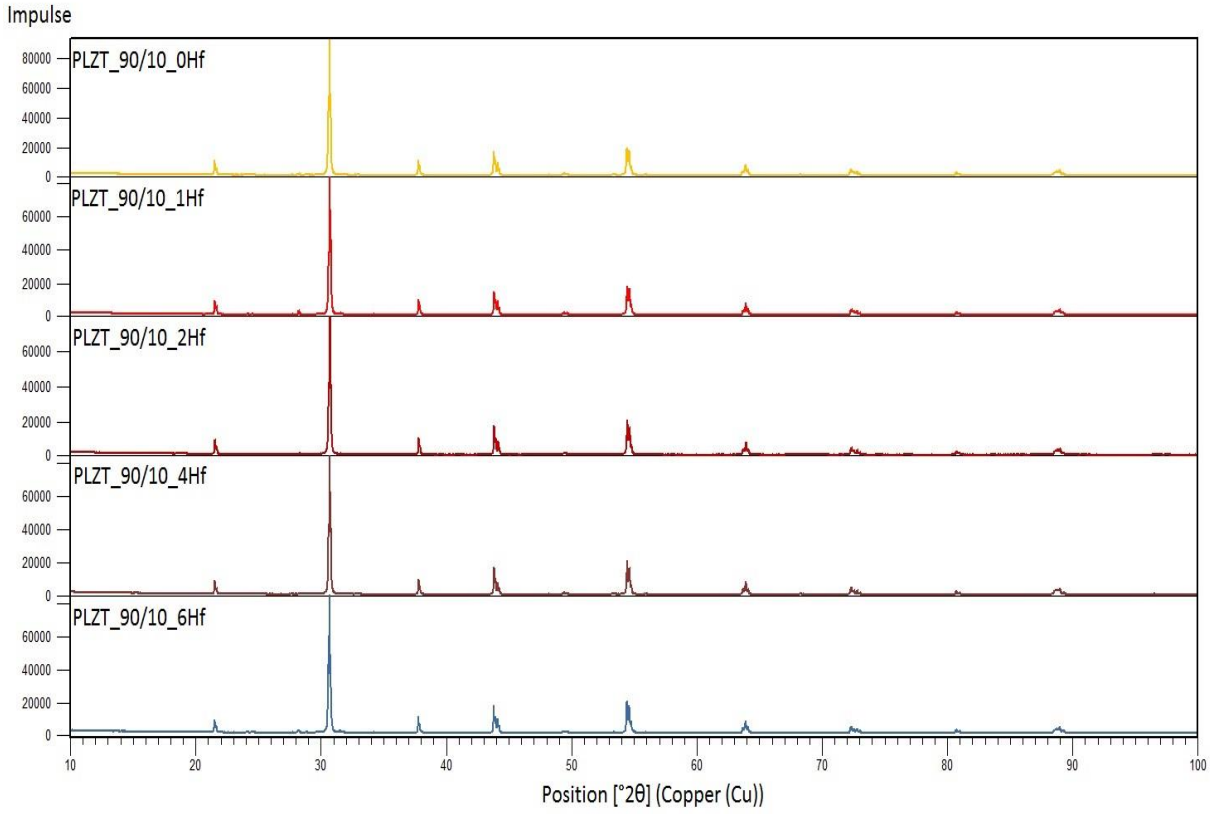

Figure 13 XRD Spectra of sintered PLZT_90/10_xHf (x: 0->6Hf)

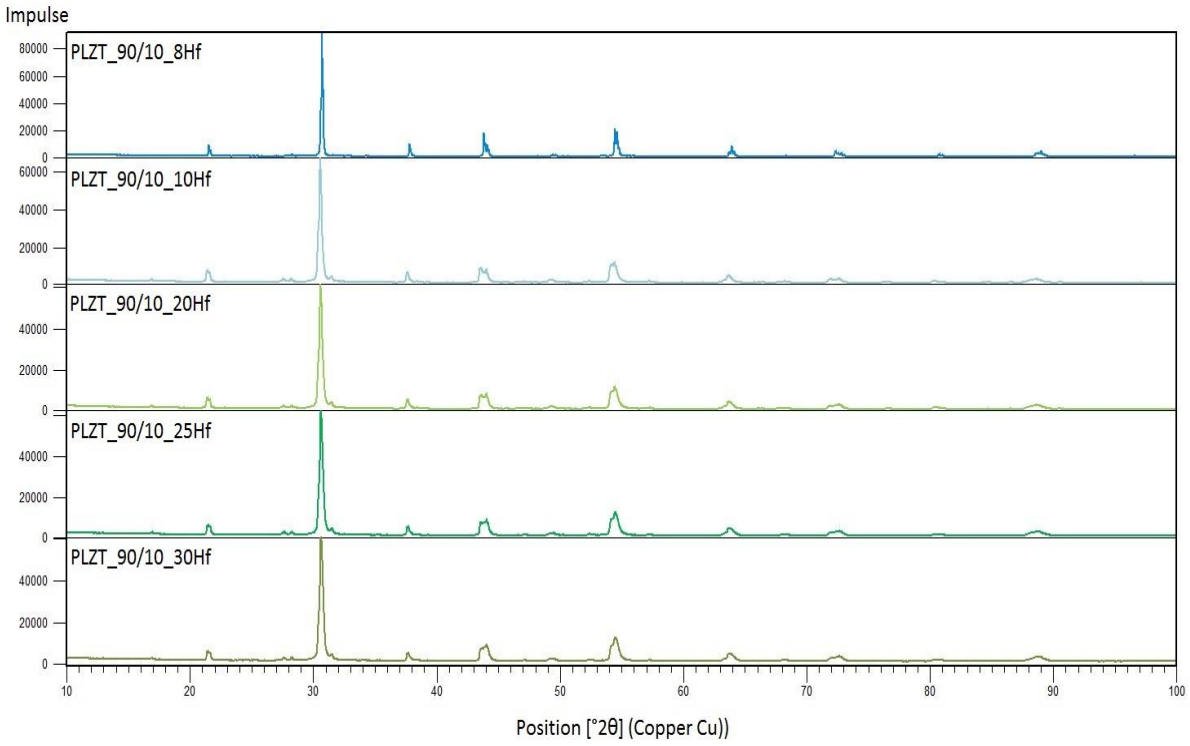

Figure 14 XRD Spectra of sintered PLZT_90/10_xHf (x: 8->30Hf)

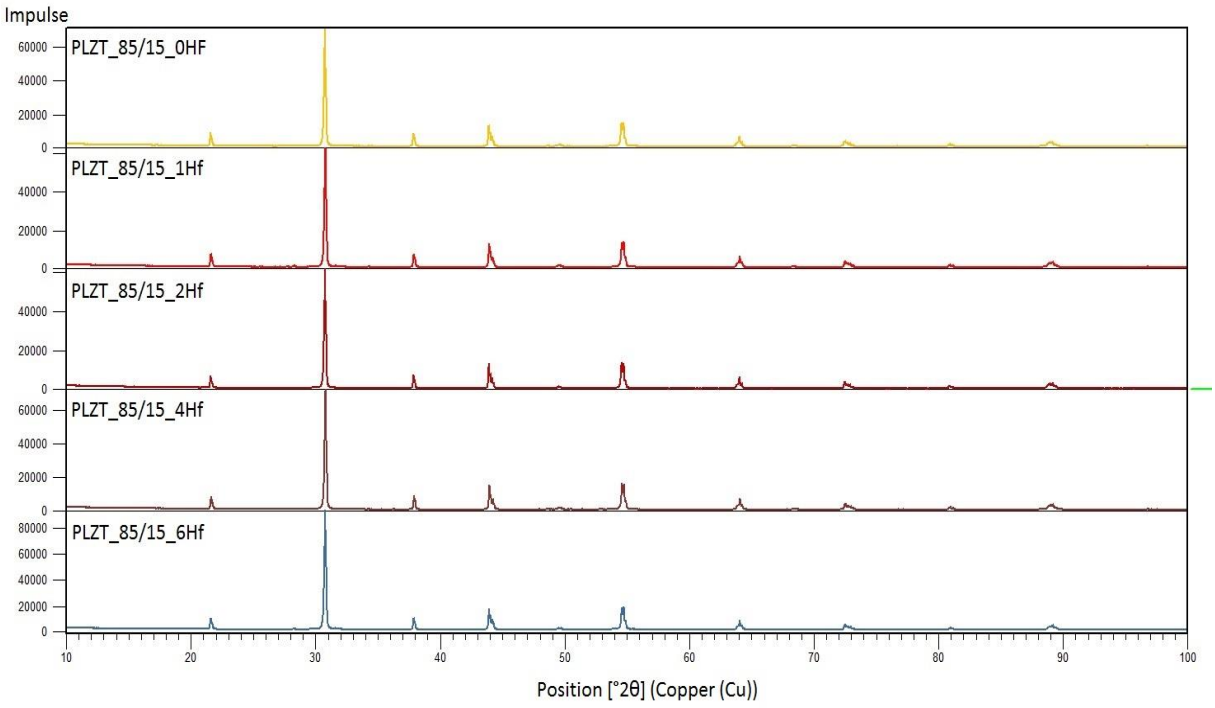

Figure 15 XRD Spectra of sintered PLZT_85/15_xHf (x: 0->6Hf)

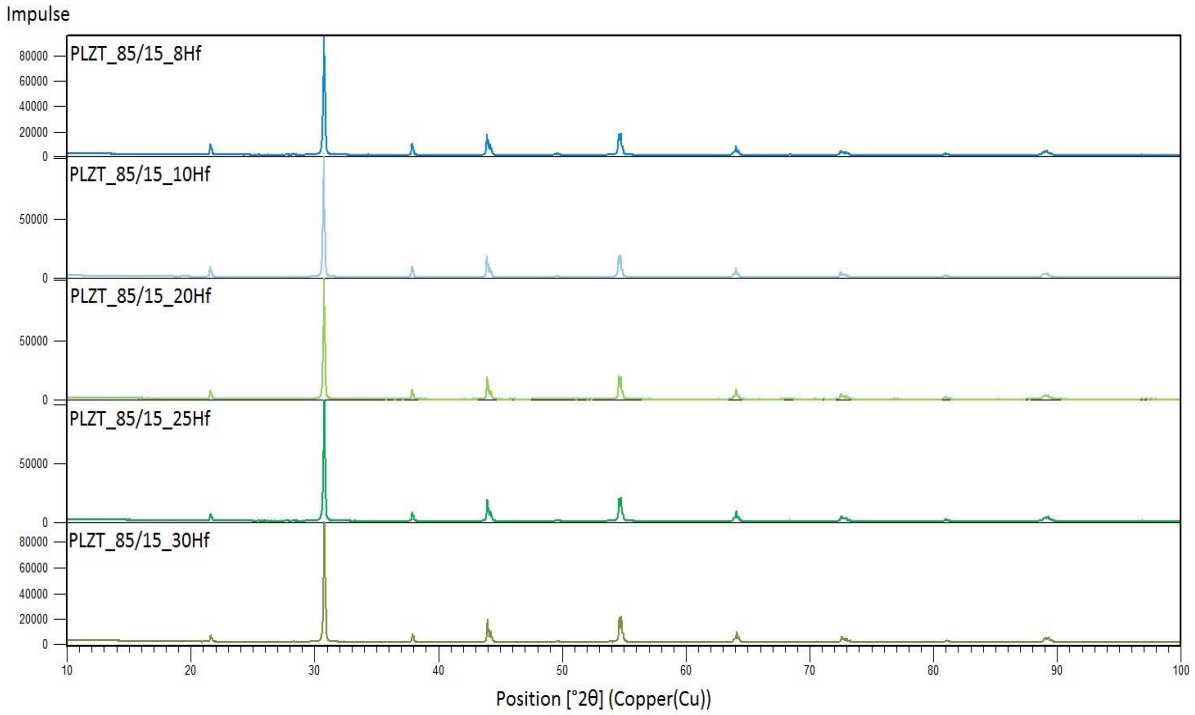

Figure 16 XRD Spectra of sintered PLZT_85/15_xHf (x: 8->30Hf)

Regarding the data obtained by the Rietveld method lattice parameters, cell volume and theoretical density were determined and compared.

For PLZT_90/10_xHf the determined lattice parameters, cell volume, theoretical densityand tolerance factor are shown in Table 11 and Table 12. The data of PLZT_85/15_xHf is depicted in Table 13 and

Table 14.

Table 11 XRD data of PLZT_90/10_xHf calcinated

Sample	Volume [A³]	M [g/mol]	Density [g/cm³]	c/a ratio	Tolerancefactor	c-a difference
PLZT_90/10_0Hf	424,72	331,77	7,78	2,4669	0,9520	8,5615
PLZT_90/10_1Hf	423,71	332,56	7,82	2,4681	0,9520	8,5603
PLZT_90/10_2Hf	423,68	333,44	7,84	2,4690	0,9524	8,5641
PLZT_90/10_4Hf	422,68	334,91	7,89	2,4702	0,9526	8,5628
PLZT_90/10_6Hf	422,85	336,49	7,93	2,4709	0,9528	8,5675
PLZT_90/10_8Hf	422,50	338,06	7,97	2,4705	0,9528	8,5632
PLZT_90/10_10Hf	423,63	339,63	7,99	2,4699	0,9520	8,5679
PLZT_90/10_20Hf	422,02	347,48	8,20	2,4684	0,9524	8,5504

PLZT_90/10_25Hf	421,65	351,41	8,30	2,4706	0,9526	8,5581
PLZT_90/10_30Hf	421,35	355,33	8,40	2,4668	0,9528	8,5382

Table 12 XRD data PLZT_90/10_xHf sintered

Sample	Volume [A³]	M [g/mol]	Density [g/cm³]	c/a ratio	Tolerance factor	c-a difference
PLZT_90/10_0Hf	421,37	331,77	7,84	2,4557	0,9520	8,4866
PLZT_90/10_1Hf	420,47	332,56	7,88	2,4563	0,9520	8,4830
PLZT_90/10_2Hf	421,39	333,44	7,88	2,4558	0,9524	8,4869
PLZT_90/10_4Hf	421,41	334,91	7,92	2,4559	0,9526	8,4875
PLZT_90/10_6Hf	420,47	336,49	7,97	2,4561	0,9528	8,4821
PLZT_90/10_8Hf	420,45	338,06	8,01	2,4559	0,9528	8,4814
PLZT_90/10_10Hf	421,41	339,63	8,03	2,4625	0,9520	8,5186
PLZT_90/10_20Hf	420,57	347,48	8,23	2,4618	0,9524	8,5096
PLZT_90/10_25Hf	420,51	351,41	8,33	2,4614	0,9526	8,5072
PLZT_90/10_30Hf	420,37	355,33	8,42	2,4613	0,9528	8,5056

Table 13 XRD data PLZT_85/15_xHf calcinated

Sample	Volume [A³]	M [g/mol]	Density [g/cm³]	c/a ratio	Tolerance factor	c-a difference
PLZT_85/15_0Hf	423,60	329,60	7,75	2,4700	0,9520	8,5685
PLZT_85/15_1Hf	423,07	330,35	7,78	2,4705	0,9520	8,5683
PLZT_85/15_2Hf	423,02	331,09	7,80	2,4704	0,9524	8,5662
PLZT_85/15_4Hf	422,60	332,57	7,84	2,4722	0,9526	8,5720
PLZT_85/15_6Hf	421,83	334,06	7,89	2,4732	0,9528	8,5713
PLZT_85/15_8Hf	421,68	335,54	7,93	2,4713	0,9528	8,5615
PLZT_85/15_10Hf	421,67	337,02	7,96	2,4712	0,9520	8,5608
PLZT_85/15_20Hf	420,05	344,44	8,17	2,4786	0,9524	8,5843
PLZT_85/15_25Hf	420,71	348,15	8,25	2,4731	0,9526	8,5632
PLZT_85/15_30Hf	419,55	351,86	8,36	2,4791	0,9528	8,5833

Table 14 XRD data PLZT_85/15_xHf sintered

Sample	Volume [A³]	M [g/mol]	Density [g/cm³]	c/a ratio	Tolerance factor	c-a difference
PLZT_85/15_0Hf	419,25	329,60	7,83	2,4583	0,9520	8,4842
PLZT_85/15_1Hf	416,77	330,35	7,90	2,4540	0,9520	8,4477
PLZT_85/15_2Hf	419,24	331,09	7,87	2,4557	0,9524	8,4723
PLZT_85/15_4Hf	416,65	332,57	7,95	2,4536	0,9526	8,4451
PLZT_85/15_6Hf	416,05	334,06	8,00	2,4533	0,9528	8,4396
PLZT_85/15_8Hf	415,92	335,54	8,04	2,4529	0,9528	8,4368
PLZT_85/15_10Hf	418,22	337,02	8,03	2,4562	0,9520	8,4675
PLZT_85/15_20Hf	418,03	344,44	8,21	2,4554	0,9524	8,4623
PLZT_85/15_25Hf	417,67	348,15	8,31	2,4566	0,9526	8,4655
PLZT_85/15_30Hf	417,30	351,86	8,40	2,4555	0,9528	8,4580

4.1.4. Small signalmeasurements

The obtained data for capacity, loss factor and relative permittivity are in Table 15 for PLZT_90/10_xHf and in Table 16 for 85/15_xHf.

Table 15 Capacity, loss factor and permittivity of PLZT_90/10_xHf (unpoled)

Sample	Capacity 1kHz	tan δ 1kHz	ε 1kHz	Capacity 100kHz	tan δ 100kHz	ε 100kHz
PLZT_90/10_0Hf	0,50	0,011	607	0,49	0,017	583
PLZT_90/10_1Hf	0,47	0,011	587	0,46	0,020	568
PLZT_90/10_2Hf	0,48	0,009	597	0,46	0,030	580
PLZT_90/10_4Hf	0,50	0,007	618	0,48	0,012	602
PLZT_90/10_6Hf	0,48	0,009	594	0,46	0,016	571
PLZT_90/10_8Hf	0,39	0,011	495	0,42	0,016	531
PLZT_90/10_10Hf	0,51	0,007	632	0,47	0,012	588
PLZT_90/10_20Hf	0,51	0,007	618	0,49	0,011	602
PLZT_90/10_25Hf	0,49	0,005	594	0,48	0,009	581
PLZT_90/10_30Hf	0,54	0,006	630	0,53	0,010	616

Table 16 Capacity, loss factor and permittivity of PLZT_85/15_xHf (unpoled)

Sample	Capacity 1kHz	tan (d) 1kHz	Epsilon 1kHz	Capacity 100kHz	tan (d) 100kHz	Epsilon 100kHz
PLZT_85/15_0Hf	0,77	0,027	760	0,75	0,045	900
PLZT_85/15_1Hf	0,74	0,029	927	0,68	0,044	855
PLZT_85/15_2Hf	0,89	0,020	1122	0,84	0,069	1051
PLZT_85/15_4Hf	0,93	0,019	1150	0,87	0,028	1080
PLZT_85/15_6Hf	0,67	0,020	843	0,65	0,028	817
PLZT_85/15_8Hf	0,74	0,022	933	0,69	0,033	862
PLZT_85/15_10Hf	0,84	0,015	1023	0,82	0,024	1004
PLZT_85/15_20Hf	0,91	0,014	1114	0,87	0,023	1056
PLZT_85/15_25Hf	0,93	0,016	1175	0,88	0,025	1110
PLZT_85/15_30Hf	0,87	0,013	1085	0,83	0,023	1032

4.1.5. High signalmeasurements

4.1.5.1. Polarization

Shown in Figure 17 are the polarization curves of PLZT_90/10_xHf determined at 8 kV/mm. This was the maximum field were all samples could be measured without breakdown.

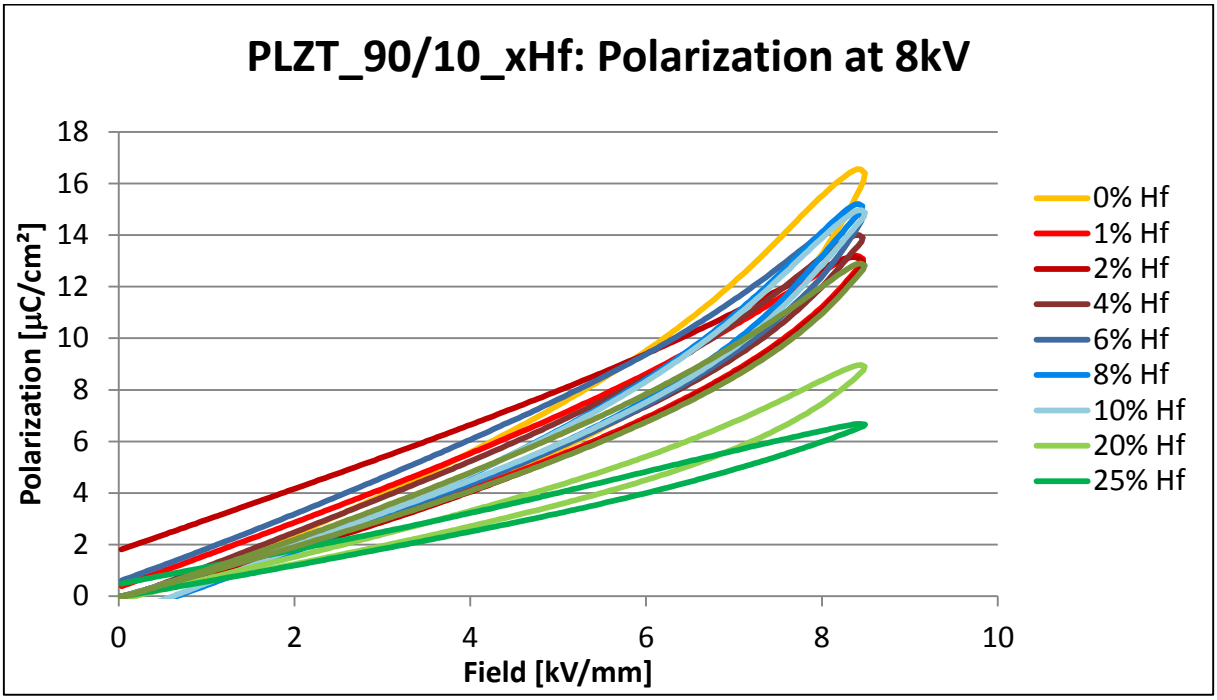

Figure 17 Polarization curves PLZT_90/10_xHf at 8kV/mm

Depicted in Figure 18are the polarization curves of PLZT_90/10_xHf samples which reached saturation polarization, indicated by the horizontal leveling of the curve. In Table 17 the values for forward switching field ($E_{(A->F)}$), backward switching field ($E_{(F->A)}$), the difference between the two (ΔE) and saturation polarization for these samples are given.

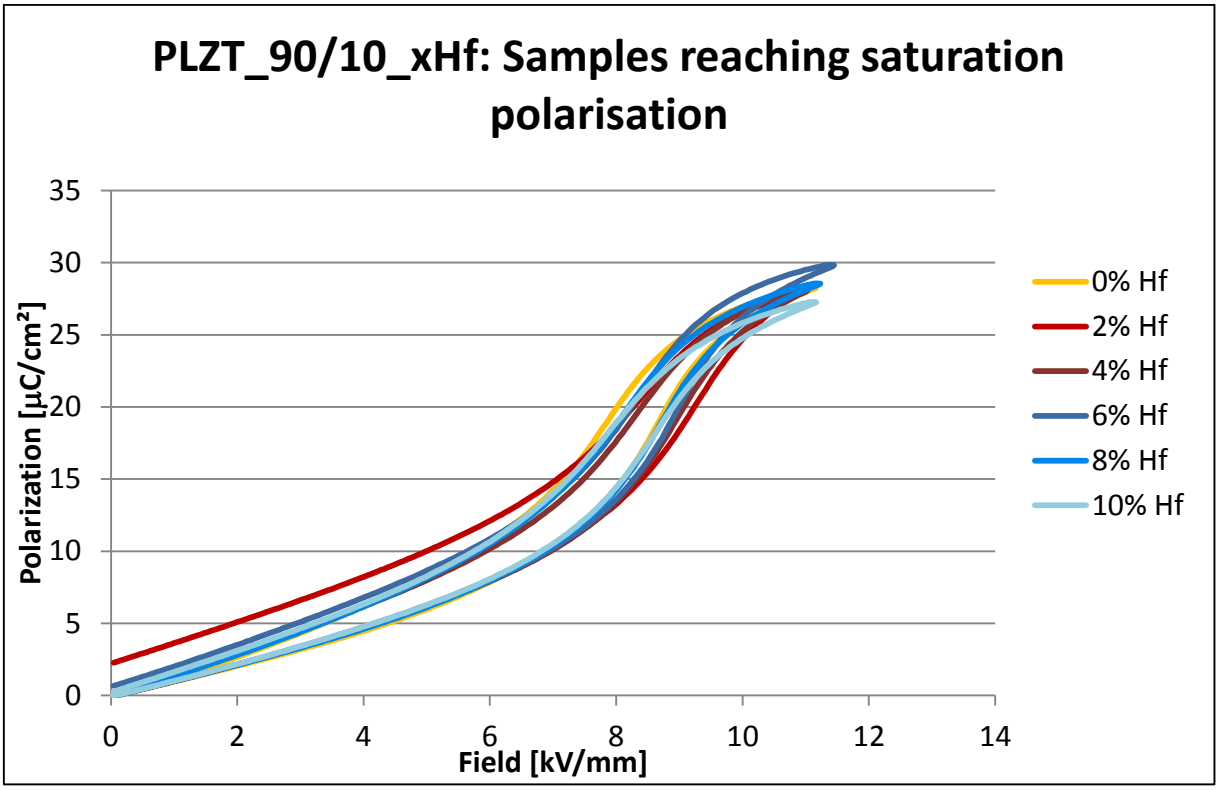

Figure 18 Saturated polarization curves PLZT_90/10_xHf at 10kV/mm

Table 17 Data of saturated polarization curves PLZT_90/10_xHf at 10kV/mm

Sample	Forward switching field ($E_{(A->F)}$) [kV/mm]	Backward switching field ($E_{(F->A)}$) [kV/mm]	ΔE	SaturationPolarization [µC/cm²]
0% Hf	8,47	7,64	0,83	27,3
2% Hf	8,8	7,78	1,02	27,2
4% Hf	8,71	8,1	0,61	27,1
6% Hf	8,66	8,05	0,61	28,0
8% Hf	8,5	7,82	0,68	27,0
10% Hf	8,48	7,85	0,63	26,3

With the PLZT_85/15_xHf series all samples reached saturation polarization when submitted to a field of 6kV/mm. The curves are shown inFigure 19 and the data in Table 18.

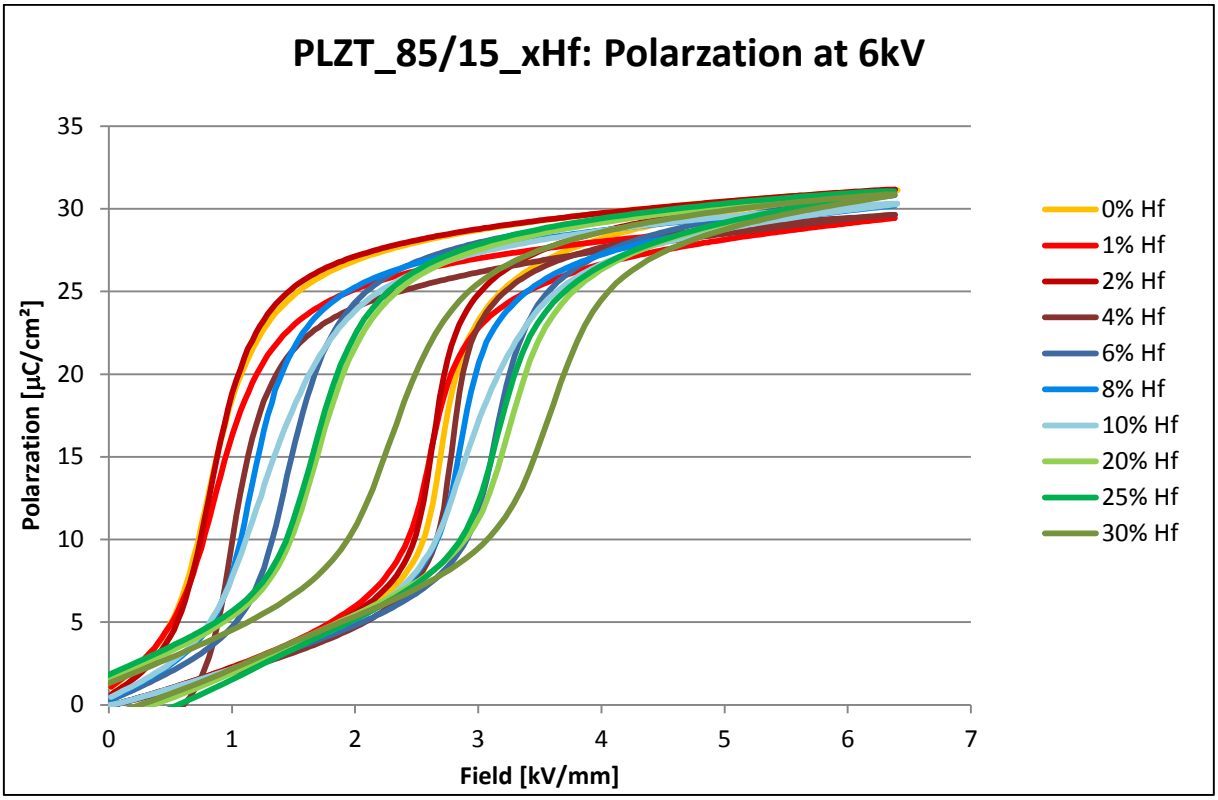

Figure 19 Saturated polarization curves PLZT_85/15_xHf 6kV/mm

Table 18 Data of saturated polarization curves PLZT_85/15_xHf 6kV/mm

Samples	Forward switching field ($E_{(A->F)}$) [kV/mm]	Backward switching field ($E_{(F->A)}$) [kV/mm]	ΔE	SaturationPolarization [µC/cm²]
0% Hf	2,76	0,946	1,81	31
1% Hf	2,62	1	1,62	29,3
2% Hf	2,66	0,941	1,72	31
4% Hf	2,81	1,2	1,61	29,6
6% Hf	3,16	1,55	1,61	30,7
8% Hf	2,91	1,29	1,62	30,2
10% Hf	2,98	1,42	1,56	30,3
20% Hf	3,21	1,84	1,37	29,5
25% Hf	3,16	1,75	1,41	31,5
30% Hf	3,56	2,41	1,15	29,7

4.1.6. Electronmicroscopy

Depicted inFigure 20 is an example of an image (PLZT_85/15_20Hf). All other images can be found in Annex 2.

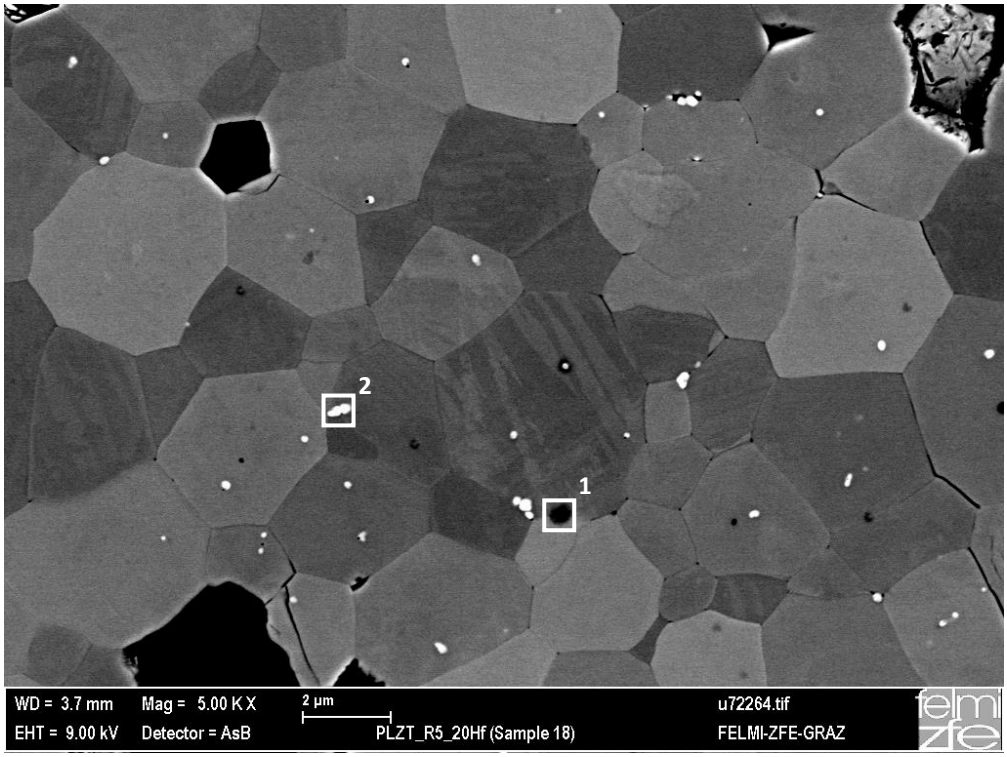

Figure 20 BSE image of PLZT_85/15_6Hf (with indicated secondary phases: 1=ZrO_2 and 2=HfO_2)

The area indicated with 1 is a secondary phase consisting of zirconium oxide. Hafnium oxide is responsible for the small white grains seen above (area 2). The average grain size calculated is depicted in Table 19 for the PLZT_90/10_xHf series and in Table 20 for the PLZT_85/15_xHf series.

Table 19 Calculated grain sizes for PLZT_90/10_xHf series

Sample	Grainsize [µm]		Differencebetweenmethodes [%]
	Interceptmethode	Line cutmethode	
PLZT_90/10_0Hf	3,29	3,12	5,14
PLZT_90/10_2Hf	3,74	3,59	4,09
PLZT_90/10_6Hf	3,39	3,10	9,24
PLZT_90/10_10Hf	3,36	3,23	4,02
PLZT_90/10_20Hf	2,89	2,69	7,68
PLZT_90/10_25Hf	2,52	2,09	20,19
PLZT_90/10_30Hf	2,88	2,61	10,37

Table 20 Calculated grain sizes for PLZT_85/15_xHf series

Sample	Grain size [µm]		Difference between methodes [%]
	Intercept methode	Line cut methode	
PLZT_85/15_0Hf	3,25	2,79	16,43
PLZT_85/15_2Hf	2,92	2,75	6,08
PLZT_85/15_6Hf	2,04	2,02	1,09
PLZT_85/15_10Hf	2,53	2,32	9,18
PLZT_85/15_20Hf	2,06	2,02	1,68
PLZT_85/15_25Hf	1,73	1,47	17,14
PLZT_85/15_30Hf	3,17	2,43	30,34

4.2. Discussion

The objective of this thesis is to investigate the influence of substituting zirconium by hafnium in PLZT. In this section the results shown above will be discussed in detail. First the incorporation of hafnium and sintering behavior will be discussed by analyzing the SEM and XRD data as well as density measurements. Then the influence of the doping on the electrical properties will be shown.

4.2.1. Sintering behavior and hafnium incorporation

4.2.1.1. XRD analysis

The XRD spectra show secondary phases within the sample, but only when the concentration exceeds appr. 5 mol%. Secondary phases can be detected for all samples after calcination. Those were identified as zirconium oxide and lead hafnate. These impurities occur because the temperature during calcinations was not high enough or the reaction time was not long enough to allow complete formation of the target compound. While zirconium oxide remained an educt, hafnium oxide and lead oxide seem to have formed an intermediate phase while subjected to calcination, which only afterwards reacted with other compounds to form the product. These secondary phases exist because either the lack of diffusion speed, making it impossible for one component to reach the other components, or because two educts show a higher reactivity.

In the spectra of the sintered samples no secondary phases could be detected. The secondary phases still present after calcination were incorporated into the lattice while the samples were subjected to the sintering temperature. However secondary phases may still remain below a certain detection limit.

The data obtained using the Rietveld method give an overview over the buildup of the crystal lattice. As shown by the calculated tolerance factor (between 0,952 and 0,953) the substitution of zirconium by hafnium should be possible and result in a perovskite structure. Shown in Figure 21 is the change of the calculated cell volume of the unit cell with increasing hafnium content for the PLZT_90/10_xHf series.

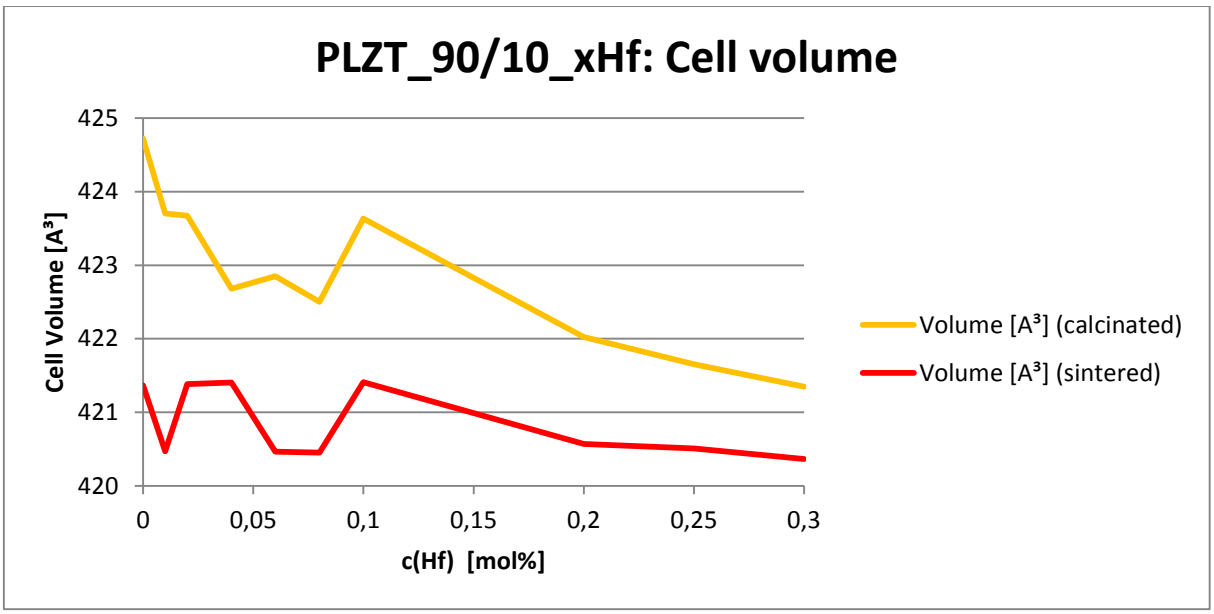

Figure 21 Cell volume (unit cell) of the PLZT_90/10_x Hf series

For concentrations of hafnium of 10 mol% or higher a steady decline in cell volume can be seen. The maximum difference of calculated cell volume is approximately 3 Angstrom for the calcinated samples and only approximately 1 Angstrom for the sintered sample. This translates to an alteration of less than one percent. As the ionic radii responsible for the size of the unit cell are almost identical for zirconium (0,72) and hafnium (0,71), these results are consistent with the expectations. The cell volume of the sintered samples is always lower than that of the calcinated samples. The decreasing cell volume of the calcinated samples is due to the ZrO_2secondary phase present, which leads to a higher titanium content in the crystal lattice and consequently to a smaller cell volume. Concerning the sintered samples, the decrease can be explained by the higher defect concentration present due to the higher process temperature.

In Figure 22 the unit cell volume of the PLZT_85/15_xHf series is shown.

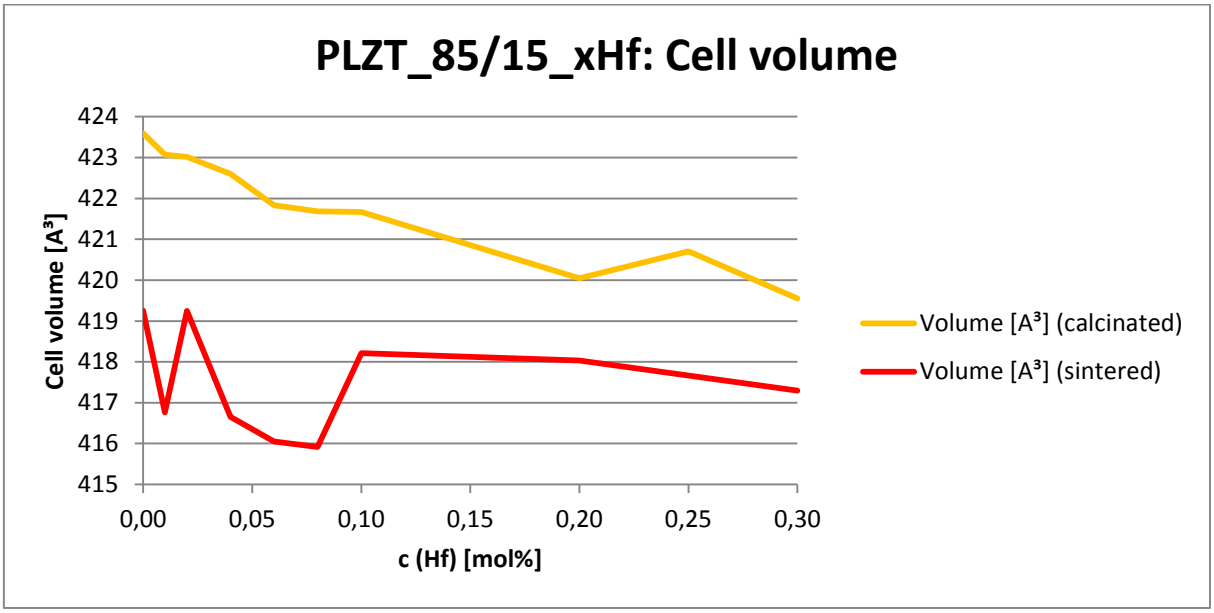

Figure 22 Cell volume (unit cell) of the PLZT_85/15_x Hf series

The calcinated samples show a steady decline in cell volume from 423,6 A to 419,6 A. The sintered samples show diffuse behavior at low hafnium concentrations, but a shallow decline above 10 mol% hafnium. The cell volume goes from 419,3 A to 417,3 A when the hafnium content is increased. Again the change in unit cell volume is less than one percent for both calcinated and sintered samples. The decrease in cell volume is caused by the changes in the lead/zirconium/titanium ratio. This relationship is influenced by the defect density of the material.

Figure 23 and Figure 24depict thetheoretical density of the samples. The density was calculated using the unit cell volume and the molecular mass of the samples and will be related to density values obtained by different methods yielding the relative density.

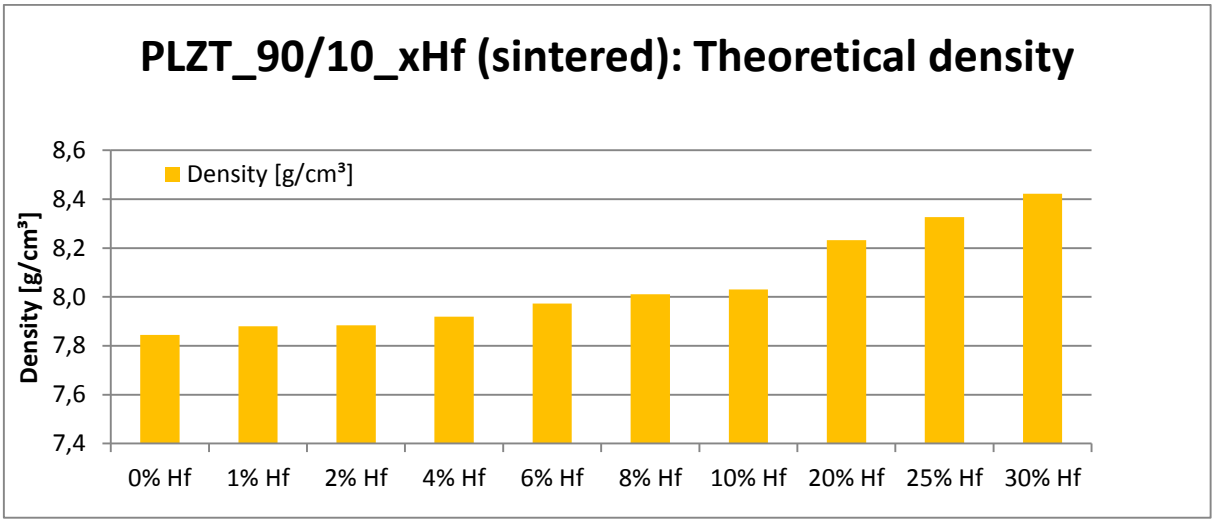

Figure 23 Theoretical density of sintered PLZT_90/10_xHf series

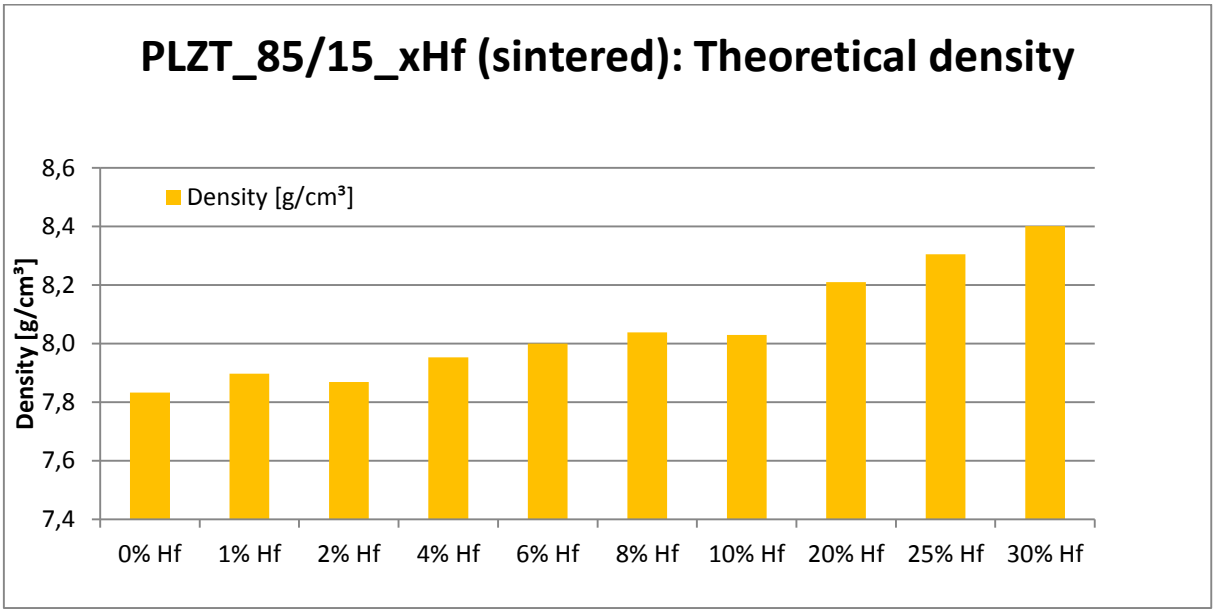

Figure 24 Theoretical density of sintered PLZT_85/15_xHf series

Both series show an increased density with higher hafnium concentration (and subsequently with higher mass). The range of the density values is similar (between 7,8 and 8,4 g/cm³) in both series. The theoretical density is not influenced by the varying titanium content, as the smaller cell volume is compensated by the lower molecular mass of the samples with higher titanium content.

4.2.1.2. Microstructure

The structure of the sintered samples was further analyzed using electron microscopy. The gained data was used to calculate the grain size, to check for secondary phases and to estimate porosity. Figure 25 shows the image obtained from the undoped sample of the PLZT_90/10_xHf series. The miniscule black spots seen in the image are leftover residues of the silica material used for polishing the sample prior to the microscopy.

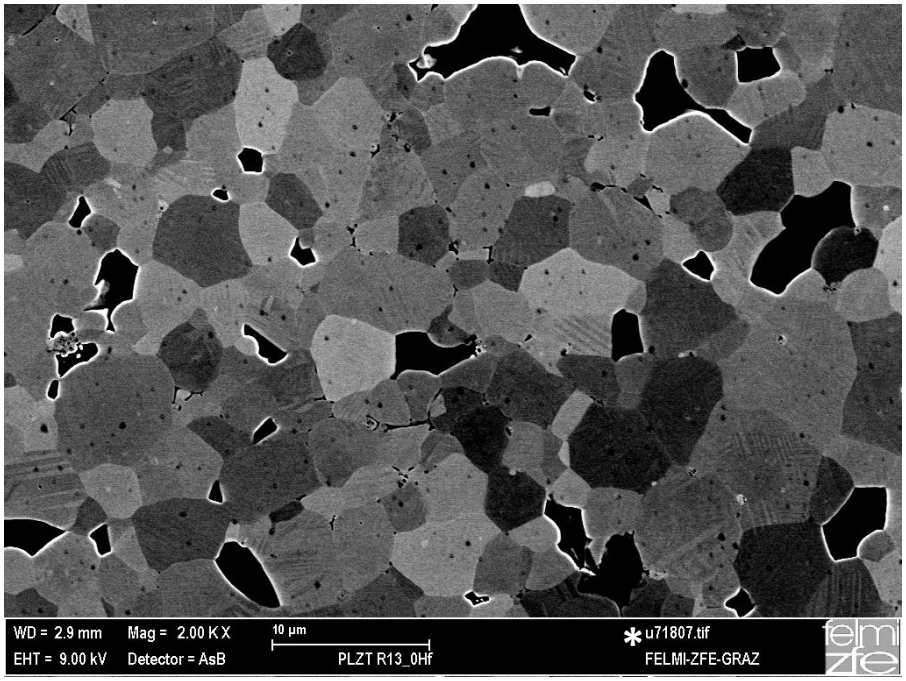

Figure 25 BSE image of PLZT_90/10_0Hf (secondary phase ZrO2 indicated by *)

There are pores visible (black spots with white border). Compared to the grains visible, the pores show a broad variation of size. Some are bigger than the average grains and some are smaller. The black grain (indicated above by the *) is a secondary phase consisting of zirconium oxide (determined by EDX). There are not many such secondary phases present in the sample, therefore it is not surprising that this phase could not be detected in the XRD measurements.

Depicted in Figure 26 is the PLZT_90/10_30Hf sample.

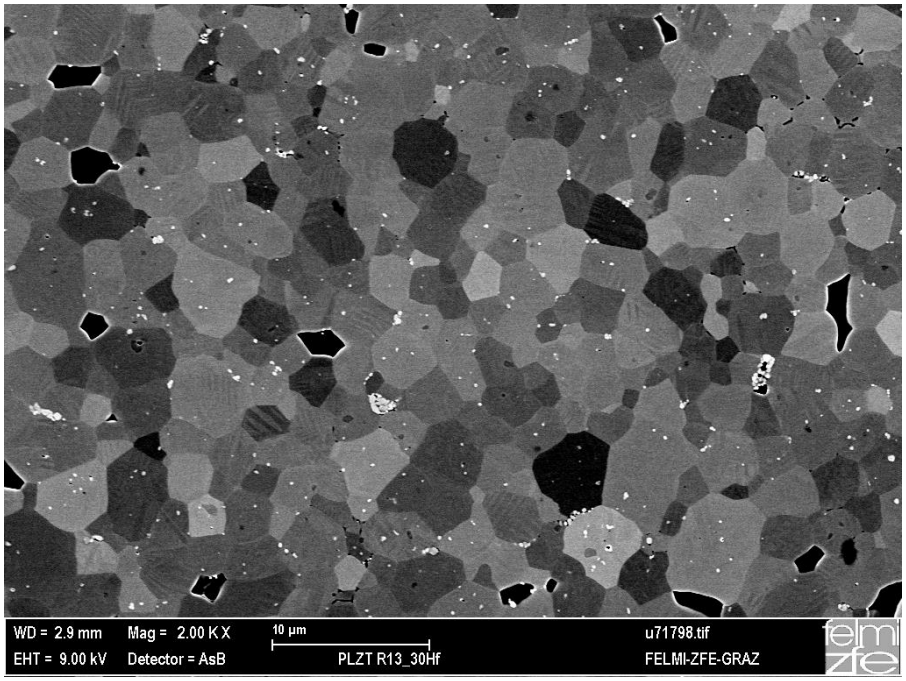

Figure 26 BSE image of PLZT_90/10_30Hf

There are pores visible in this image as well. However they are fewer and smaller than in the undoped sample. They seem to be about the same size as the average grains. The grains in this sample are more evenly distributed regarding their size than the grains in the undoped sample. The black zirconium oxide secondary phases are present here too, but there is another secondary phase as well.

The white dots seen in Figure 26 are composed of lead hafnate. They do not form bigger grains as expected, but exist as small particles randomly distributed through the grain. Some agglomerations seem to form around pores, but they too do not form bigger grains. It appears that the small grains are formed when a saturation of lead hafnate is reached in a specific area of the material. Subsequently the grains are trapped inside the material because of their inability to reach unsaturated areas because of their slow diffusion speed.

In Figure 27 PLZT_85/15_0Hf is depicted.

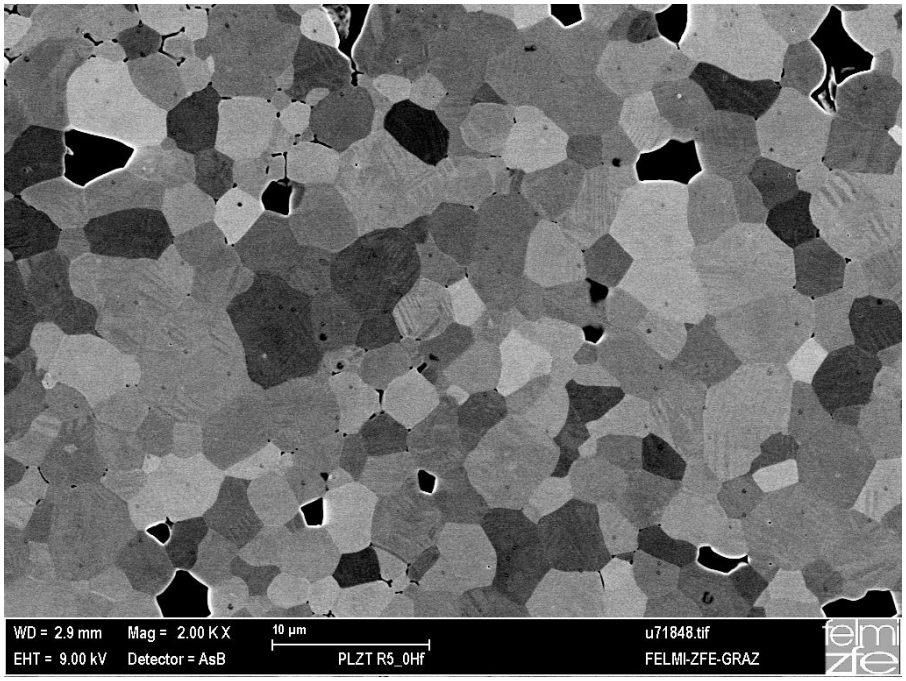

Figure 27 BSE image of PLZT_85/15_0Hf

Compared with the undoped sample of the other series, one can see that there are fewer pores visible and they are smaller. A more even size distribution is also clearly notable in comparison with PLZT_90/10_0Hf. The zirconium oxide secondary phase is present, but the grains are smaller and fewer than in the PLZT_90/10_0Hf sample

Figure 28 depicts the PLZT_85/15_30Hf sample.

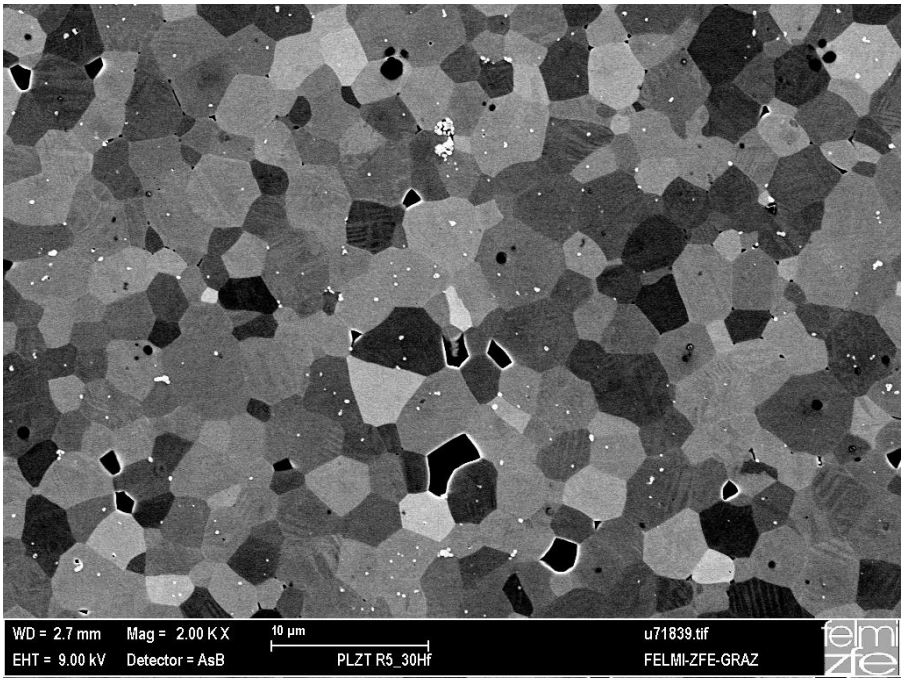

Figure 28 BSE image of PLZT_85/15_30Hf

The hafnium incorporation is incomplete and both zirconium oxide and lead hafnate secondary phases are present. There is however less lead hafnate present than in the PLZT_90/10_30Hf sample. All samples with 2% hafnium doping or more have lead hafnate secondary phases, which become more with increasing hafnium content.

The average grain size was determined using both line cut and intercept method. Shown in Figure 29 is the average grain size of the PLZT_90/10_xHf series.

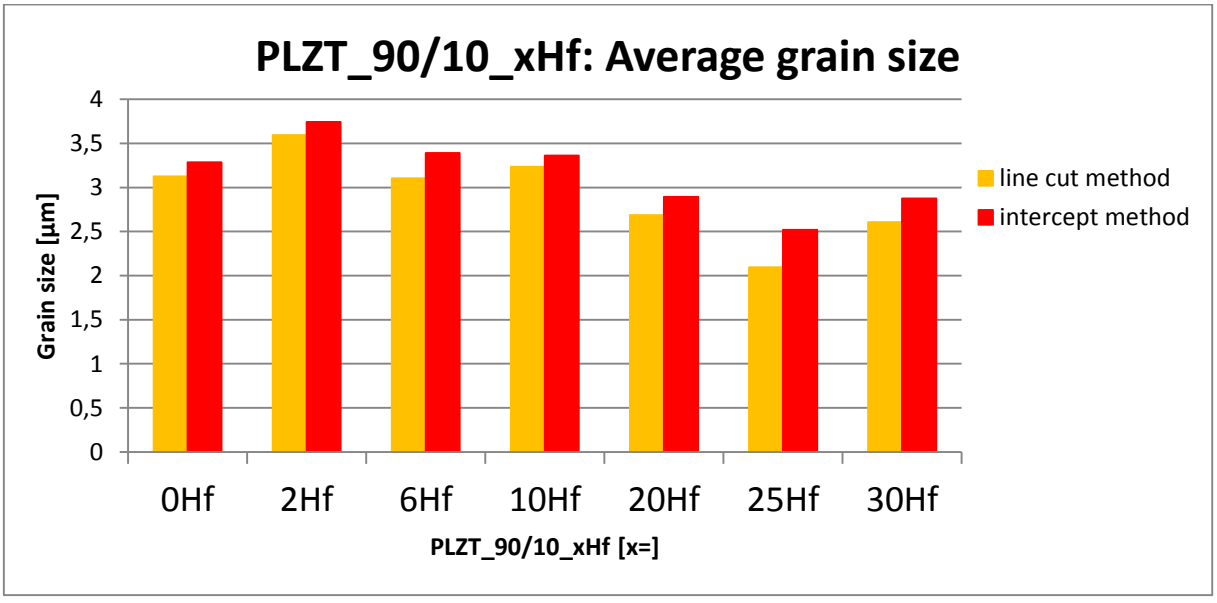

Figure 29 Average grain size of the PLZT_90/10_xHf series

The grain size first increase between 0 and 2 mol% hafnium and decreases until 25 mol% only to increase when 30 mol% hafnium is included. The average grain size obtained by line cut method is always a bit lower than the one from the intercept method, but follows the same trend. Due to the existence of secondary phases in samples with high hafnium content it is difficult to discern the influence of doping on the grain size. The shrinkage of the grains with higher hafnium concentration could be directly linked to the present of the dopant, or to the decrease of lead in the material, as it forms the secondary phase with hafnium. The presence of zirconium oxide as secondary phase means that there is a higher titanium concentration in the main phase, influencing the material as well.

In Figure 30 the average grain size for the PLZT_85/15_xHf series is shown.

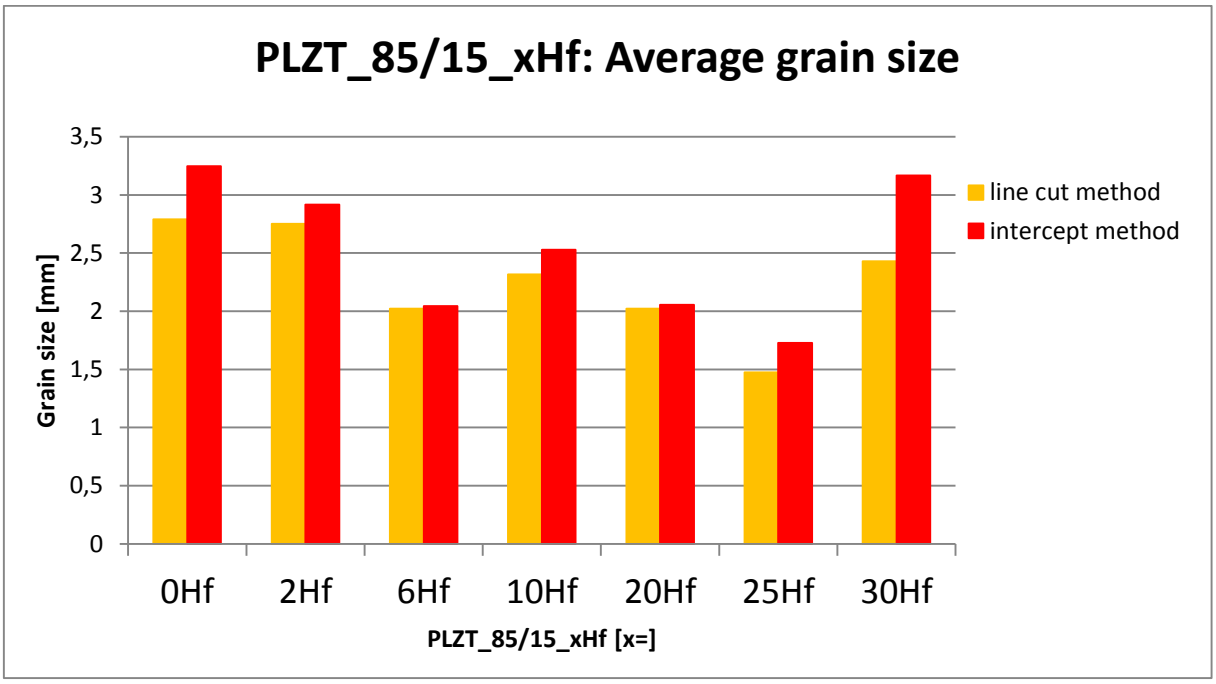

Figure 30 Average grain size of the PLZT_85/15_xHf series

The PLZT_85/15_xHf samples show a decline in grain size up to a hafnium concentration of 30 mol%. The only exception is the 10 mol% hafnium doped sample. The incorporation of hafnium leads to smaller grains.

4.2.2. Density measurements

Density of the samples was determined using the geometrical properties, the Archimedes principle and the XRD data used to calculate the theoretical density of the samples. In Figure 31 the density measurements for PLZT_90/10_xHf series is are shown.

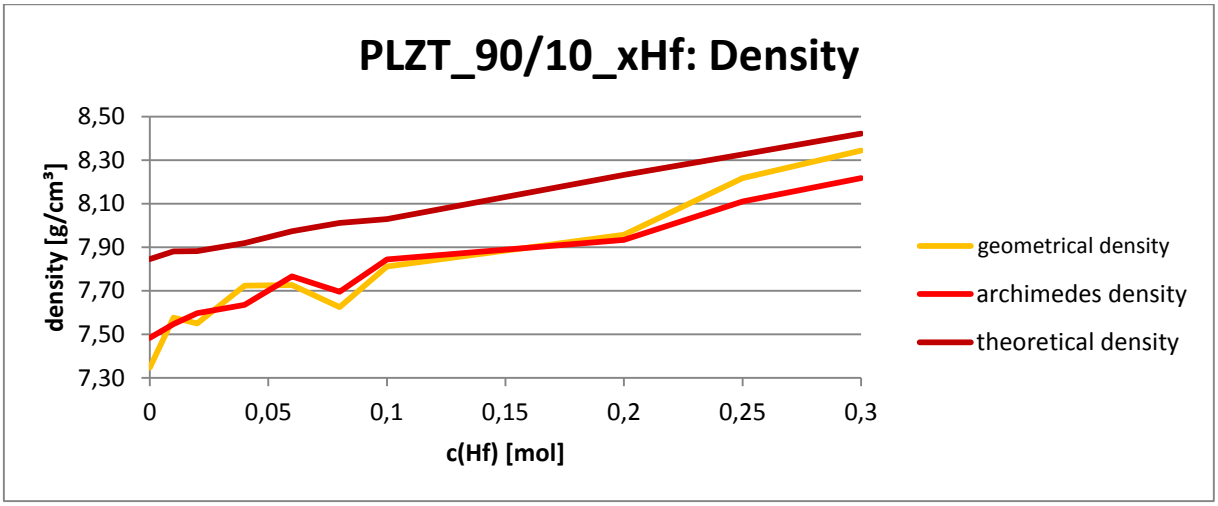

Figure 31 Density measurements of PLZT_90/10_xHf series

All three calculated density values show a parallel increase with increasing hafnium content. The Archimedes and geometrical density curves are approximately at the same values. In Figure 32 the relative density of the PLZT_90/10_xHf series is shown (relation between theoretical and Archimedes density). The values are all above 95%, which indicates sufficient densification for further characterization.

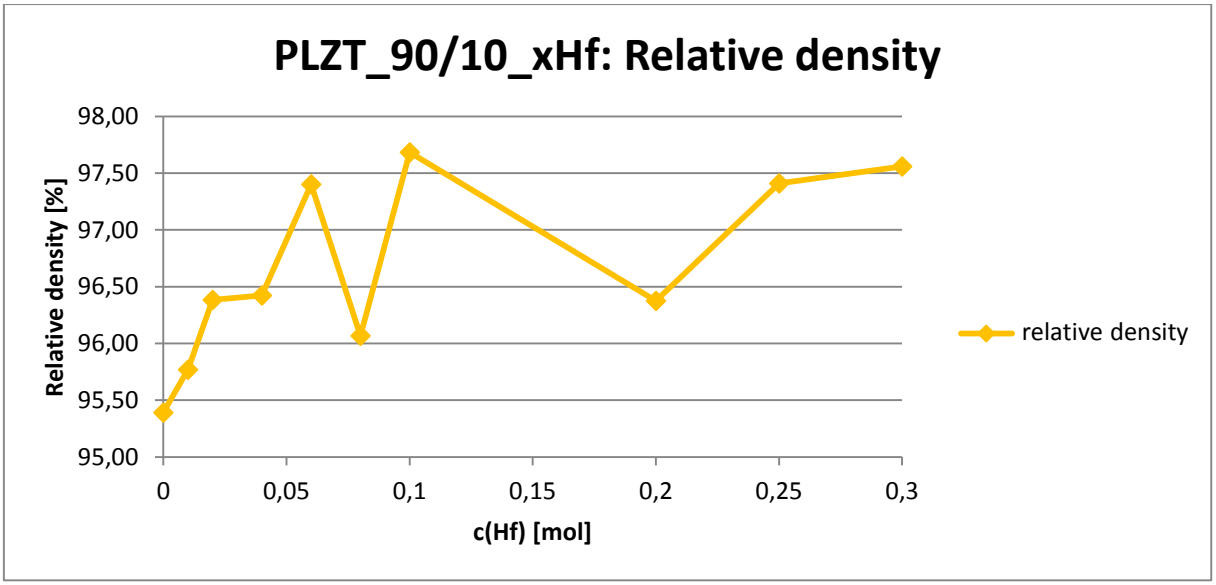

Figure 32 Relative density of PLZT_90/10_xHf series

In Figure 33 the three density values of the PLZT_85/15_xHf series are compared. In accordance with the former series, the density shows a steady rise with increased hafnium content. In general density measured by Archimedes principle yields more exact results, when compared to density measured by geometrical means.

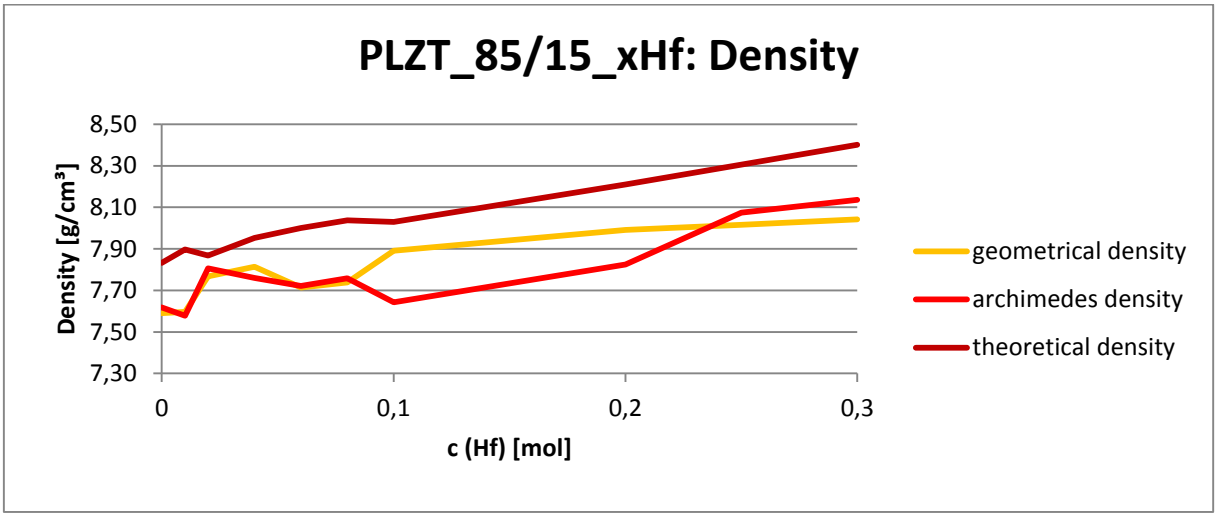

Figure 33 Density measurements of PLZT_85/15_xHf series

Both, the geometrical and the Archimedes density are lower than the theoretical density for each sample. All three density values measuredrange between 7,3 and 8,4 for all samples of both series.

In Figure 34 the relative density of the PLZT_85/15_xHf series is depicted.

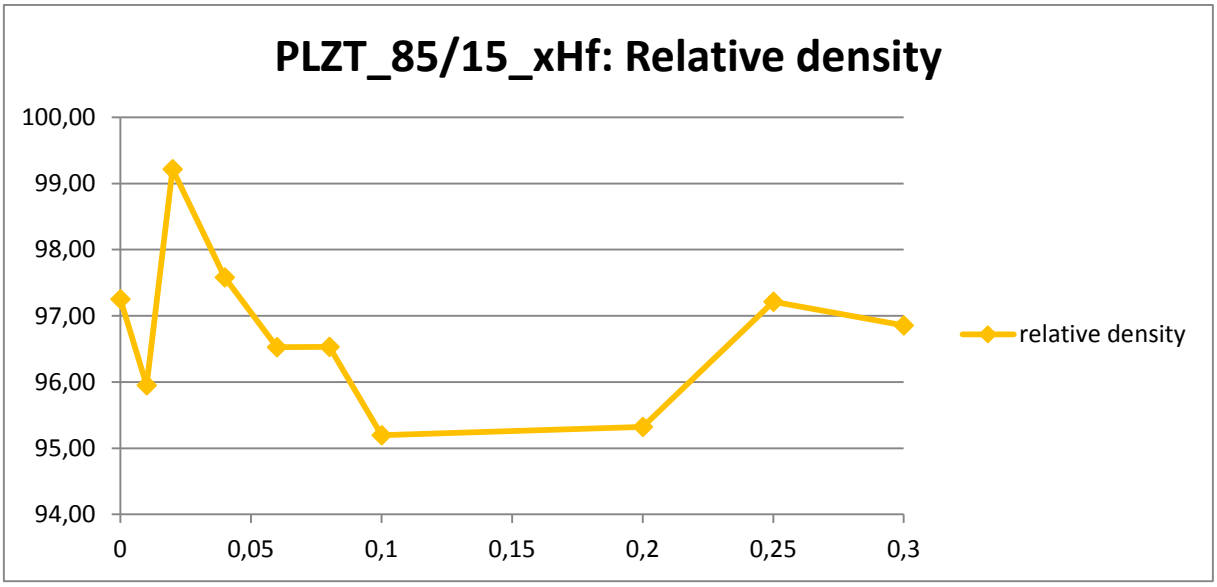

Figure 34 Relative density of PLZT_85/15_xHf series

All samples show between 95 and 99% relative density, which is sufficient for further characterization.

4.2.3. Small signalmeasurements

In this section the results concerning the permittivity and the loss factor of the samples will be discussed. The loss factor indicates how much of the applied energy is lost in the storing process and the permittivity is a measure of permeability of a dielectric concerning an applied electrical field.

4.2.3.1. Permittivity and loss factor

In Figure 35 the permittivity of the PLZT_90/10_xHf series is depicted.

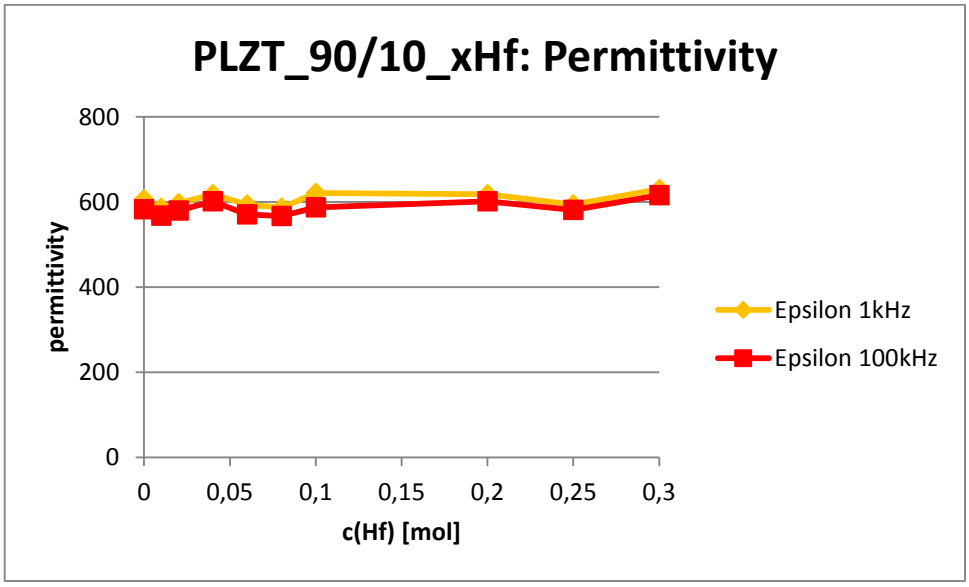

Figure 35 Permittivity of PLZT_90/10_xHf at 1 kHz and 100 kHz measured at room temperature

The values of the measurements at 100 kHz are slightly below those at 1 kHz, but the permittivity of the samples remains reasonably stable over the frequency range.

Hafnium addition has only a small influence the maximum permittivity of PLZT, as all values are around 600. There is a slight increase in capacity with higher hafnium content, but the secondary phases present in these samples (xHf>10%) may distort the result.

Depicted in Figure 36is the loss factor of the PLZT_90/10_xHf series.

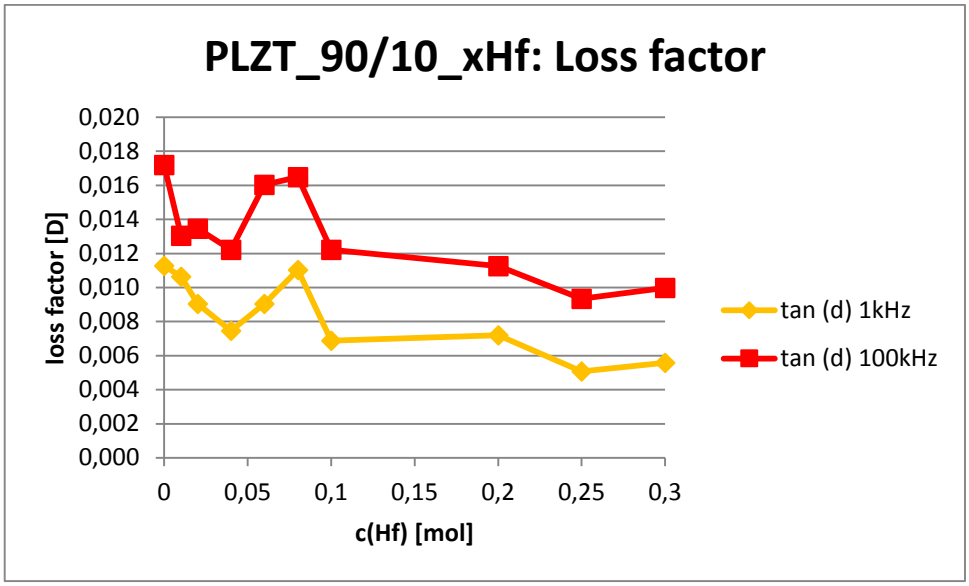

Figure 36 Loss factor of PLZT_90/10_xHf at 1 kHz and 100 kHz measured at room temperature

The loss factor of the samples measured at 100 kHz is higher than those of the ones that were measured at 1 kHz. The sample with 8% hafnium doping shows a maximum at both frequencies. Otherwise the loss factor decreases with increasing hafnium content.

The permittivity of the PLZT_85/15_xHf series (shown in Figure 37) is not influenced by the frequency. Compared with the other series the permittivity of these samples is approximately 40% higher, due to the higher titanium content of the material.

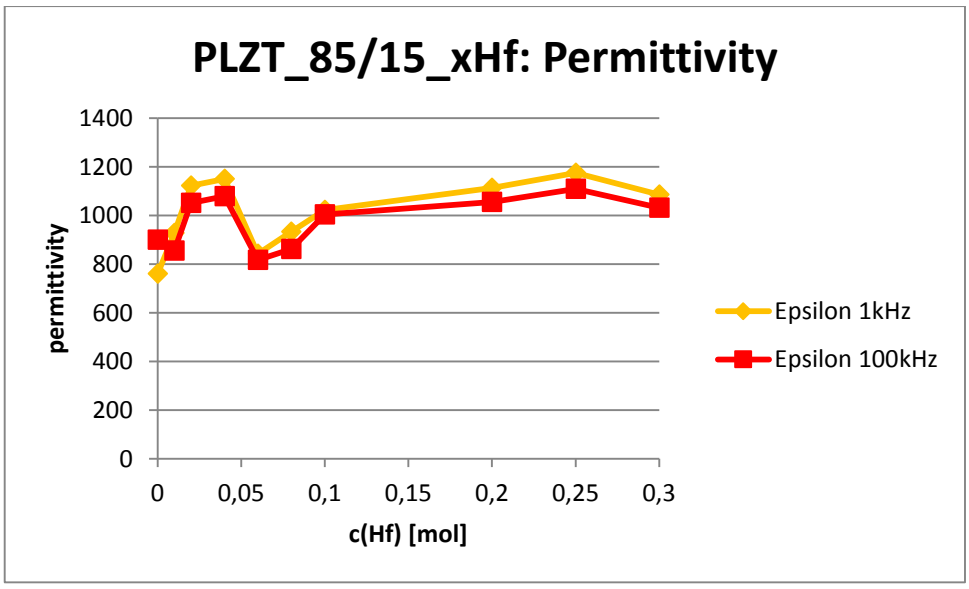

Figure 37 Permittivity of PLZT_85/15_xHf at 1 kHz and 100 kHz measured at room temperature

As the permittivity relates to the density of the samples, the deviations at lower hafnium concentrations can be correlated with the density measurements. The curves for the geometrical and Archimedes density (Figure 33) show the same progression as the ones in Figure 37. It can be assumed that the influence of hafnium doping on the density of the samples too is a big influence on the permittivity.

In Figure 38 the loss factor of the PLZT_85/15 series is depicted. Increased frequency leads to higher losses, as was the case with the PLZT_90/10 series.

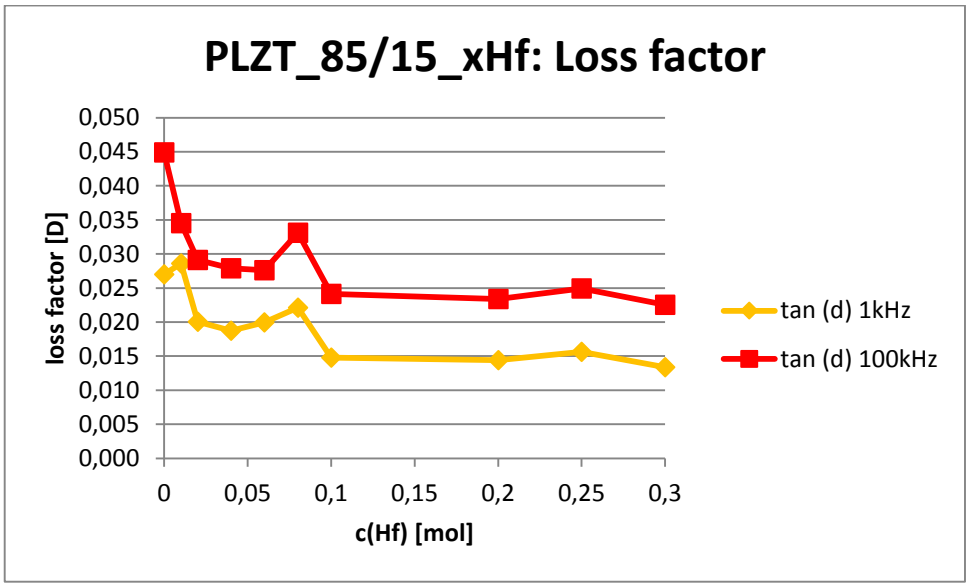

Figure 38 Loss factor of PLZT_85/15_xHf at 1 kHz and 100 kHz measured at room temperature

The loss factor decreases with increasing hafnium doping. The only exception is the sample with 8% hafnium, which shows a maximum just like the PLZT_90/10_8Hf sample. This may be because the doping content shifts the relaxation time of the material to a value which leads to the maximum dispersion of energy as the polarization cannot keep up with the alternating field.

In general the loss factor of the PLZT_85/15 series is higher than the loss factor of the PLZT_90/10 series, showing that higher titanium concentration increases the dielectric losses along with the permittivity.

4.2.4. High signal measurements

4.2.4.1. Permittivity versus temperature

When the permittivity and the loss factor are measured over a temperature range, both values show maxima at temperatures where structural changes (e.g. phase transitions) occur. Depicted in Figure 39 are the measurements taken of the PLZT_90/10_xHf series. No linear influence of the amount of hafnium doping on the height of the permittivity and the loss factor could be determined.

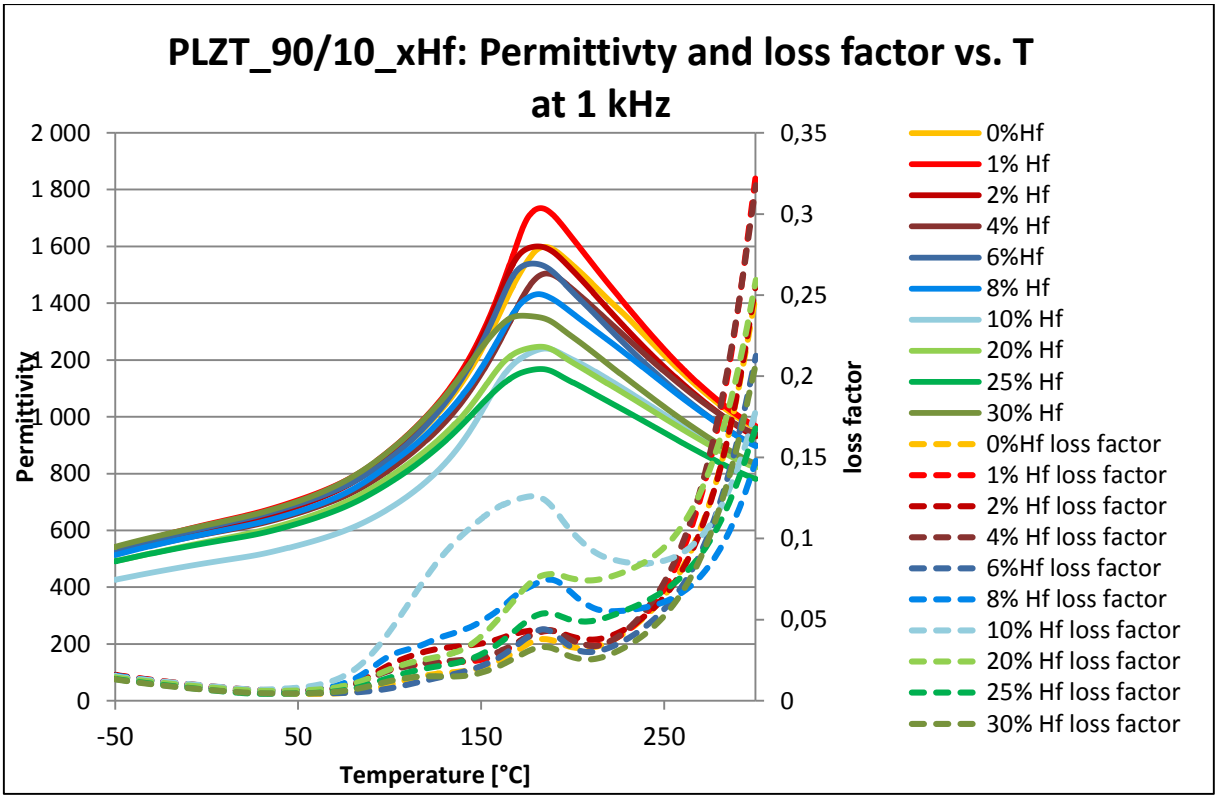

Figure 39 PLZT_90/10_xHf: Permittivity and loss factor vs. Temperature at 1 kHz

The permittivity measurements show one maximum at approximately 185°C. This maximum is present in all samples and is only slightly shifted with temperature (see Figure 41). The maxima first are rather sharply defined and become more diffuse when a hafnium content of 10 mol% is reached and exceeded. It seems that with the appearance of secondary phases the phase transition becomes more diffuse. Concerning the loss factor measurements two maxima can be determined. One maximum is around 115°C and one is at approximately 185°C.

In Figure 40the measurements of the PLZT_85/15_xHf series are depicted. Concerning the height of both permittivity and loss factor no linear influence of hafnium doping on the material could be observed.

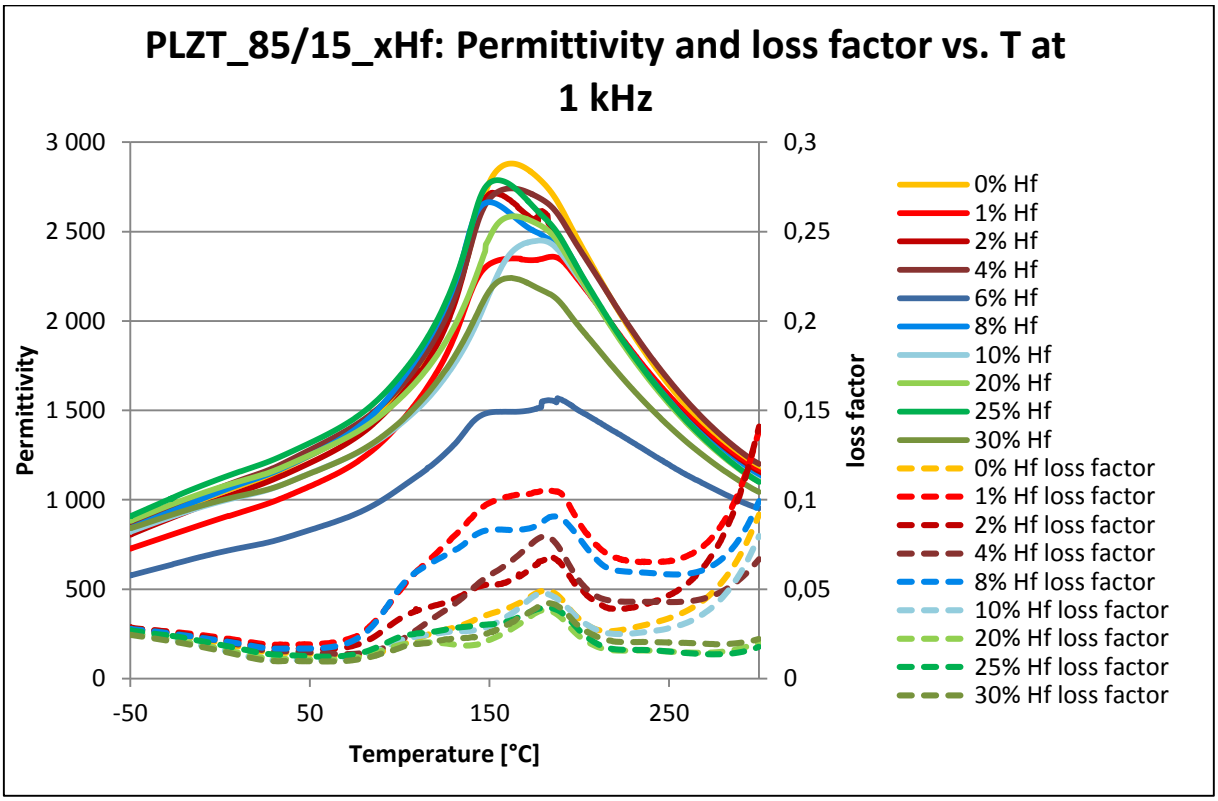

Figure 40 PLZT_85/15_xHf: Permittivity and loss factor vs. T at 1 kHz

Two maxima can be seen in the permittivity measurements. One is at approximately 185°C and one at about 155°C. The maximum at the lower temperature falls in the range of the antiferroelectric to paraelectric phase transition of pure PLZT, but is a bit higher. The one at the higher temperature is at the same range as the one of the PLZT_90/10_xHf series.

Measurements of the loss factor show both maxima present in the permittivity curves and an additional maxima at approximately 115°C. The maximum at 185°C is a rather sharp, well defined peak. The other two maxima are more diffuse in nature and overlap with each other.

In Figure 41the temperature of the maximum permittivity is shown for both series.

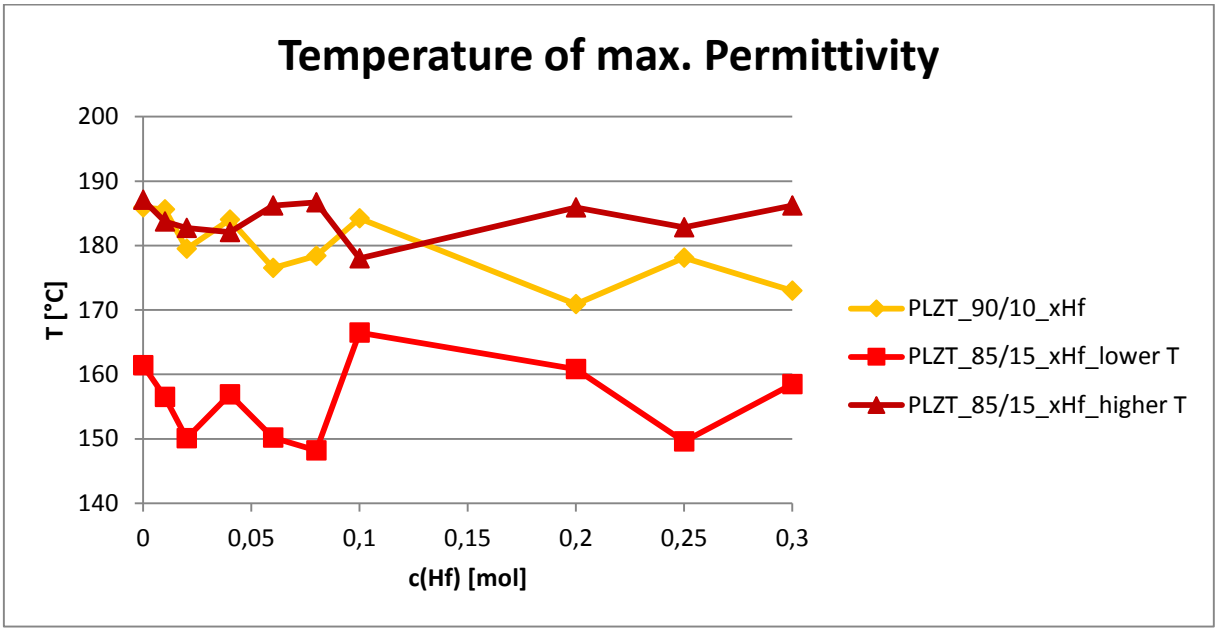

Figure 41 Temperature of max. permittivity

Both series have a maximum at about 185°C. The shifts in temperature with increasing hafnium content depicted here are diffuse and are most likely just scattering. The lower temperature present at higher concentration (>0,1) of thePLZT_90/10_xHf series may be caused by the formation of secondary phases in the material. A possible explanation for this maximum is a transition from anincommensurateantiferroelectric to a commensurate antiferroelectric, as it was observed by Asada et al. [22] in PLZT x/95/5.

The maximum at lower temperature of the PLZT_85/15_series scatters around 155°C. As the undoped sample has a maximum at a temperature higher than the one given in the phase diagram, it is likely that the exact stoichiometry was not achieved in the sample due to secondary phases or defects. The shifting of this maximum with varying hafnium content might be explained by the core/shell structure theory proposed by Ogihara et al. [23]. By forming cores of the undoped component surrounded by a shell of dopant the temperature dependence of the maximum permittivity is increased.

4.2.4.2. Polarization curves

The polarization of the samples was measured at varying fields. Important values obtained from this measurement are the forward switching field, the backward switching field and the area in between the two (hysteresis area). The forward switching field defines the maximum permittivity at high field and the hysteresis area is an indicator for how much loss to expect during the switching process.

Depicted inFigure 42 are the switching fields and the difference of the two switching fields (ΔE) of those samples of the PLZT_90/10_xHf series that were able to reach saturation polarization. All other samples reached breakdown voltage before saturation and broke. Therefore no values could be obtained. It is clear that hafnium doping has no influence on the polarization behavior of the samples. All three curves are flat and show neither decrease nor increase.

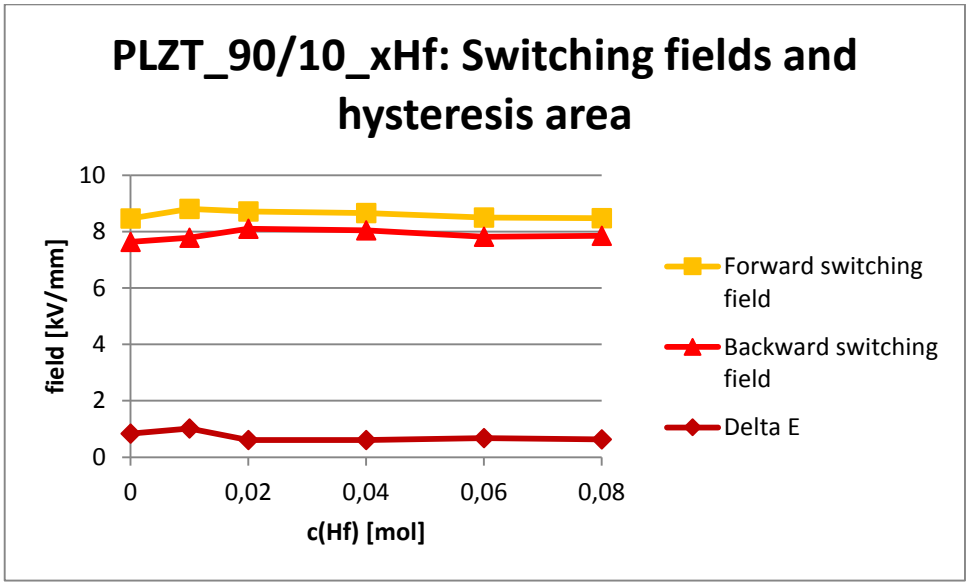

Figure 42 Switching fields and ΔE of the PLZT_90/10_xHf series

In Figure 43 the switching fields and the difference of the two switching fields are depicted. Both switching fields shift slightly to higher fields with increasing hafnium content. As the shift of the backward switching field is a bit steeper than the one for the forward switching field, a narrowing of the hysteresis curve occurs. This leads to a smaller hysteresis area and smaller losses in the material.

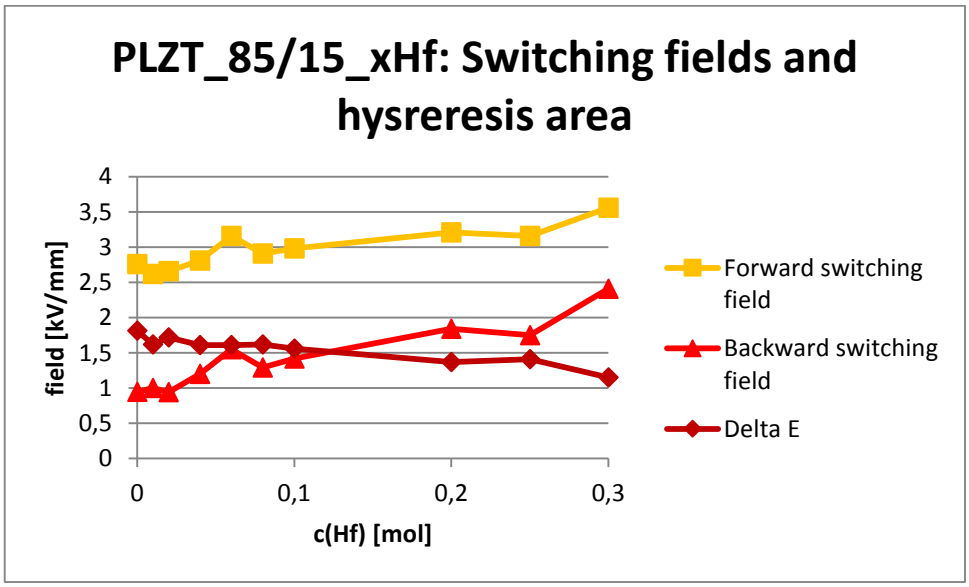

Figure 43 Switching fields and ΔE of the PLZT_85/15_xHf series

In comparison the PLZT_90/10_xHf series reaches higher field strengths with its saturation polarizations. This would be very desirable to increase the amount of energy storable in the material. The samples of the PLZT_85/15_xHf series saturate at much lower fields. Hafnium doping seems to reduce the losses in the PLZT_85/15_xHf series, but does not influence the stability or the saturation polarization.

5. Summary

To investigate the effect of substitution of zirconium by hafniumin lead lanthanum zirconatetitanate is the main aim of this thesis. Zirconium and hafnium differ only in their atomic mass, but not in their ionic radii or valency. Two compositions with different zircon to titanium ratio and varying hafnium content were prepared. using the following formula: $Pb_{0,91}La_{0,06}V_{Pb}^{II}{}_{0,03}(Hf_xZr_{1-x})_yTi_{1-y}$with titan content of either 0,1 or 0,15 and hafnium content ranging from 0 to 0,3. The series with y=0,9 is called PLZT_90/10_xHf and the series with y= 0,85 is called PLZT_85/15_xHf. The powders were synthesised using mixed oxide method with a calcination at 850°C for 3 hours. Cylindrical samples were formed by uniaxial pressing and sintering at 1250°C.

XRD measurements show that the inclusion of hafnium into the crystal lattice is only completed after sintering, as the calcination temperature is not high enough. The spectra of the calcinated samples show zirconium oxide and lead hafnate secondary phases, which disappear after sintering. The unit cell volume calculated shows a slight decrease with higher hafnium concentration for both series.

The SEM images taken of both series show that at hafnium content greater that 10 mol% lead hafnate secondary phases are still present in the material, even though they could not be detected with the XRD measurements. Increasing hafnium content leads to higher relative densities for the PLZT_90/10_xHf series decreasing the porosity of the samples. The average grain size was determined by line cut and intercept method. For both series a decline in grain size with increasing hafnium concentration was observed.

The density of the samples was determined using the geometrical density, the Archimedes principle and calculations using the XRD data (leading to the theoretical density).Density measurements show an increase in all three values with higher hafnium doping for both series. When comparing the measured density to the theoretical equivalent, densities above 95% of the theoretical value were achieved for all samples, indicating a satisfying densification during sintering.

The permittivity and loss factor of the samples were measured at 1 kHz and 100 kHz. Hafnium doping has no influence on the two parameters. However the higher titanium content of the PLZT_85/15_xHf series increases permittivity by 30%. The only value significantly influenced by the different frequencies used was the loss factor, which was higher at 100 kHz.

Permittivity and the loss factor were measured against the temperature in order to determine transition temperatures and describe any shift caused by the Hafnium substitution.

The permittivity measurements of the PLZT_90/10_xHf series show a maximum at 185°C that could not be attributed to any known phase transition. The loss factor measurements show a maximum at 185°C and on at 115°C. The maximum at lower temperature might be an antiferroelectric to antiferroelectric phase transition. Hafnium doping does not shift the temperature of the peak. For the PLZT_85/15_xHf series the same maxima could be detected. However an additional maximum at approximately 155°C was detected. However no linear trend could be observed.

Hafnium doping has no influence on the maximum polarization of the samples. However the switching field was shifted to lower fields and the hysteresis area was decreased with increasing hafnium content for both series.

In summary it can be said, that hafnium doping only has a significant impact on the switching field of PLZT.Other changes observed in the materialare either diffuse in nature or may be caused by secondary phases present in the material. Considering the much bigger influence of the Ti-content on electric parameters and phase transitions, it is obvious that a difference in ionic radius between dopant and replaced ion is much more important for the properties of the material than a difference in atomic mass.

6. References

[1] EPCOS OHG (TDK-EPC); Stand 27.11.2014; http://www.epcos.de/epcos/192854/tech-library/artikel/products---technologies/article-products---technologies/ceralink----eine-neue-technologie-fuer-zwischenkreise/192110

[2] Heremans, C., Tuller, H. L.; J. Eur. Ceram. Soc.; (1999); 19; 1133-37

[3] Burn, I., Smith, D. M.; (1972);*J. Mat. Sci.;7*(3); 339-343.

[4] Haertling, G. H.; (1999); J. Am. Ceram. Soc.; 82; 797-818

[5] Liu, H., Dkhil, B.; (2011); Z. Kristallogr.; 226; 163-170

[6] Tan, X., Ma, C., Frederick, J., Beckman, S., Webber, K. G.; (2011); J. Am. Ceram. Soc.; 94; 4091-4107

[7] Gachigi, K. (1997). *Electrical energy storage in antiferroelectric-ferroelectric phase switching, chemically modified lead zirconate ceramics*. Pennsylvania State University

[8] Gröting, M., Albe, K.; (2014); Journal of Solid State Chemistry; 213; 138-144

[9] Goldschmidt, V. M.; (1926); Die Naturwissenschaften; 21; 477-85

[10] Shirane, G., Suzuki, K., Takeda, A.; (1952); J. Phys. Soc. Japan; 7; 12

[11] Jaffe, B., Cook, W. R., Jaffe, H.; (1971); Piezoelectric Ceramics; Academic Press.

[12] Cao, W., Cross, E. L.; (1993) Phys. Rev. B; 47; 4825

[13] Noheda, B., Cox, D. E., Shirane, G., Gonzalo, J. A., Cross, L. E.,Park, S-E.; (1999); Appl. Phys. Lett; 74; 2059

[14] Jaffe, B., Roth, R. S., Marzullo, S.; (1954); J. Appl. Phys.; 25; 809-10

[15] Newnham, R. E.; (2008); *Properties of materials*;

[16] Haertling, G. H.; Land, C. E.; (1971); J. Am. Ceram. Soc; 54; 1

[17] Gonnard, P., Troccaz, M.; (1978); J. Solid State Chem.; 23; 321-26

[18] Banerjee, A., Bandyopadhyay, A., Bose, S.; J. Am. Ceram. Soc.; (2006); 89 [5]; 1594-1600

[19] Moulson, A. J., Herbert, J. M.; Electroceramics: Materials, properties, applications; (2003); 2nd edition

[20] Yu, Y., Tu, J., Singh, R. N.; J. Am. Ceram. Soc.; (2001); 84; 333-340

[21] DIN 50601,Metallografische Prüfverfahren, Ermittlung der Ferrit- oder Austenitkorngröße von Stahl und Eisenwerkstoffen

[22] Asada, T., Koyama, Y.; Physical Review B; (200); 70; 104105

[23] Ogihara, H., Randall, C. A., Trolier-McKinstry, S.; J. Am. Ceram. Soc.; (2009); 92; 110-118

7. List of Figures

8. List of Tables

9. Annex

9.1. Schemes of Permittivity versus temperature measurements

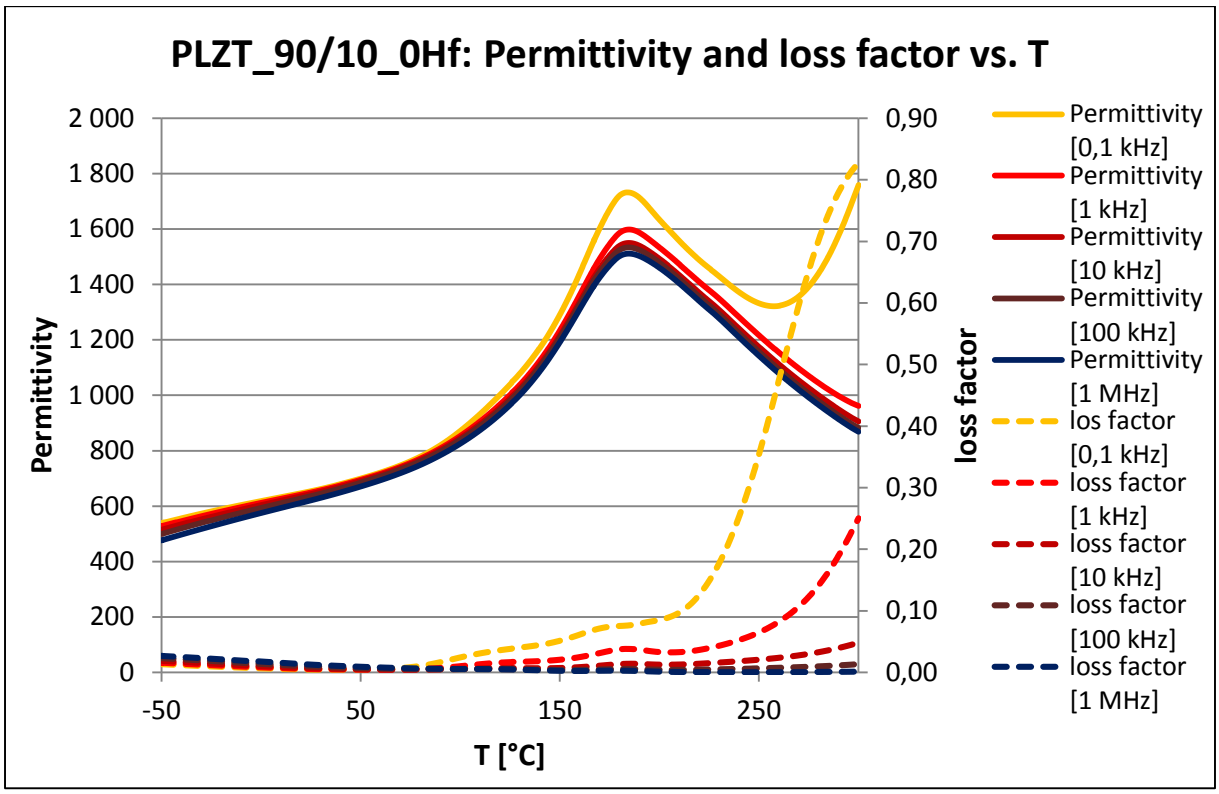

Scheme 1 PLZT_90/10_0Hf: Permittivity and loss factor vs. Temperature

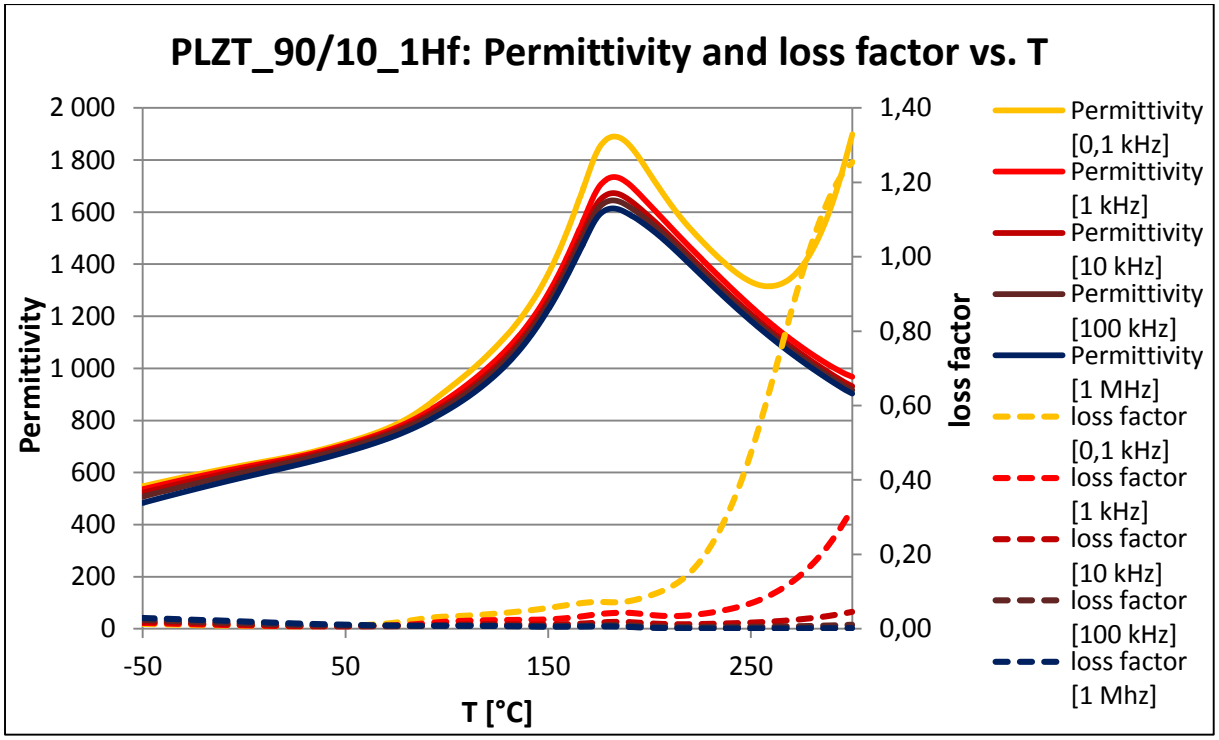

Scheme 2 PLZT_90/10_1Hf: Permittivity and loss factor vs. Temperature

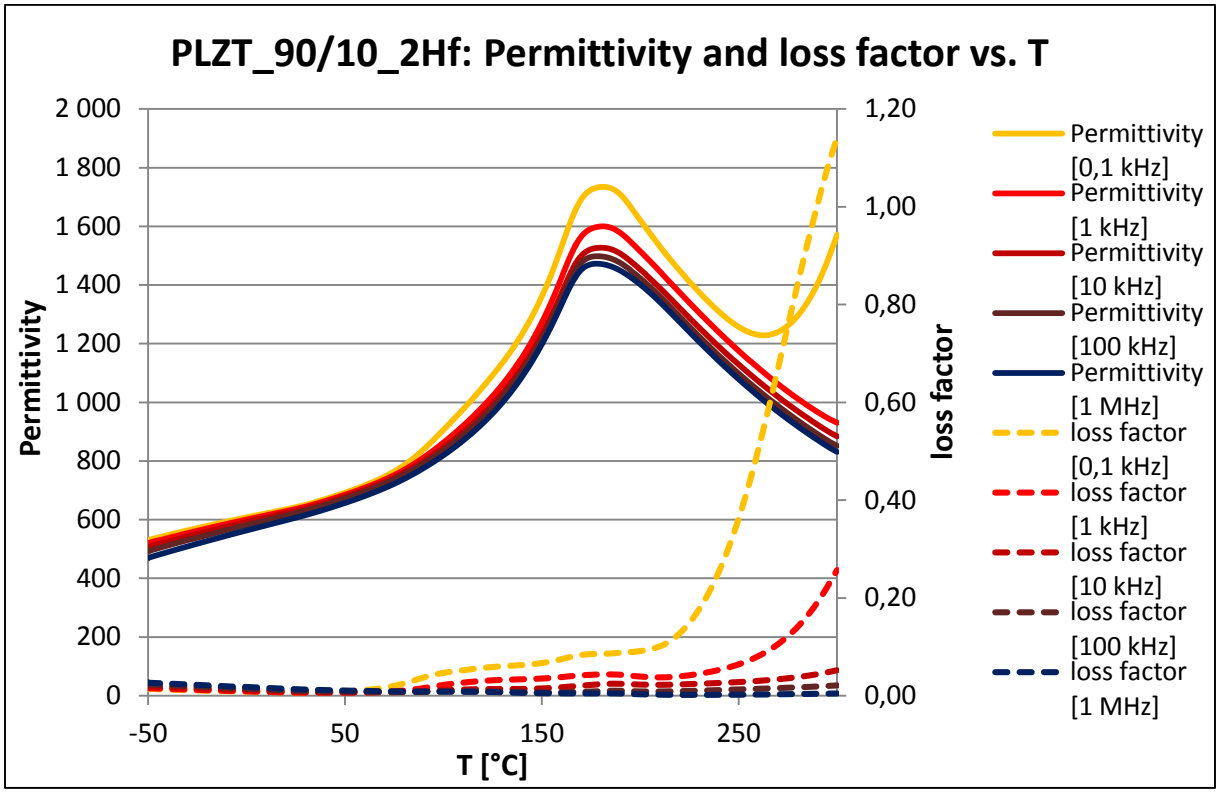

Scheme 3 PLZT_90/10_2Hf: Permittivity and loss factor vs. Temperature

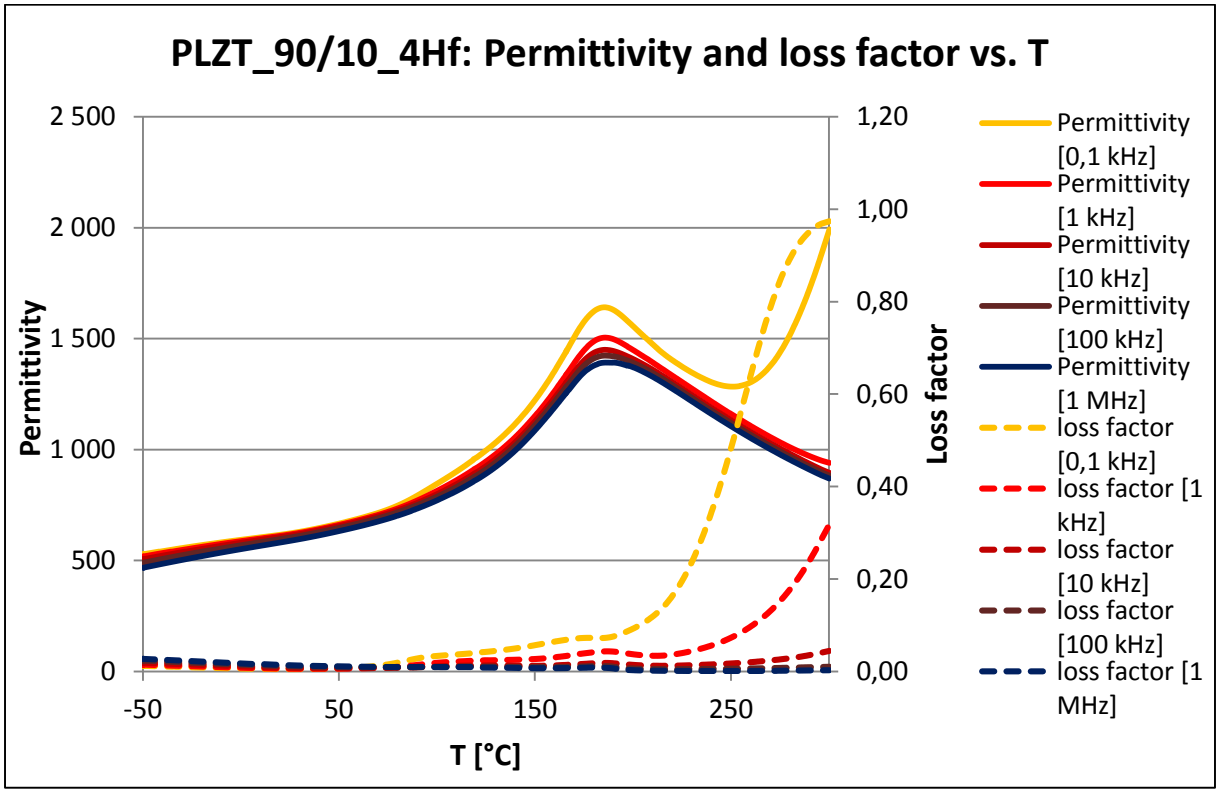

Scheme 4 PLZT_90/10_4Hf: Permittivity and loss factor vs. Temperature

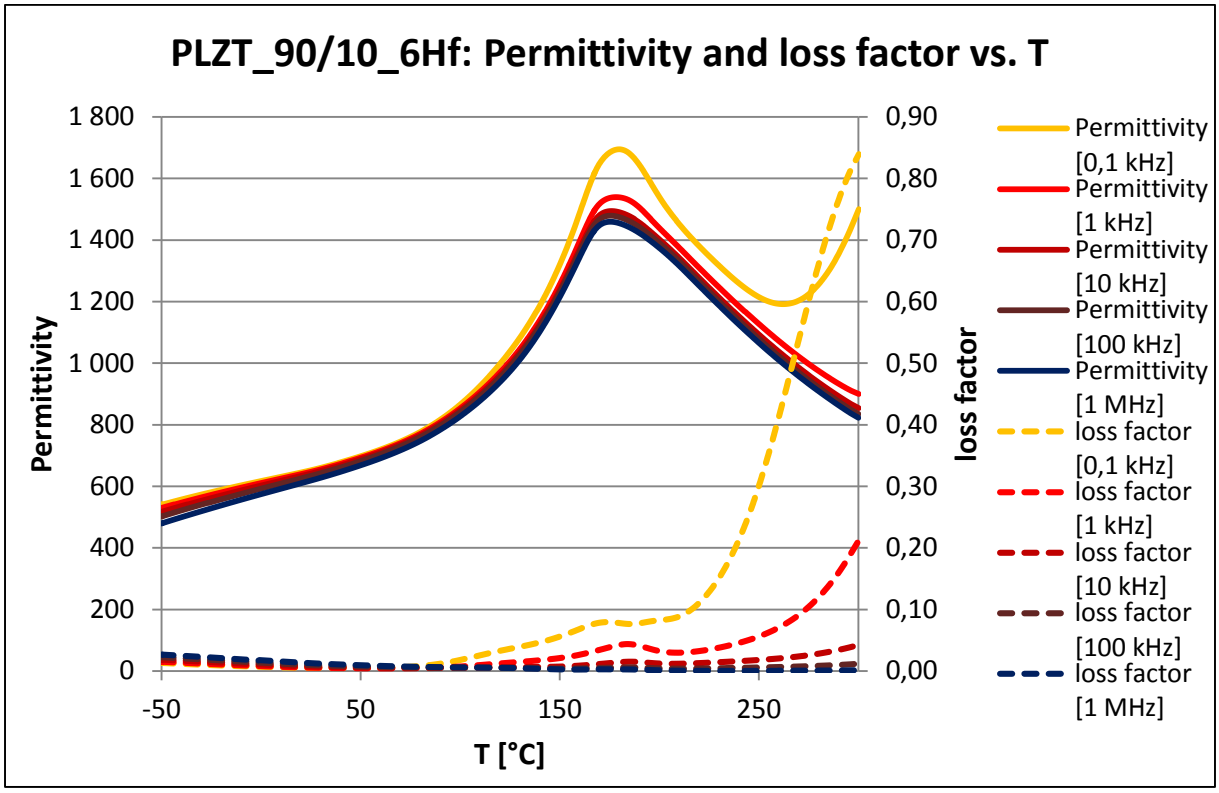

Scheme 5 PLZT_90/10_6Hf: Permittivity and loss factor vs. Temperature

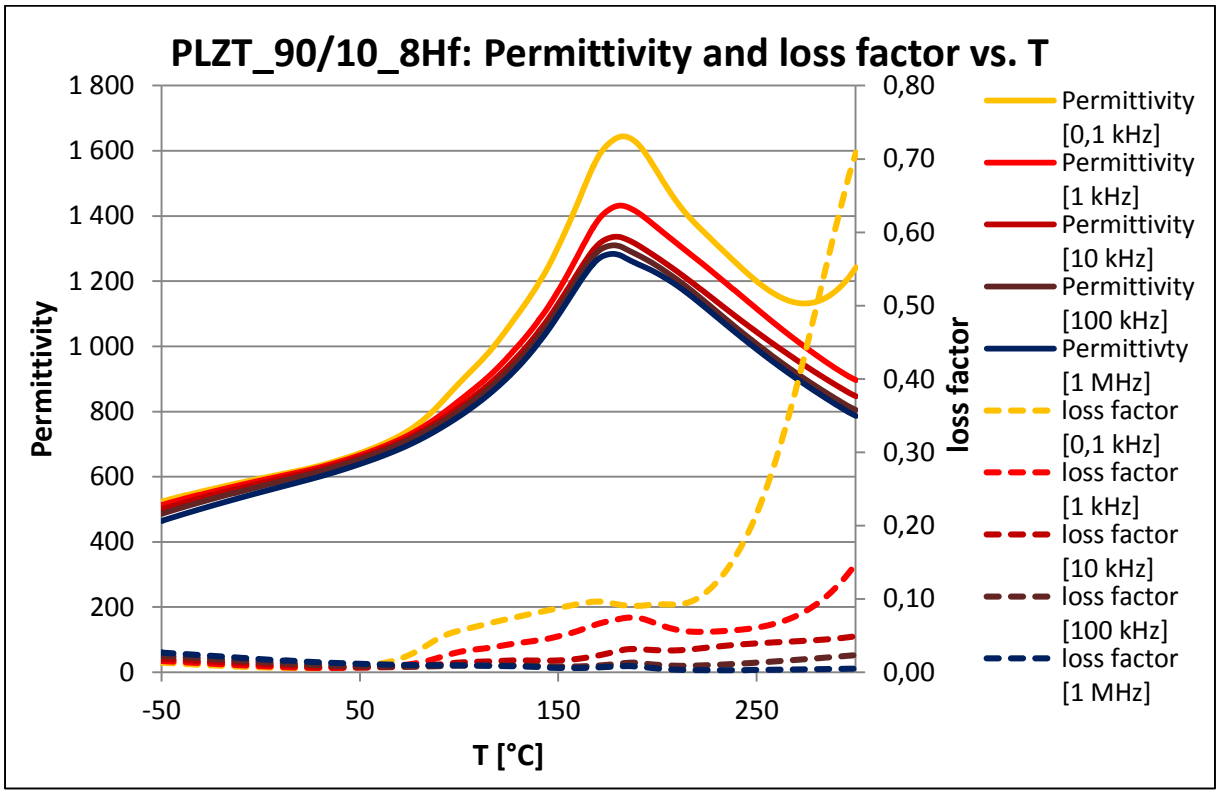

Scheme 6 PLZT_90/10_8Hf: Permittivity and loss factor vs. Temperature

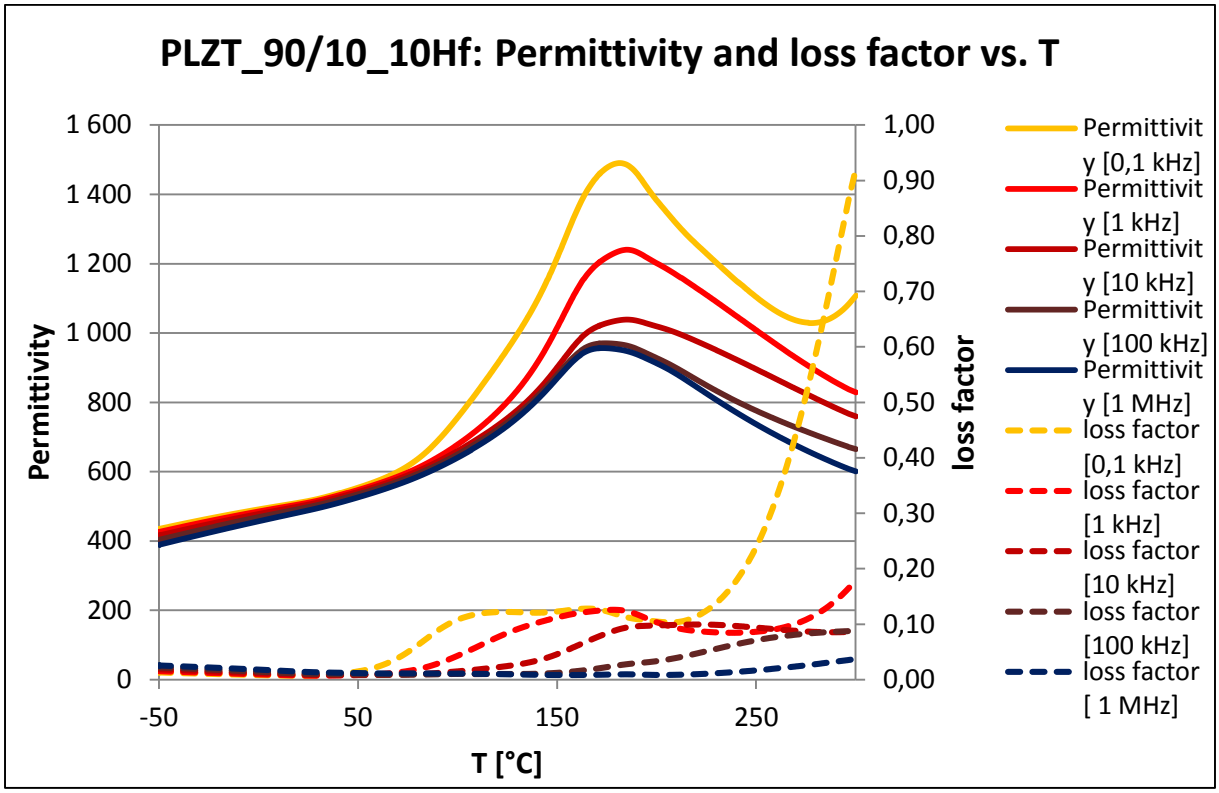

Scheme 7 PLZT_90/10_10Hf: Permittivity and loss factor vs. Temperature

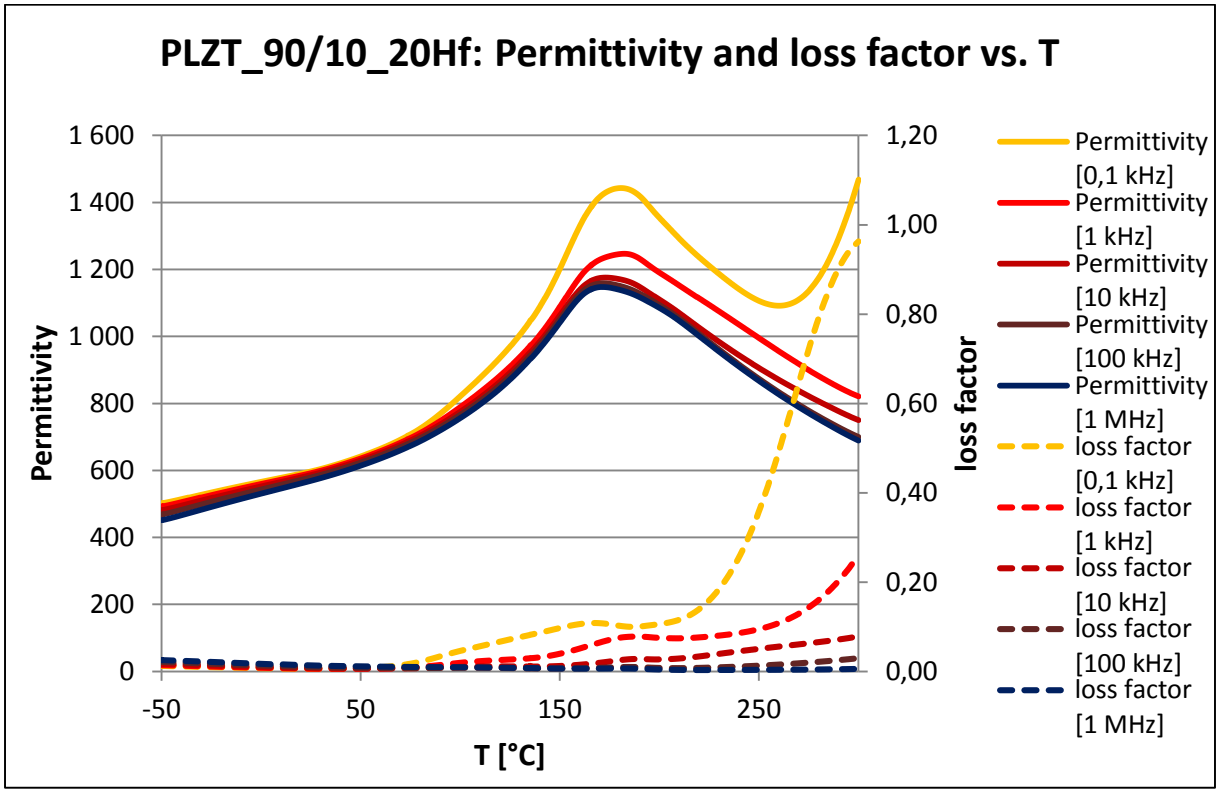

Scheme 8 PLZT_90/10_20Hf: Permittivity and loss factor vs. Temperature

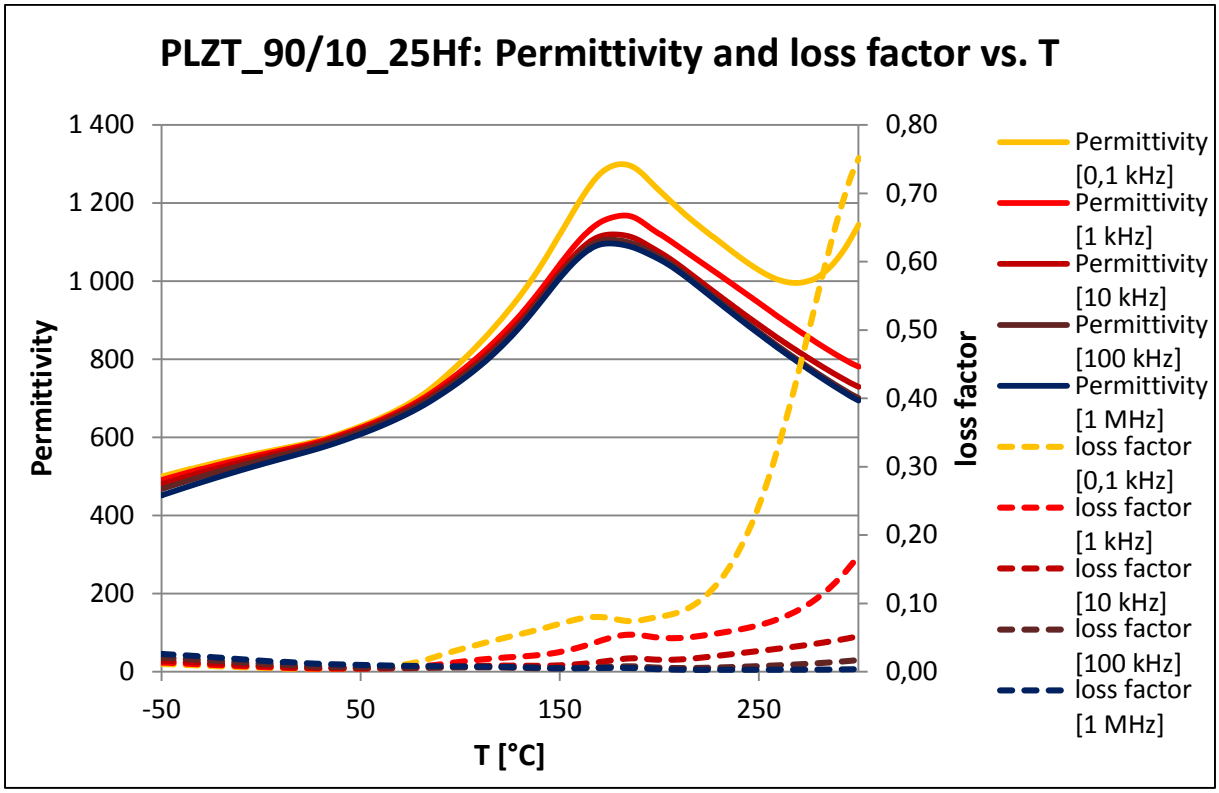

Scheme 9 PLZT_90/10_25Hf: Permittivity and loss factor vs. Temperature

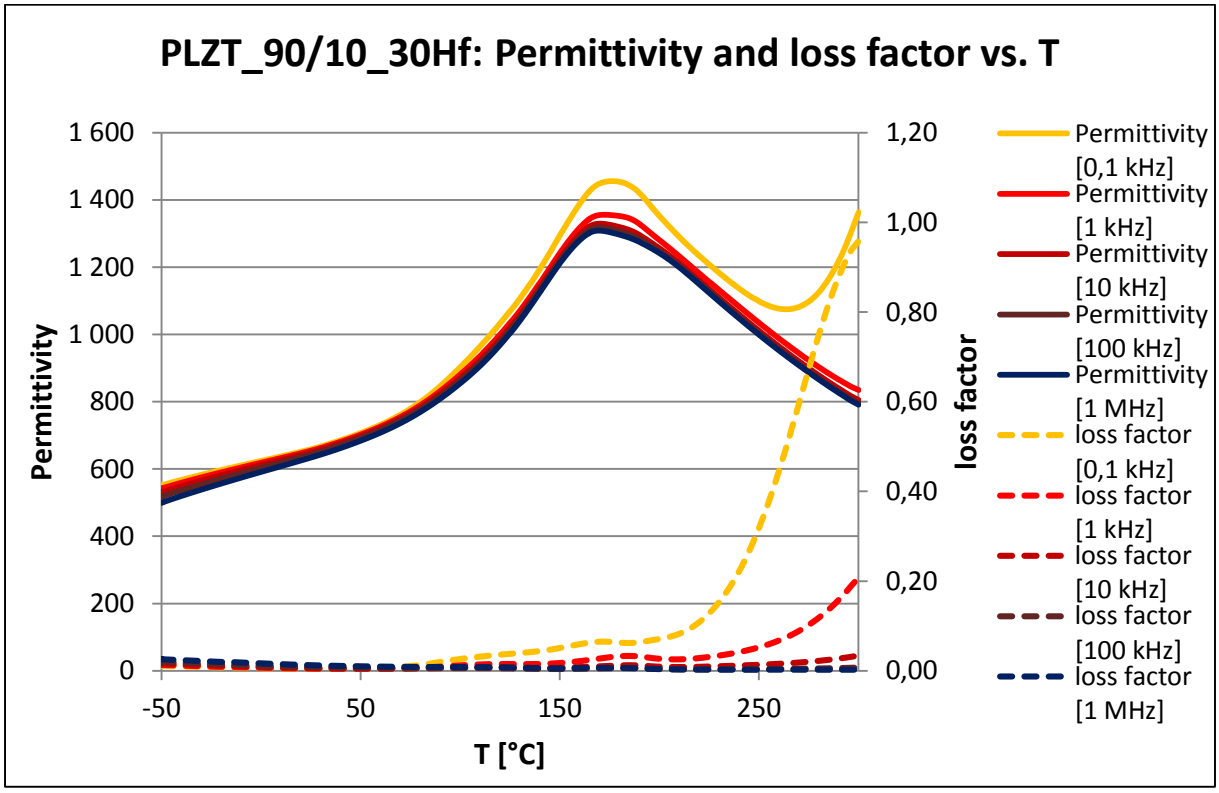

Scheme 10 PLZT_90/10_30Hf: Permittivity and loss factor vs. Temperature

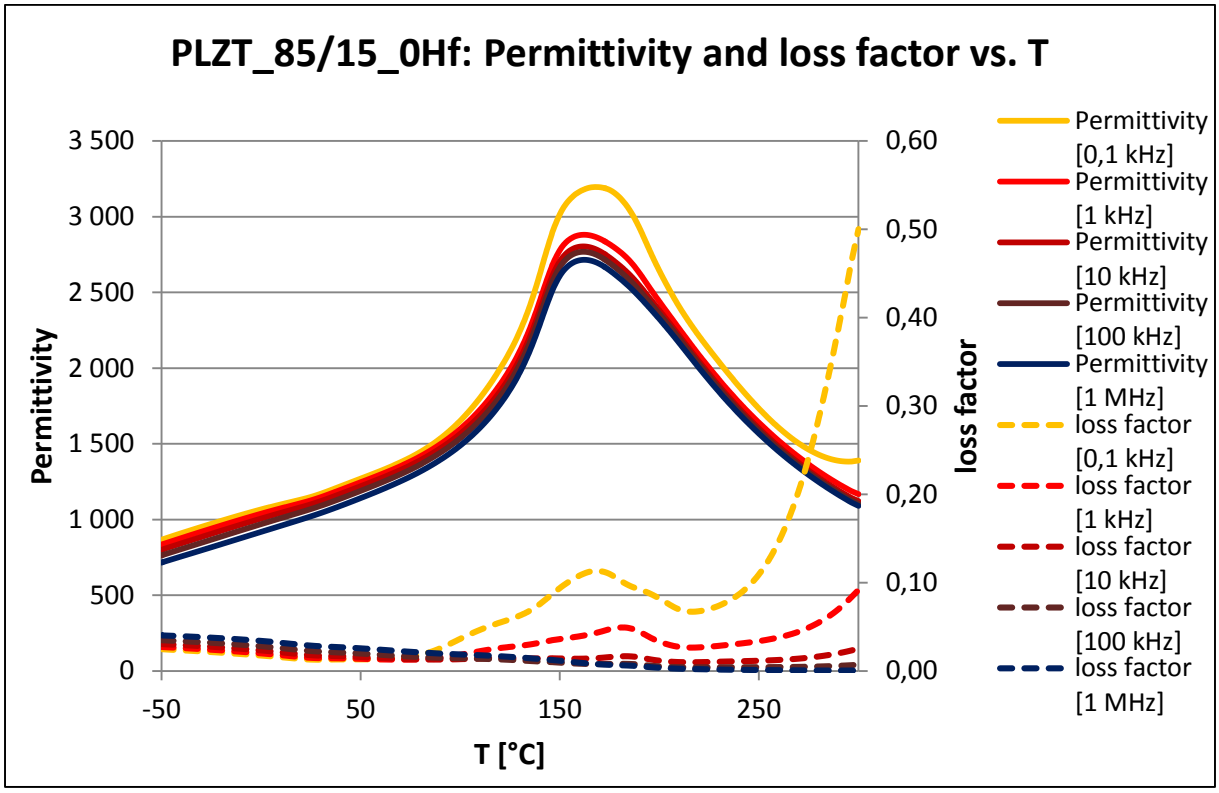

Scheme 11 PLZT_85/15_0Hf: Permittivity and loss factor vs. Temperature

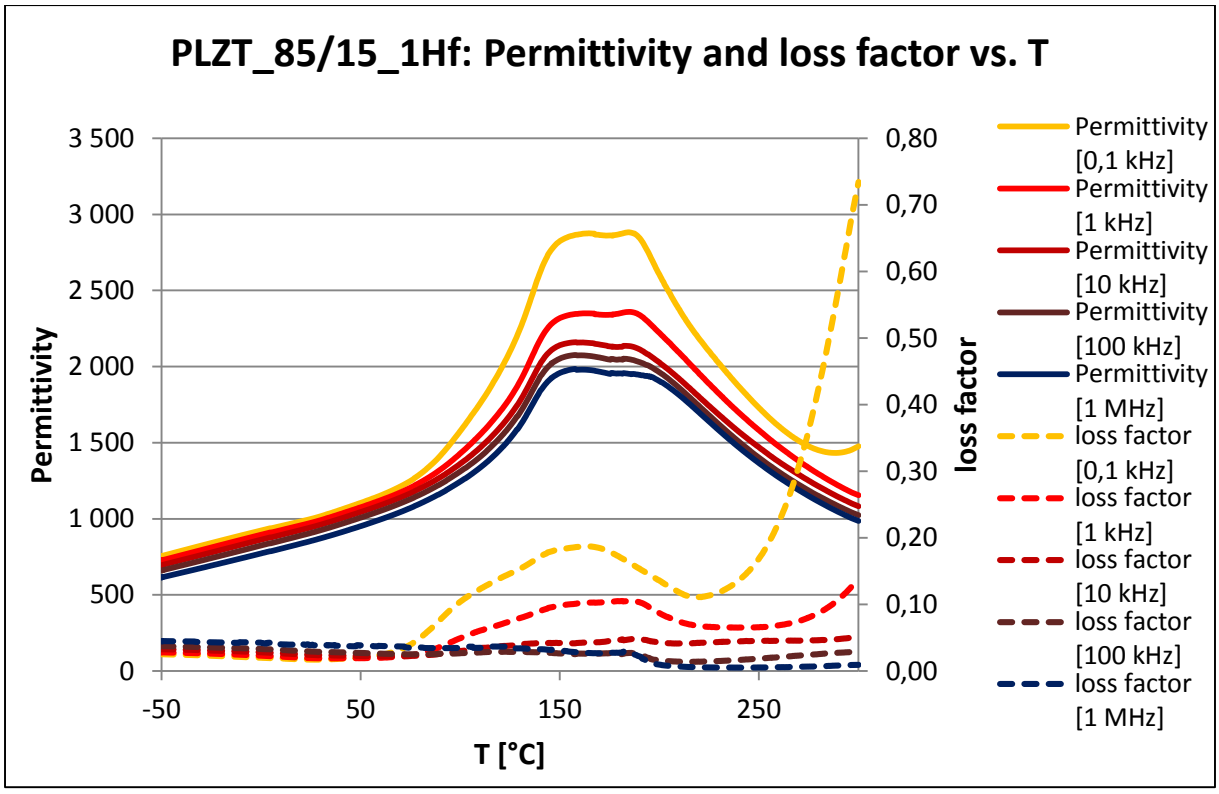

Scheme 12 PLZT_85/15_1Hf: Permittivity and loss factor vs. Temperature

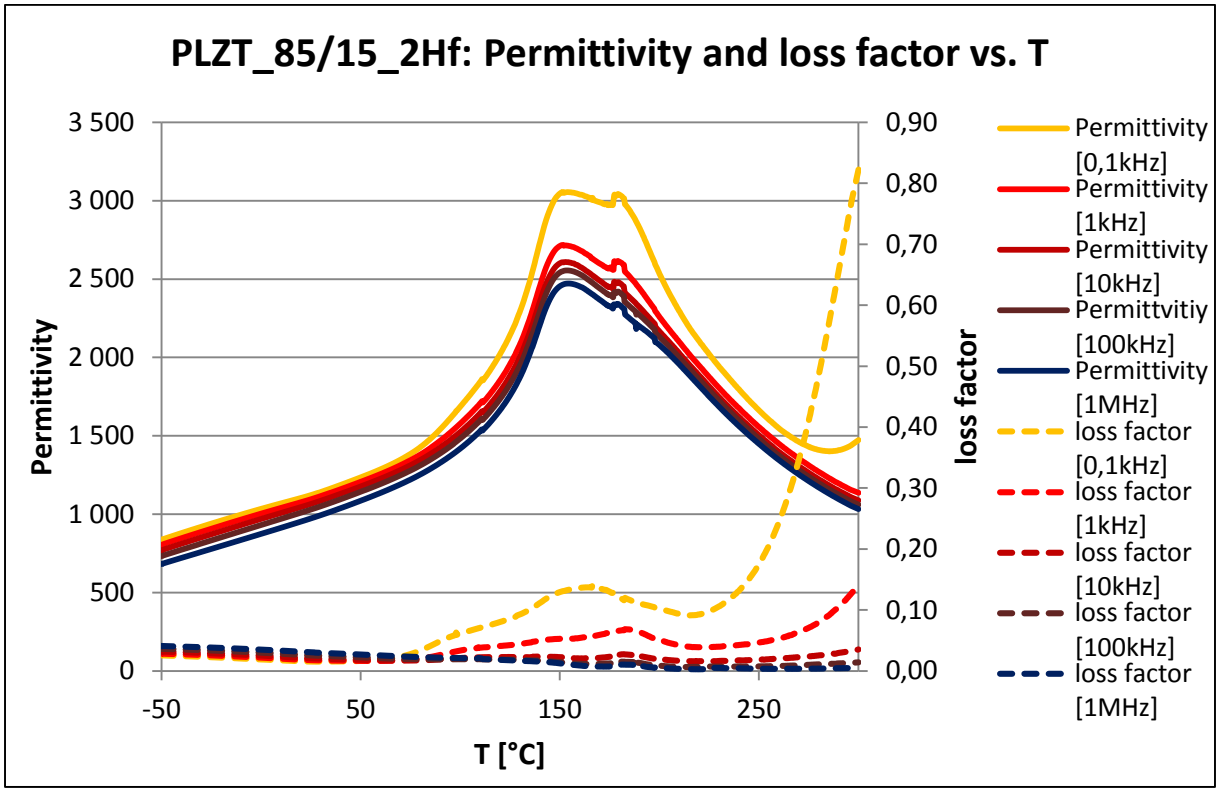

Scheme 13 PLZT_85/15_2Hf: Permittivity and loss factor vs. Temperature

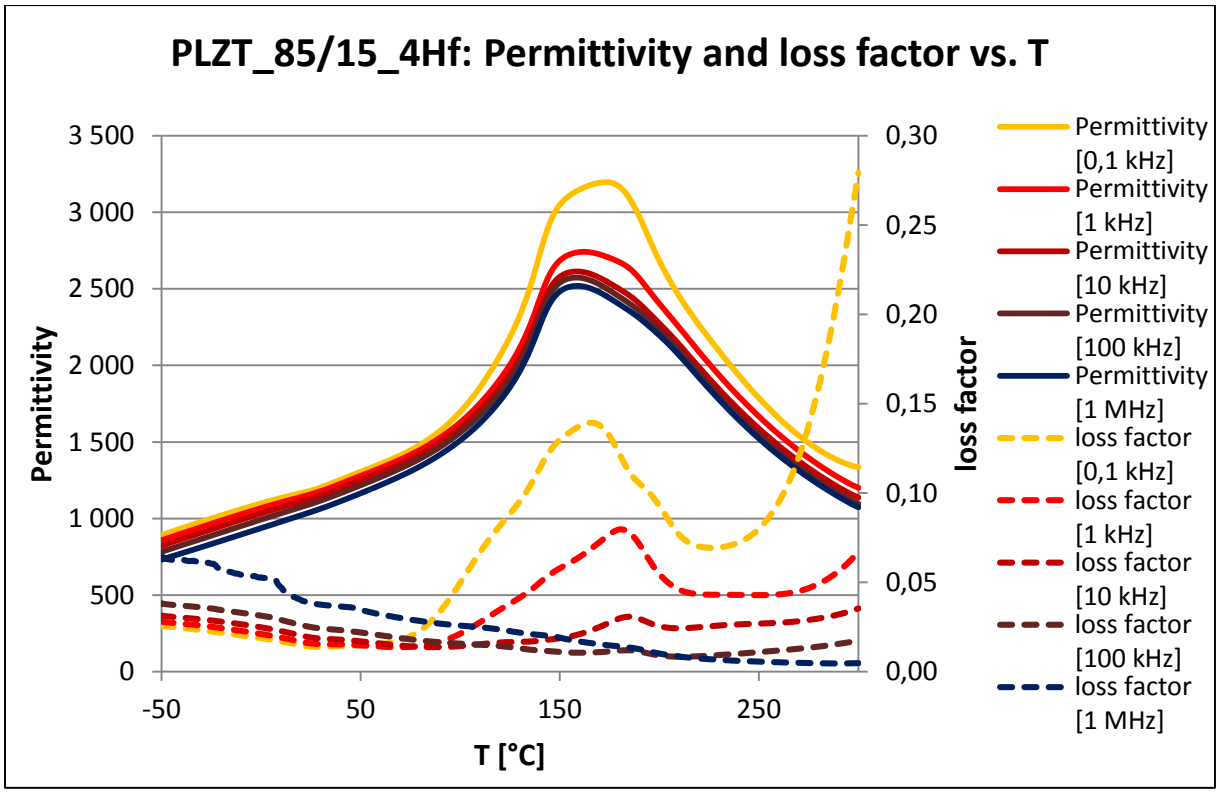

Scheme 14 PLZT_85/15_4Hf: Permittivity and loss factor vs. Temperature

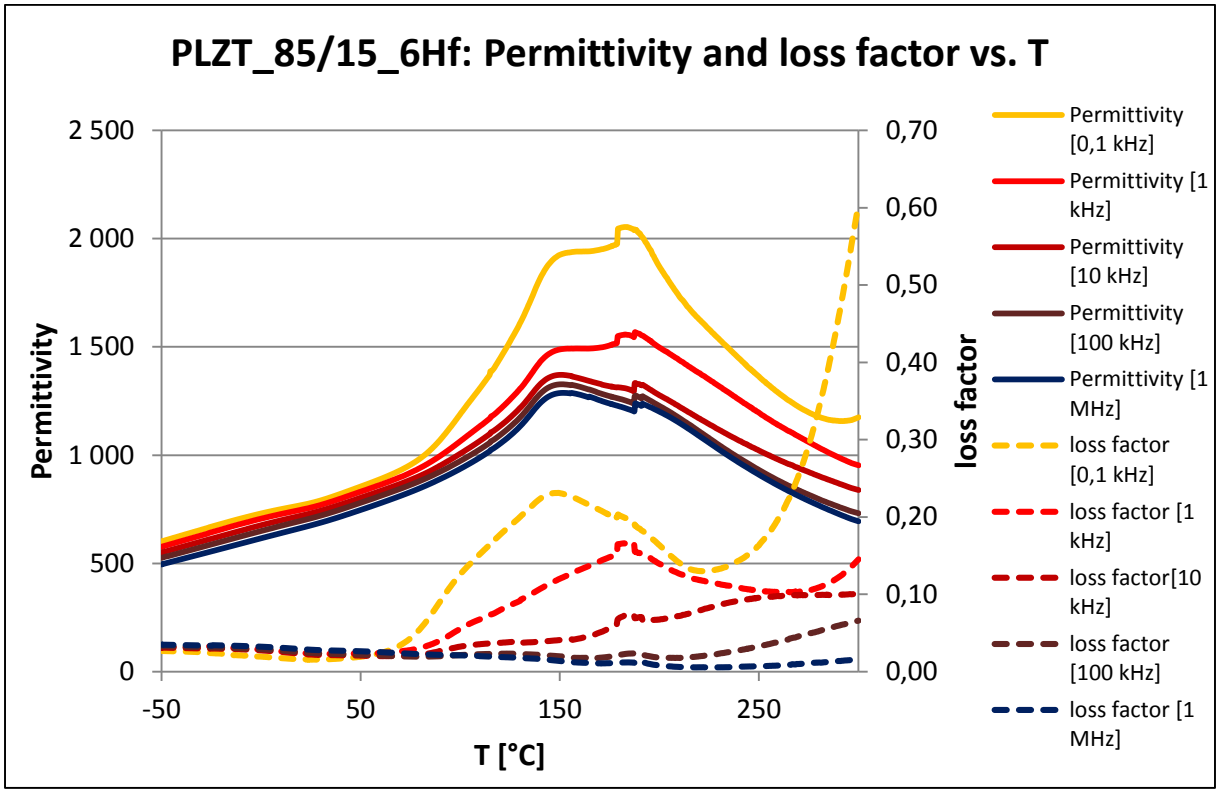

Scheme 15 PLZT_85/15_6Hf: Permittivity and loss factor vs. Temperature

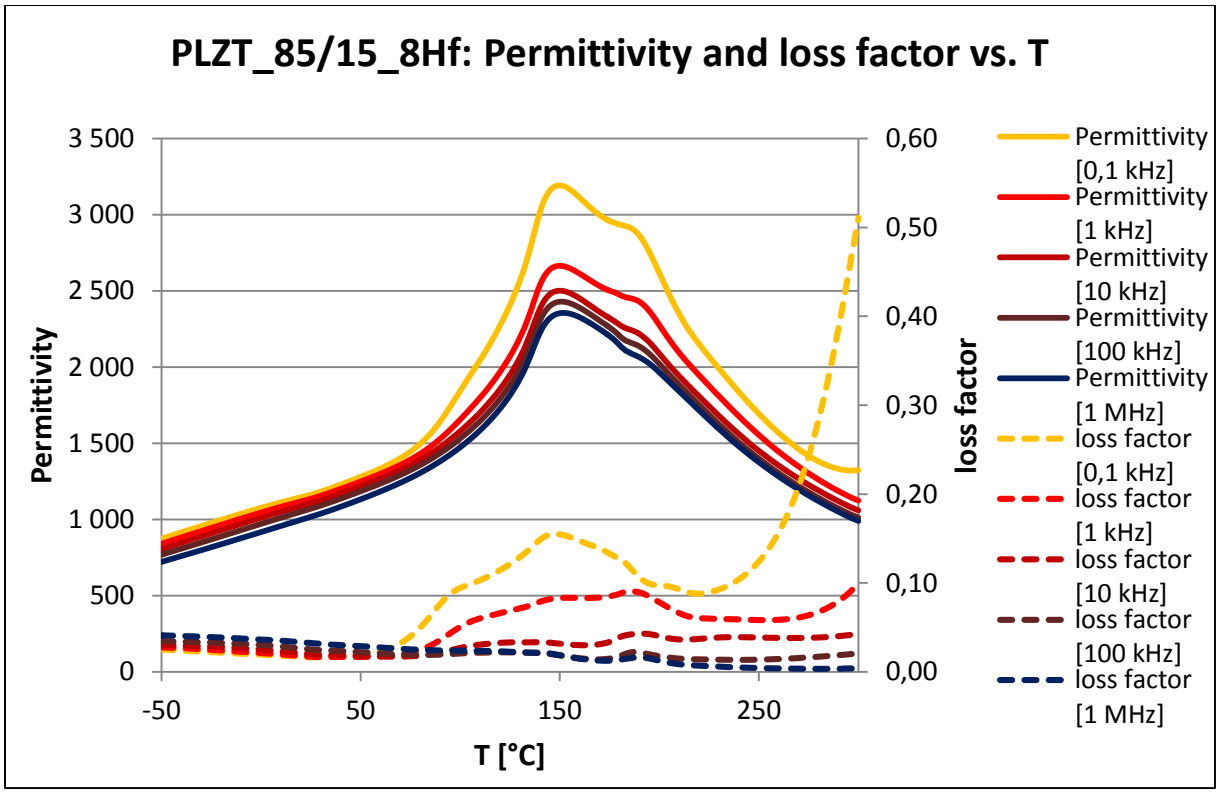

Scheme 16 PLZT_85/15_8Hf: Permittivity and loss factor vs. Temperature

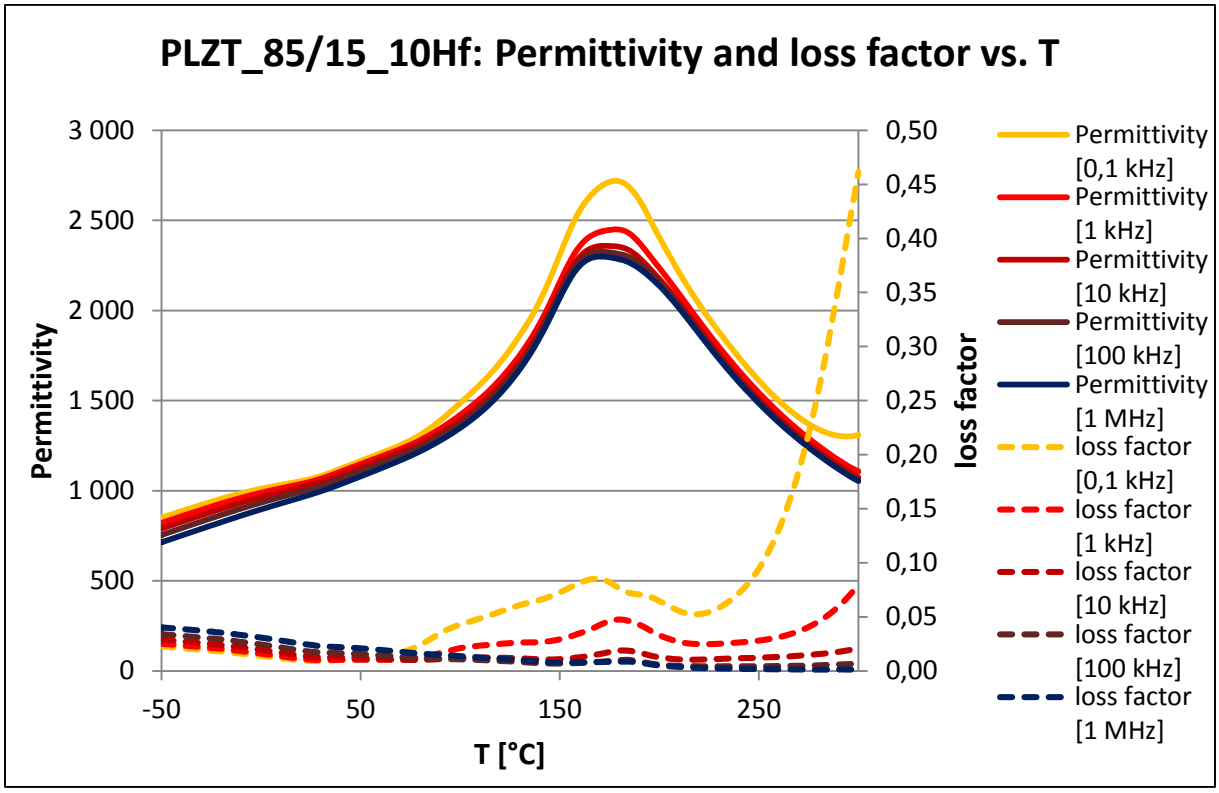

Scheme 17 PLZT_85/15_10Hf: Permittivity and loss factor vs. Temperature

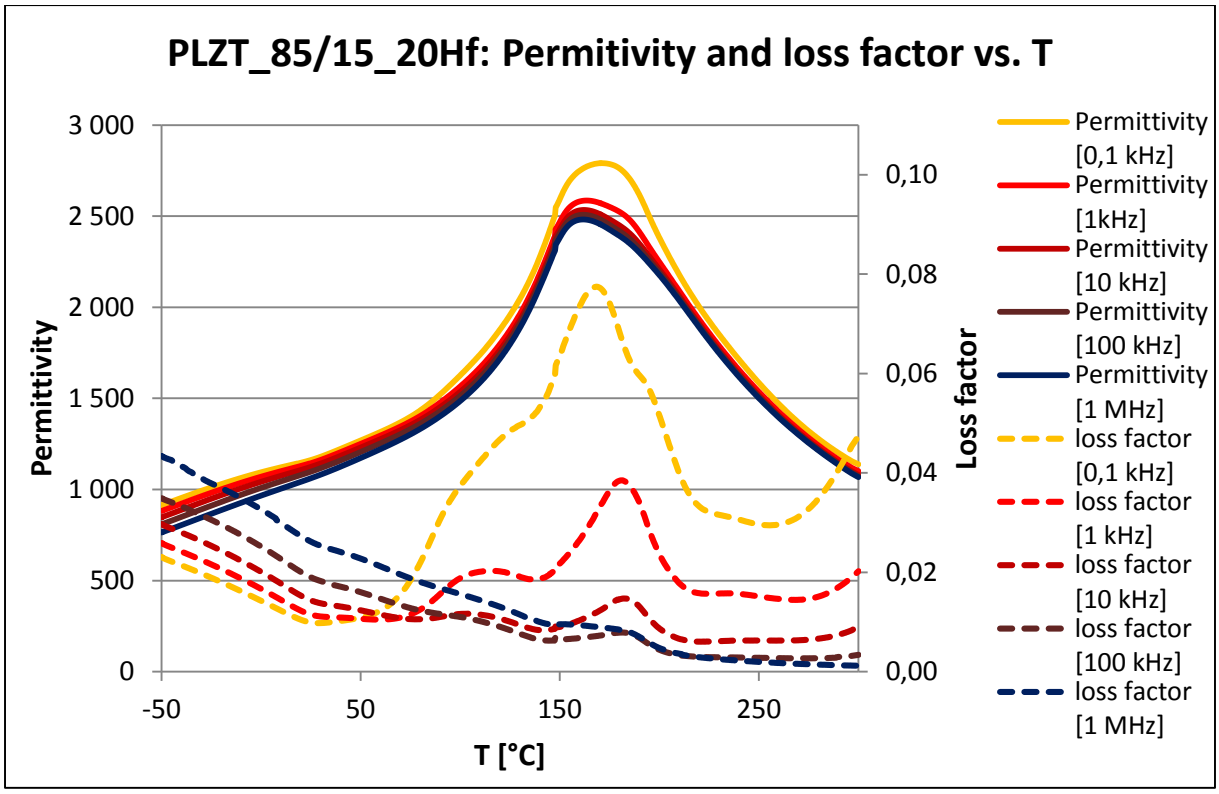

Scheme 18 PLZT_85/15_20Hf: Permittivity and loss factor vs. Temperature

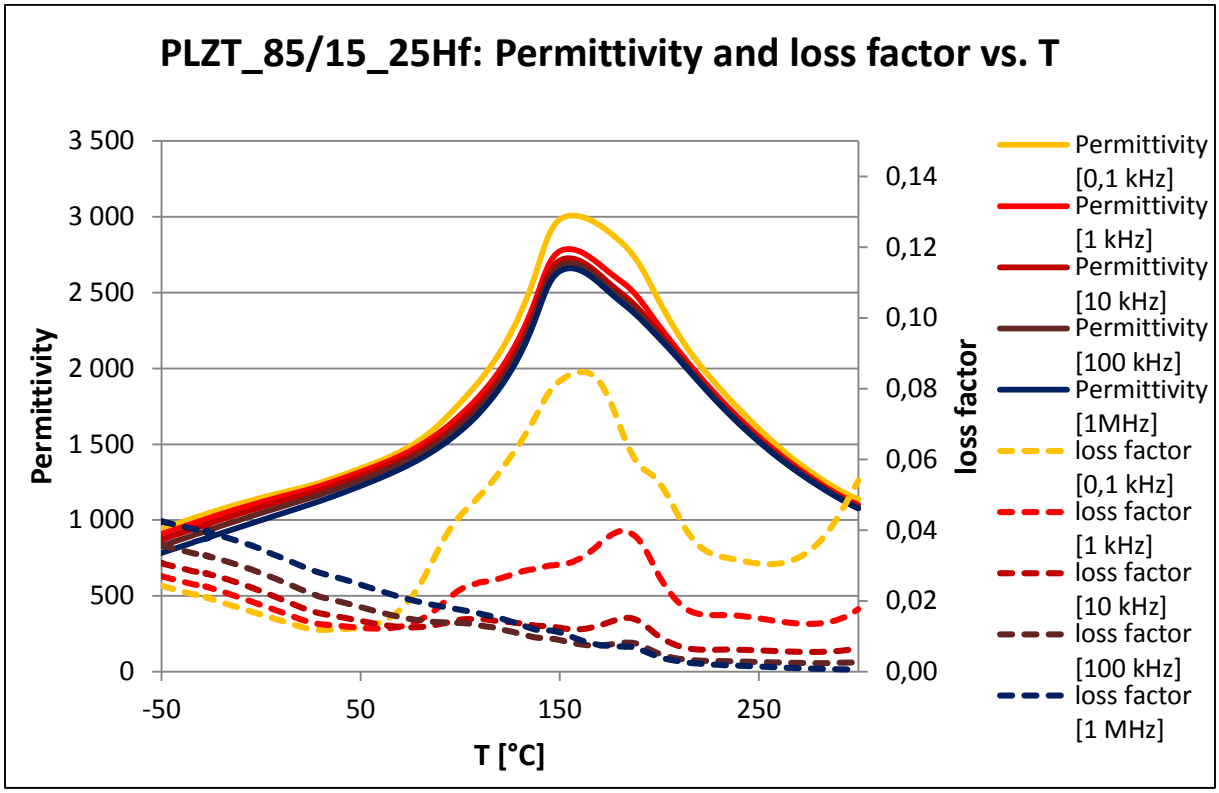

Scheme 19 PLZT_85/15_25Hf: Permittivity and loss factor vs. Temperature

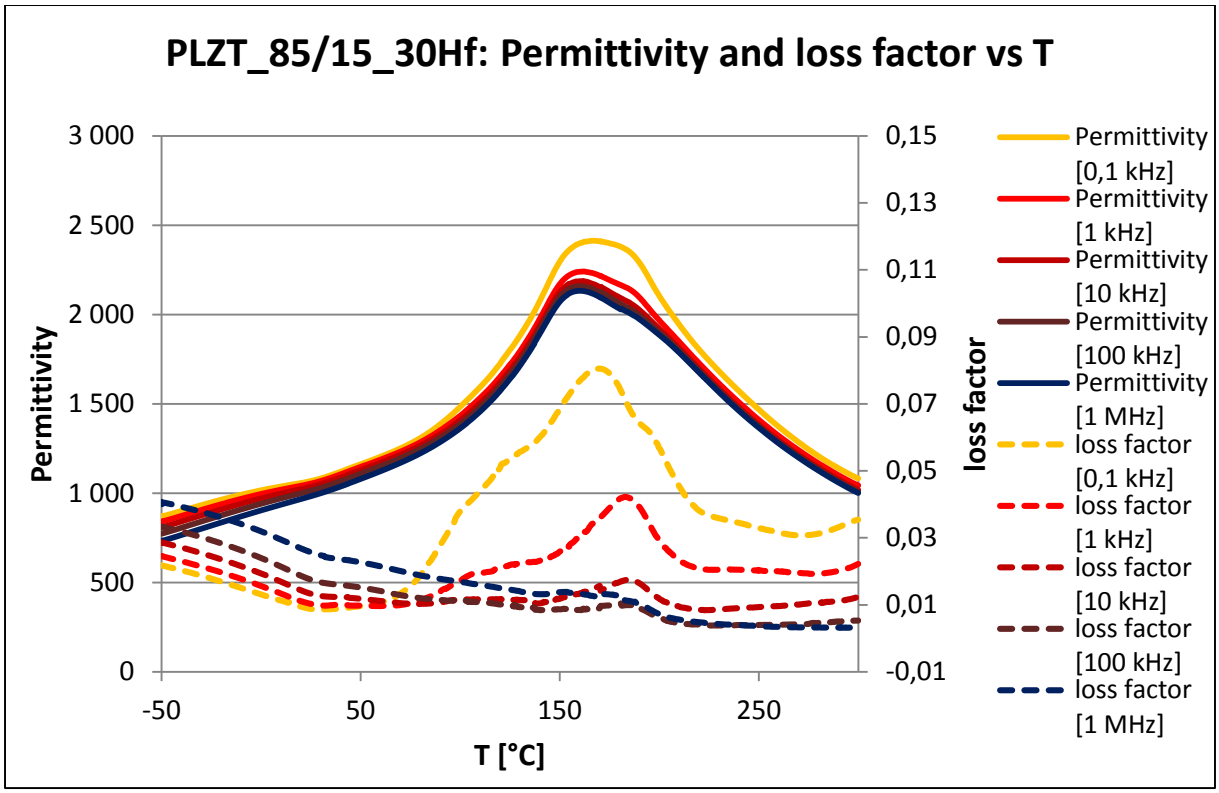

Scheme 20 PLZT_85/15_30Hf: Permittivity and loss factor vs. Temperature

9.2. SE/BSE microscopy images

9.2.1. PLZT_90/10_xHf:

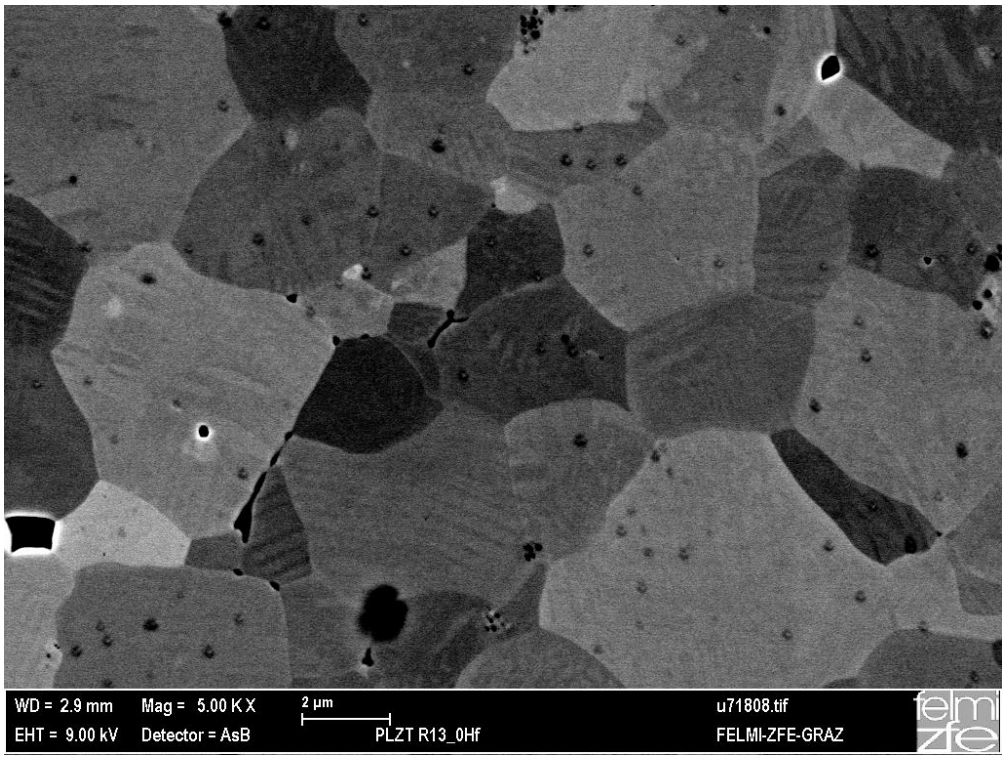

Figure 44 BSE image of PLZT_90/10_0Hf

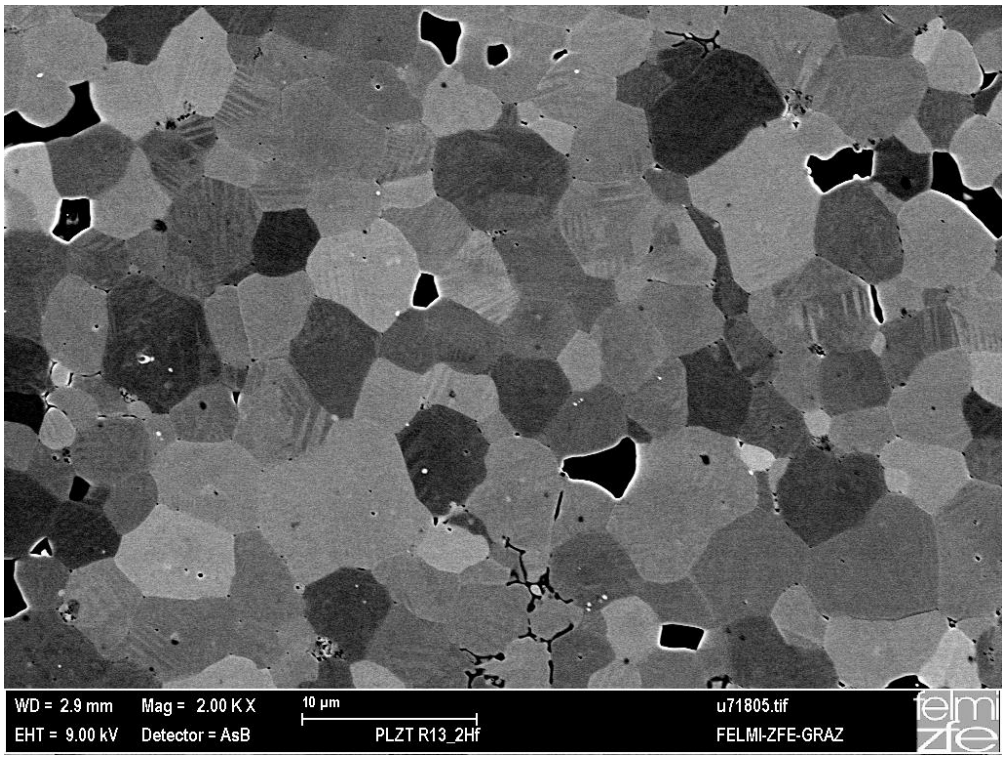

Figure 45 BSE imageof PLZT_90/10_2Hf

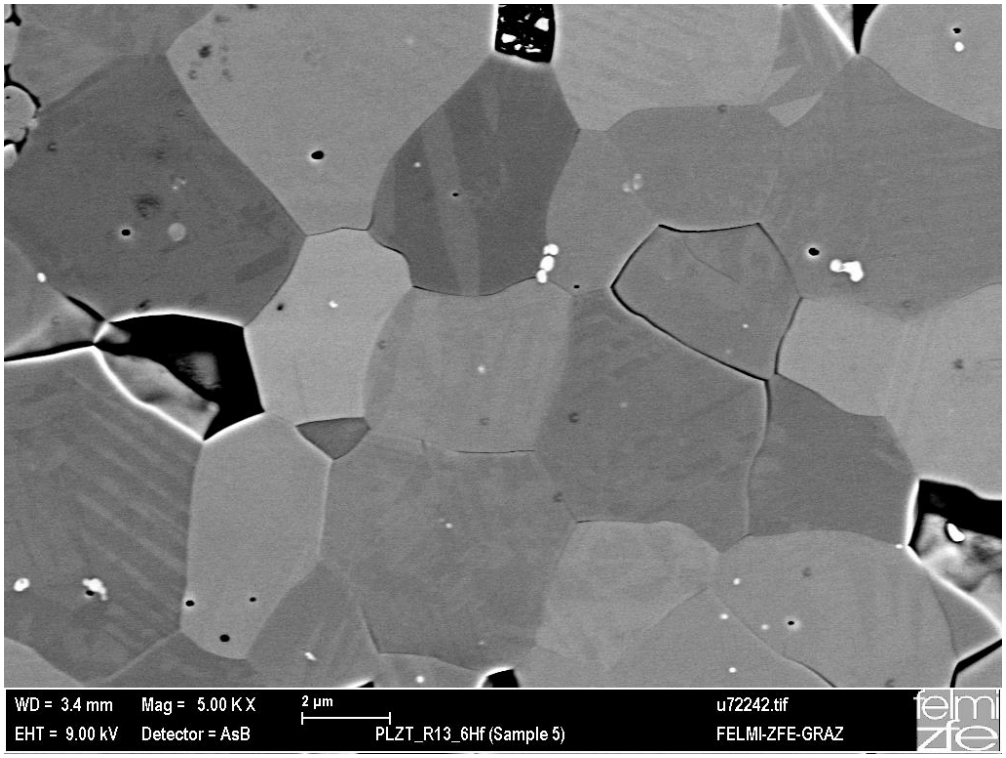

Figure 46 BSE imageof PLZT_90/10_6Hf

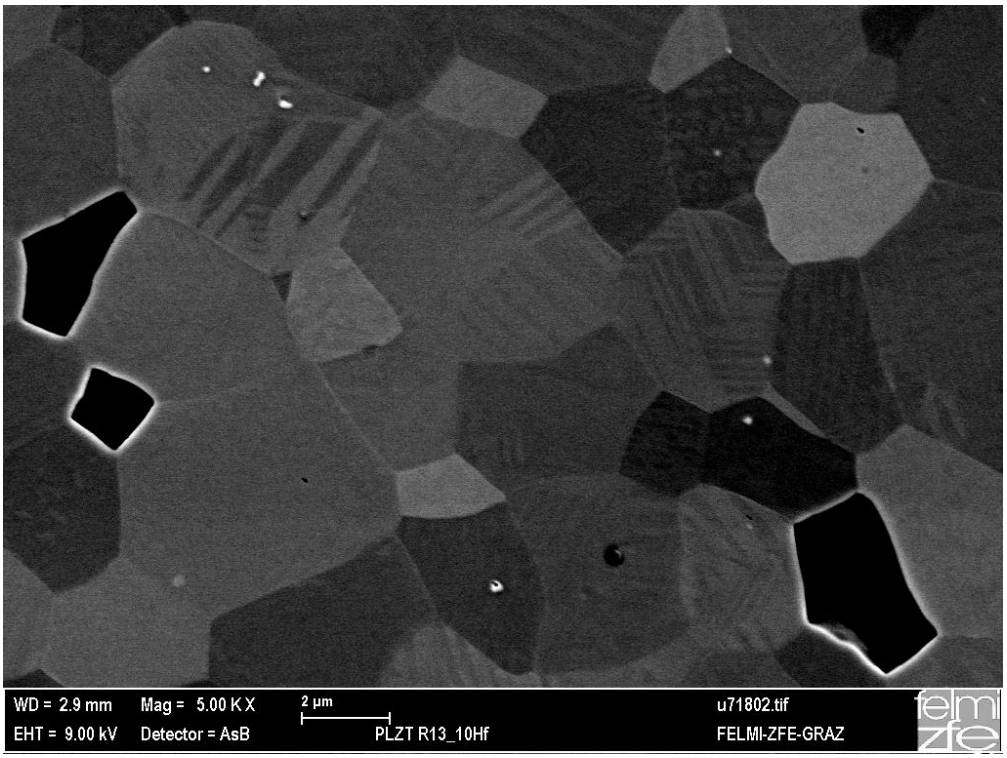

Figure 47 BSE imageof PLZT_90/10_10Hf

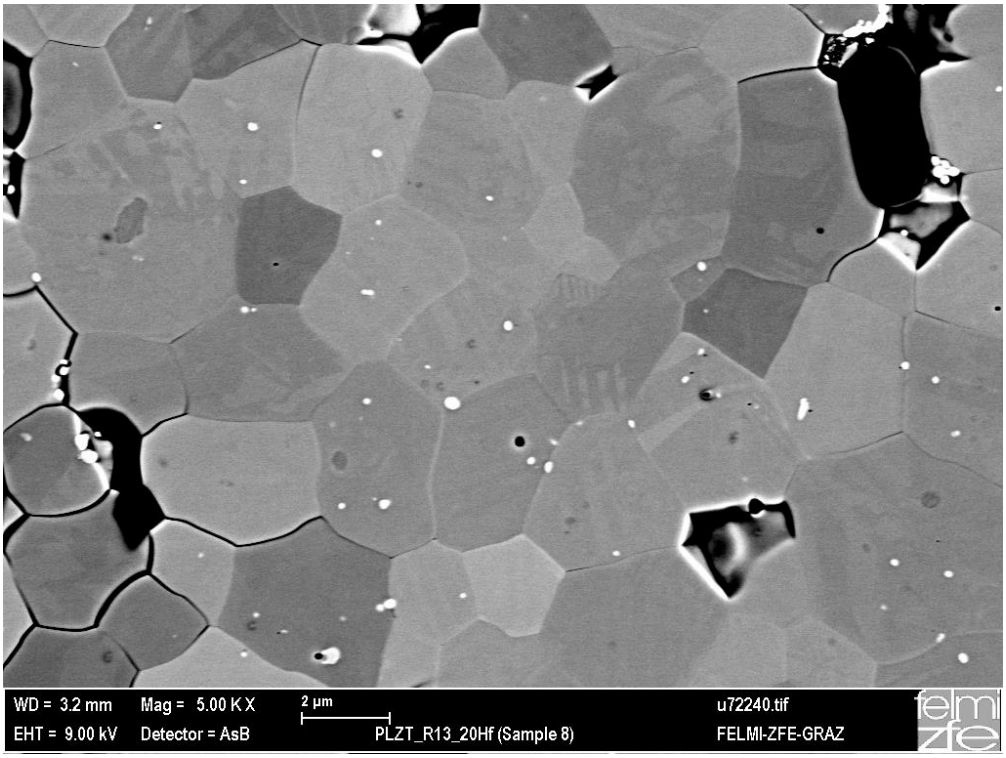

Figure 48 BSE imageof PLZT_90/10_20Hf

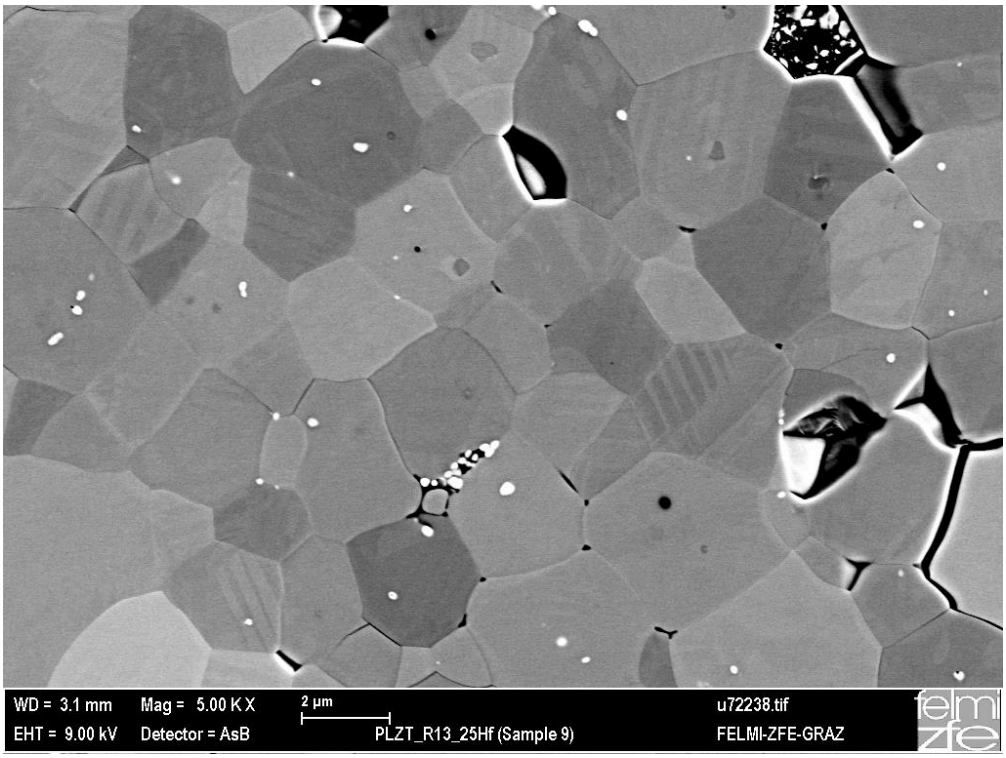

Figure 49 BSE imageof PLZT_90/10_25Hf

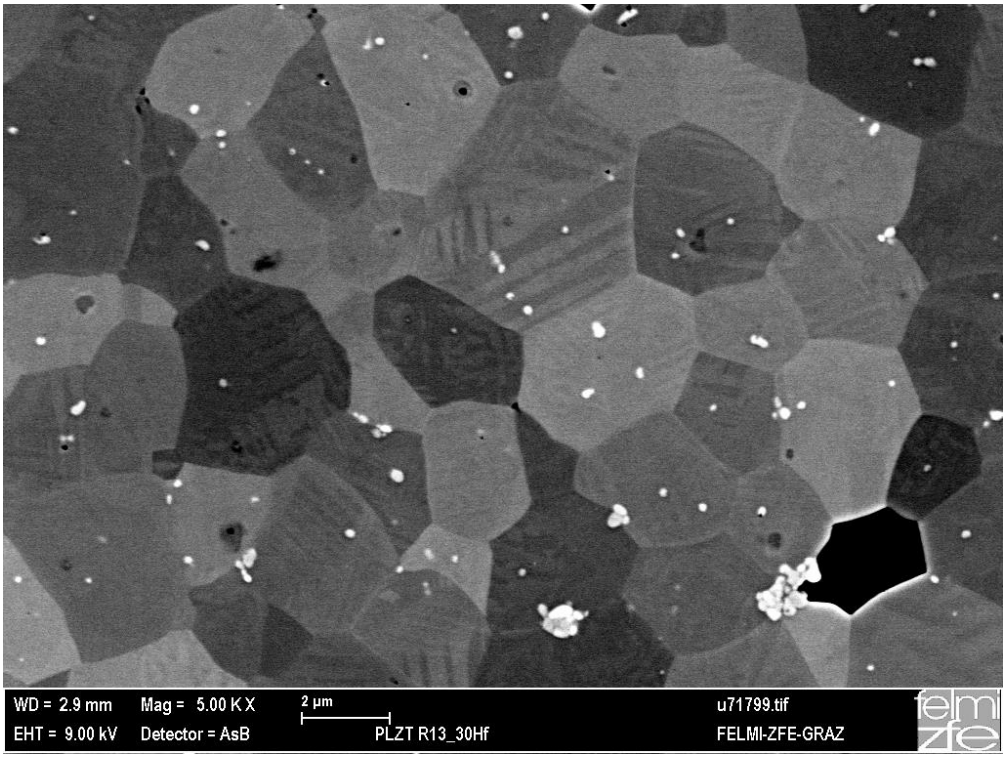

Figure 50 BSE imageof PLZT_90/10_30Hf

9.2.2. PLZT_85/15_xHf:

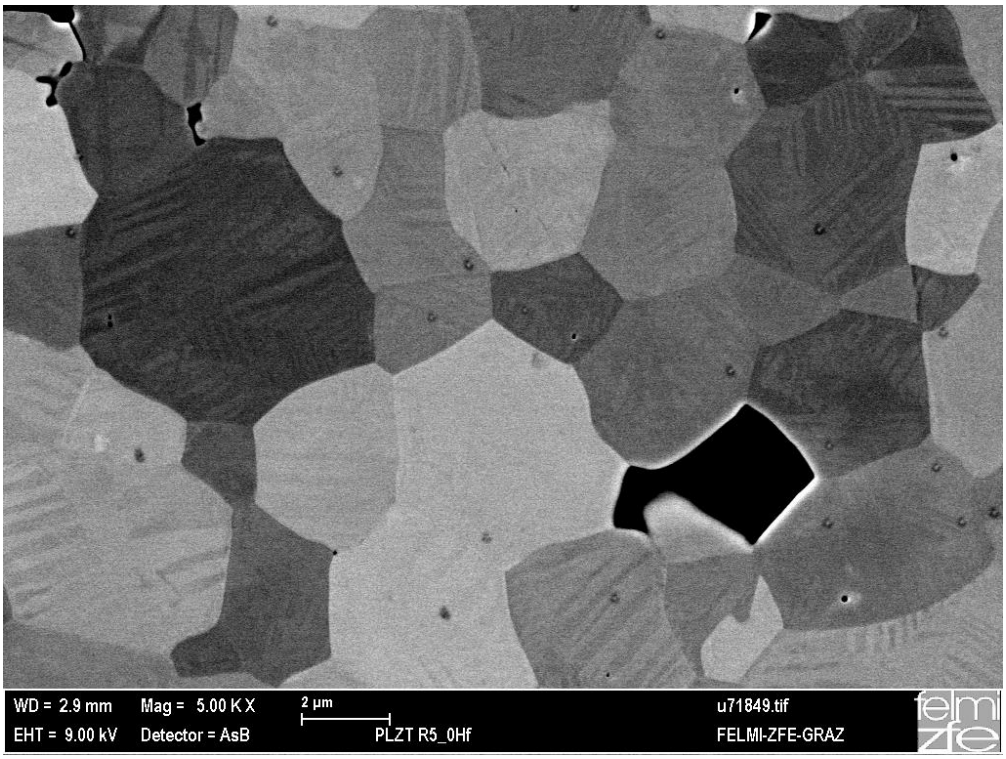

Figure 51 BSE imageof PLZT_85/15_0Hf

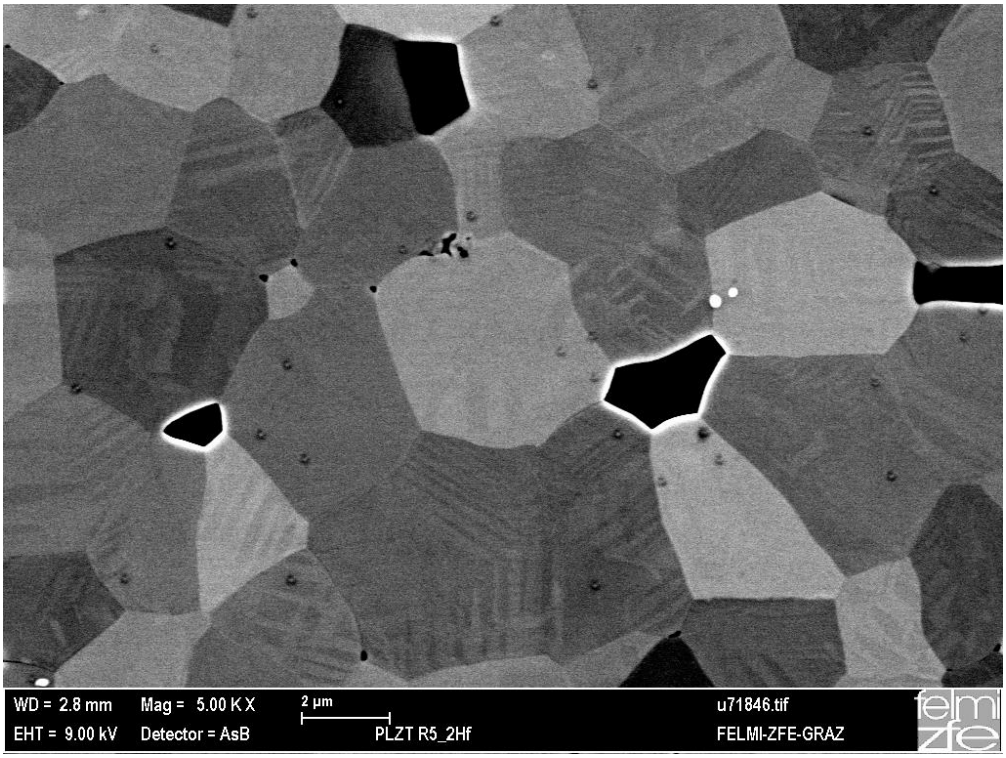

Figure 52BSE imageof PLZT_85/15_2Hf

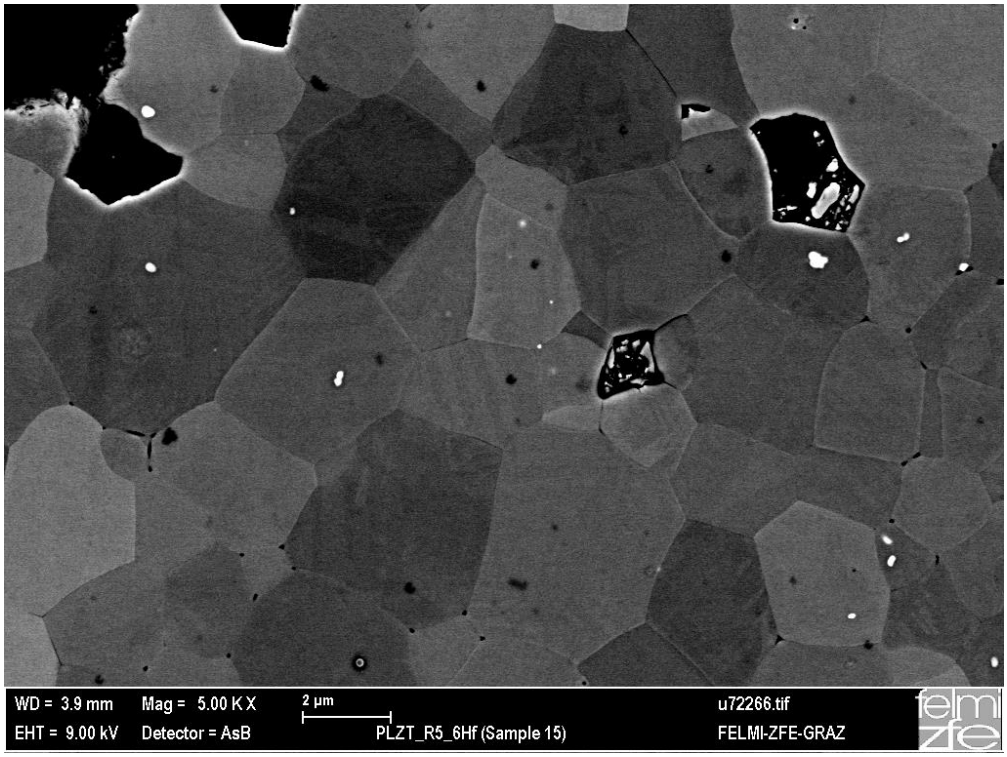

Figure 53 BSE image of PLZT_85/15_6Hf

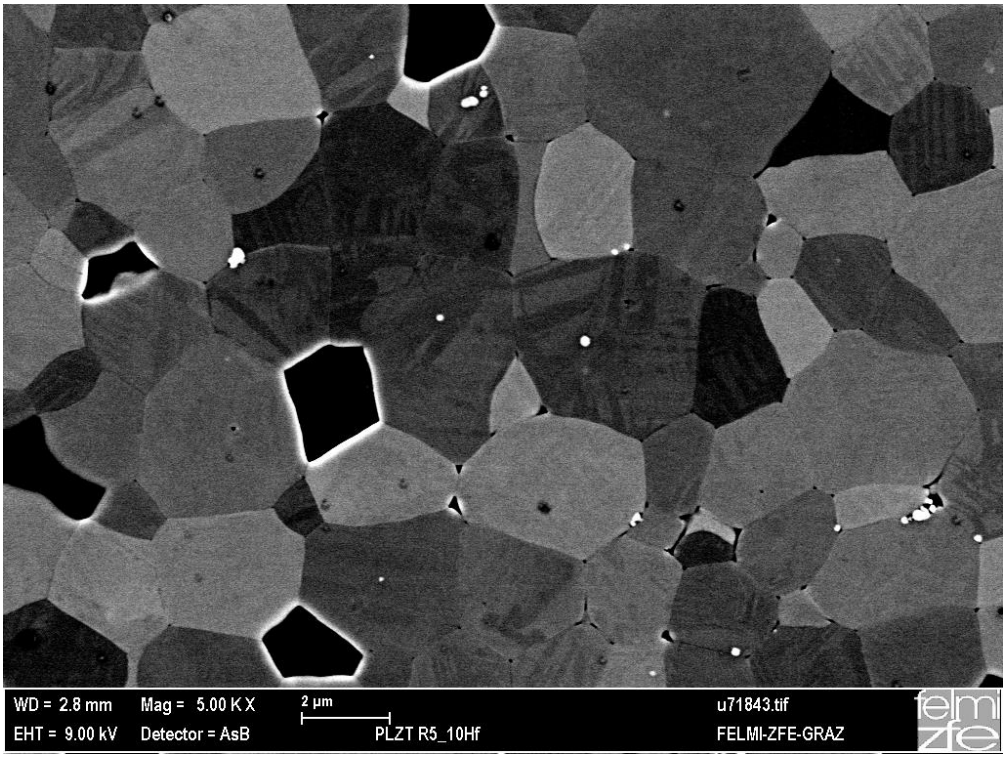

Figure 54 BSE imageof PLZT_85/15_10Hf

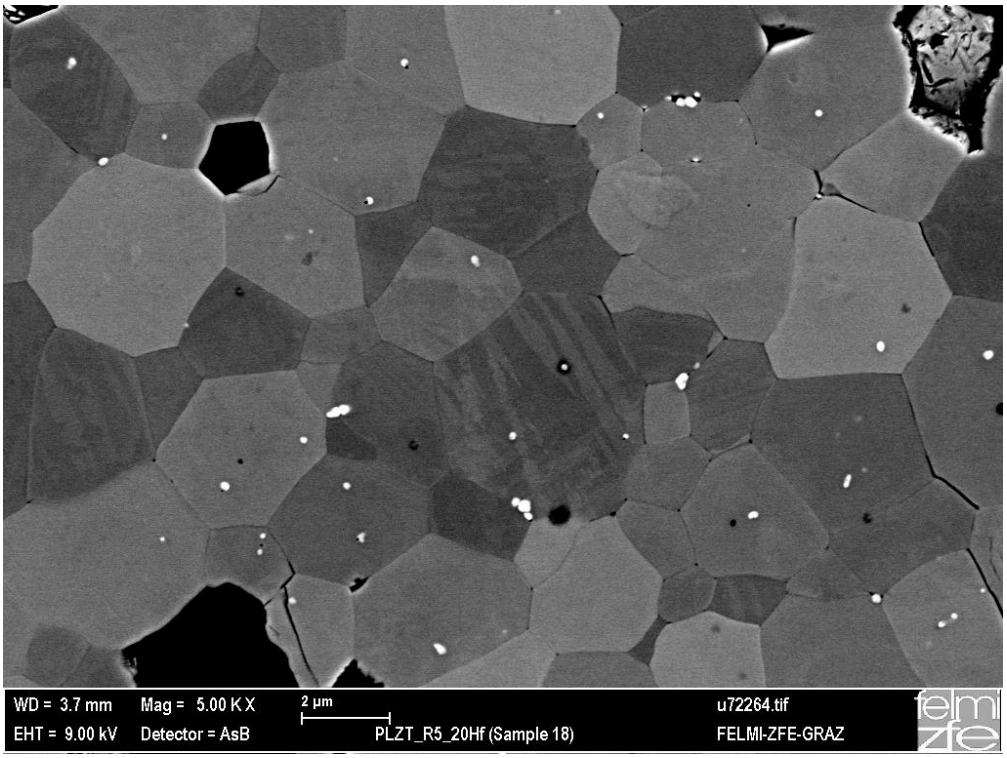

Figure 55 BSE imageof PLZT_85/15_20Hf

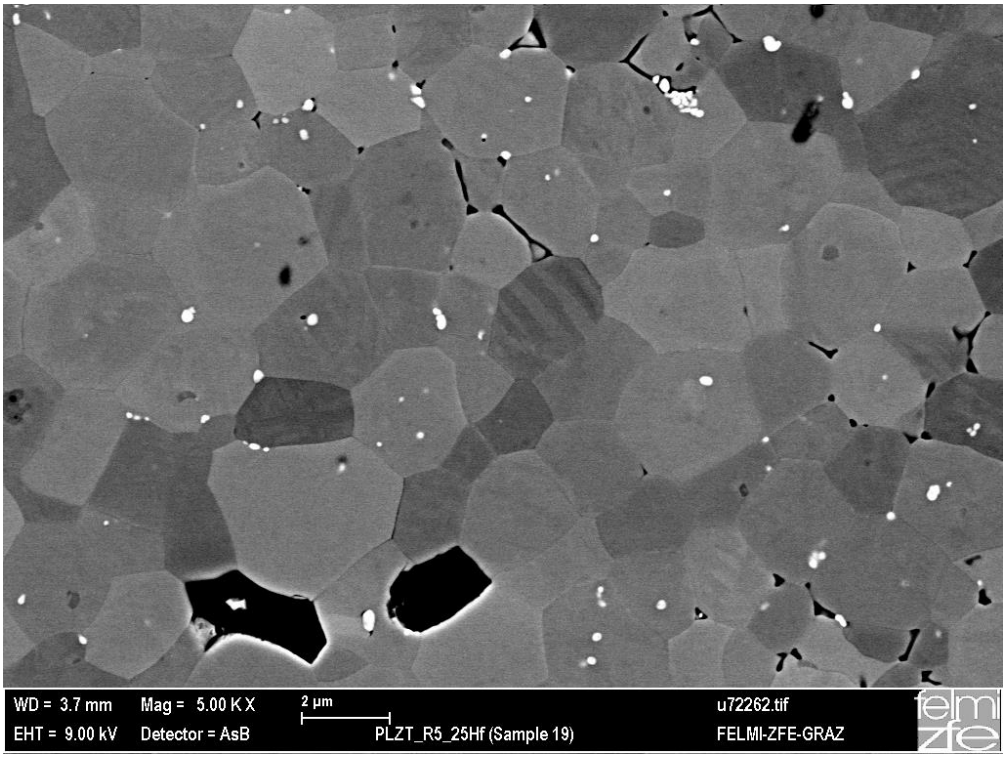

Figure 56 BSE imageof PLZT_85/15_25Hf

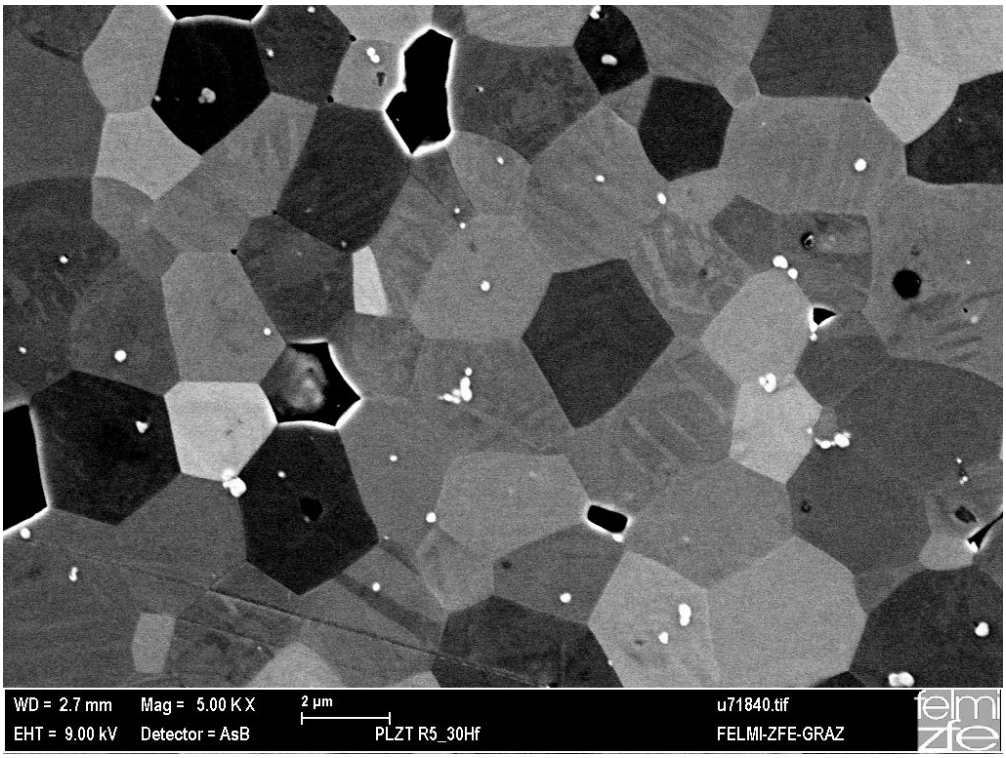

Figure 57 BSE imageof PLZT_85/15_30Hf